

**Investigations on the
Multiferroic and Thermoelectric properties of
Low and Intermediate band width Manganites**

*Thesis submitted to
Cochin University of Science and Technology
in partial fulfillment of the requirements
for the award of the degree of
Doctor of Philosophy*

by

SAGARS



*Department of Physics
Cochin University of Science & Technology
Cochin- 682 022, India.*

August 2010





Investigations on the Multiferroic and Thermoelectric properties of Low and Intermediate band width Manganites

Ph. D Thesis

Author

Sagar S
Kannamkarayil
Thodiyoor North P. O
Karunagappally
Kollam, Kerala, India
Pin: 690523
e-mail: srisagarsankar@yahoo.com

T112

Supervising Guide

Prof. M. R. Anantharaman
Head of the Department
Department of Physics
Cochin University of Science & Technology
Cochin- 682 022,
India.

August 2010

Cover Page Illustration

Back cover: Selected Area Electron Diffraction pattern of LNMO sample



Prof. M. R. Anantharaman

Professor & Head

Department of Physics

Cochin University of Science and Technology

Cochin – 682 022 India.

Certificate

Certified that the present work in this thesis entitled “**Investigations on the Multiferroic and Thermoelectric properties of Low and Intermediate band width Manganites**” is based on the bonafide research work carried out by **Mr. Sagar S** under my guidance at the Department of Physics, Cochin University of Science and Technology, Cochin – 22, Kerala, India and has not been included in any other thesis submitted previously for the award of any degree.

Prof. M. R. Anantharaman

(Supervising Guide)

Cochin -22

20-08-2010

Ph.No: +91484-2577404 Extn. 30 (Off)
E mail: mra@cusat.ac.in mraiya@yahoo.com

Declaration

I hereby declare that the work presented in this thesis entitled **“Investigations on the Multiferroic and Thermoelectric properties of Low and Intermediate band width Manganites”** is based on the original research work carried out by me under the guidance and supervision of Dr. M R Anantharaman, Prof. & Head Department of Physics , Cochin University of Science and Technology, Cochin-682 022 and no part of the work reported in this thesis has been presented for the award of any other degree from any other institution.

Cochin-22
20-08-2009



Sagar S

Acknowledgements

It is a matter of joy for me to present this thesis and I wish to express my grateful appreciation to all who have enabled me to accomplish this piece of work.

With immense pleasure and profound thankfulness, I express my gratitude towards my supervising guide and Head, Department of Physics, Prof. M. R. Anantharaman for all the support and persistent encouragement and personal attention extended to me through out my research period. I am always grateful to him for his competent advice and sustained guidance without which the successful completion of this work would not have been possible.

I wish to acknowledge all former Heads of the Department, Dr. M. Sabir, Dr. K.P. Vijayakumar, Dr. V. C. Kuriakose, Dr. Ramesh Babu. T and Dr. Godfrey Louis for providing the laboratory and library facilities during my research program.

My sincere thanks to all the faculty members of the Department of Physics, Cochin University of Science and Technology for the help and support they have provided for the completion of this research work.

I thank, Council of Scientific and Industrial Research (CSIR), India for providing financial assistance in the form of junior and senior research fellowships.

I am grateful to the faculty and scientists in various institutions around the world, particularly, Dr. V. Ganesan and Dr. R. Rawat of UGC-DAE CSR, Indore, Dr. P.A. Joy of National Chemical Laboratory Pune, Dr. Imad A -al- Omari of Sultan Qaboos University Muscat, Prof. Manfred Albrecht of Chemnitz University of Technology, Germany, Prof. Pulikkal M. Ajayan, Rice University, USA, Dr. Suresh Kumar of Binani Zinc (R&D), Cochin, Dr. V. R. Nair and Dr. P. Narayanan of IREL, Udyogamandal, Dr. Shibu Eapen of STIC, Cochin.

I thank all the teaching and non-teaching staff of the Department of Physics who helped me in various ways.

Magnetics Laboratory was a great place where I always feel as at my home. I am deeply thankful to its past and present members for creating the cordial atmosphere and for their support and help, without which it would have been difficult for me to complete my project. I remember with gratitude the names of Dr. K. A. Malini, Dr. Asha Mary John and Dr. Smitha Sasidharan for their expertise advice and affection. I remember Dr. S. Saravanan, Mr. Sanoj M. A, Mr. Hysen Thomas, Dr. Senoy Thomas and Mr. Narayanan T. N with deep gratitude and affection. I would always cherish the memories with Dr. Sajeev U S , Dr. Swapna S Nair , Dr. Mathew George, Dr. E. M. A. Jamal, Mr.

Vasudevan Nampoothiri, Mr. V Vijayachandran Nair, Mr. Rajeev R Asokan, Mr. Shyam Kishore, Dr. Prema K, H, Dr. Santhosh D. Shenoy, Mr. Tom Thomas, Ms. Leena, Ms. Remya, Mr. Ram Kumar, Mr. Balasubrahmaniam, Mr. Neeraj K, Mr. Anand P. B and Mr. Navaneeth P. I remember Dr. E. M. Mohammed, Dr. C. Joseph Mathai, Dr. S. Sindhu, Dr. Solomon, and Dr. S. Jagatheesan who really worked hard in establishing Magnetics Laboratory.

Special love and thanks to Mr. Sudeep P.M, Dr. Veena Gopalan, Dr. Vijutha Sunny, Ms. Reena Mary A. P, Ms. Geetha P, Ms. Vinayasree S, Ms. Sethulakshmi N and Mr. Abhilash A for their valuable help during the final stage of my thesis work.

I extend my sincere thanks to Dr. Ajimsha R. S, Dr. Anoop Menon and Dr. Jayakrishnan for the nice moments at CUSAT. I thank with love and gratitude all my fellow research scholars of Department of Physics for the affection and support

I am thankful to all the support received from the faculties of N. S. S Hindu College, Changanacherry, Govt. College, Kodenchery and Govt. Polytechnic College, Adoor during my research period. I also extend my heartfelt thanks to my friends at State Forensic Science Laboratory, Thiruvananthapuram for their love and affection.

At this moment I remember Dr. B. Premlet and Late. Prof. M. R. T Nair for their contribution in building up my confidence. I thank all my students for their support. I am grateful to my friend Mr. Venugopal B for his constant encouragement in completing my thesis work.

Words are insufficient to express my acknowledgements for my ever loving parents, for they have been the inspiring force behind me. Due to circumstances they could not complete their school education. But they knew the value of education and provided all the possible facilities for my studies. I am thankful to my brother, sister and in-laws who provided me with all the support for such a long time.

I am deeply indebted to my wife Sruthy and my son Vasudev for the completion of my thesis work and to them I dedicate this Ph. D thesis.

Above all, I thank God Almighty for all blessings showered upon me.

Sagar S

Dedicated to my wife and vasuvava

List of publications

Journal papers

1. Multiferroic properties of Gd based manganites; **S Sagar**, P. A Joy and M. R Anantharaman, ***Ferroelectrics*** 392 (2009) 13-19.
2. Evidence for the existence of multiple equilibrium states in cobalt phthalocyanine tetramer: a study by dielectric spectroscopy, **S Sagar**, S Saravanan, S Suresh Kumar, S Venkatachalam and M. R Anantharaman, ***J. Phys. D: Appl. Phys.***39 (2006) 1678-1683.
3. Colossal thermoelectric power in Gd- Sr manganites, **S. Sagar**, V. Ganesan, P. A. Joy, Senoy Thomas, A. Liebig, M. Albrecht and M. R. Anantharaman, ***EPL*** 91 (2010) 17008.
4. Mechanism of ac conduction in nano structured manganese zinc mixed ferrites, E Veena Gopalan, K. A. Malini, **S. Sagar**, D Sakthi Kumar, Yasuhiko Yoshida, I. A Al-Omari and M. R Anantharaman, ***J. Phys. D: Appl. Phys.*** 42 (2009) 165005.
5. Dielectric studies of nano crystalline nickel – cobalt oxide, Nisha J. Tharayil, **S. Sagar**, R. Raveendran and A. V Vaidyan, ***Physica B: Condensed Matter*** 399 (2007) 1-8.
6. On the paramagnetic conduction mechanism of Gd based manganites, **S. Sagar** and M. R Anantharaman, ***Bulletin of Materials Science*** (Under review).

7. Colossal negative Seebeck coefficient in charge ordered Na doped La manganite, **S. Sagar**, V. Ganesan, P. A. Joy and M. R. Anantharaman (Ready for communication).

Conference papers

1. “The paramagnetic conduction mechanism of Gd manganites: SPH followed by VRH”, **S Sagar** and M. R Anantharaman, National Conference on ‘Current Trends in Materials Science (CTMS-07)’ March 25th-27th 2007, Chengannur, Kerala, India.

2. “Magnetoresistance studies in Na doped manganites” **S Sagar** and M. R Anantharaman, National Seminar on ‘Recent Trends in Material Science Research’, February 14th and 15th, 2008, Govt. College, Kodenchery, Calicut, Kerala, India.

Preface

Development of new materials for making life more humane has been the hall mark of human civilization. From time immemorial, materials in some form or other have played an important role in the day to day life of human beings. Very often, after the discovery of a particular material, its impact lasts longer than anticipated and this leads to economic growth. In the post world war scenario, if the progress and prosperity of a nation was gauged by the consumption of steel, in the new millennium, the emphasis is on finding new substitutes for steel and hence the hunt for new materials to remove obsolescence is ever increasing. Fortunately for the mankind, the dawn of the new millennium witnessed the birth of a new branch of science called nano science. With the advent of nano science, scientists and engineers are toying with the idea of tailoring the properties of materials using size and shape rather than with composition. This has already paved the way for new generation materials like carbon fibers, carbon nano tubes, graphenes and nano ceramics. It is in this context that the world renowned material scientist Eiji Kobayashi remarked “Those who control materials control technology”. This adage speaks volumes on the importance of materials and material science and its relevance in the contemporary world. Miniaturization and submicron technology are the new buzz words of engineers and to be in tune with the Moore’s law, devices and systems are shrinking day by day and this is where size is going to play a lead role. In the understanding of the underlying physics which governs the properties, whether at the micro level or nano level solid state physics has a lead role in establishing the various phenomena exhibited by new and novel materials. Thus the study of materials is always synonymous with solid state physics.

In the realm of solid state physics crystal structure plays a dominant role in determining the properties of materials. It is well known that ceramics are crystalline materials and structure plays its part in deciding most of the useful

properties for applications. Materials with both symmetric and asymmetric crystal structures are found to be useful materials for various applications. However materials with cubic symmetry like spinels and perovskites have been playing a major role with respect to structures. Perovskite materials are fascinating because they display ferroelectricity. A classical example of a ferroelectric material is barium titanate (BaTiO_3) and is a known perovskite. Manganites are materials possessing perovskite structure and are widely studied the world over during the past century. Lanthanum manganites, lanthanum cobaltites and lanthanum nickelates are perovskite materials. It was believed in the eighties that they would replace all the existing auto catalysts. In the late eighties, with the advent of high T_c superconductivity, materials with perovskite structure were considered to be a prerequisite for superconductivity. Enormous research input has gone into this particular field and hence the scientific world is benefited by the possession of a huge and rich literature on these materials. Most of the underlying Physics have been explained satisfactorily. This was a time when people were looking for exotic materials for employment in storage devices and for other sensing applications. The discovery of Giant Magneto-Resistance (GMR) in multilayer films and later the revelation of Colossal Magneto-Resistance (CMR) in perovskites opened the flood gates for renewed research activities in these class of materials. Among the various materials having potential for CMR, Lanthanum manganite occupied an important position because of a variety of reasons. For example, it is possible to have Jahn Teller distortion, charge ordering and double exchange which were thought to be contributing to the CMR exhibited by these materials. If colossal magneto resistance in manganites is to be employed in devices either as sensors or memory devices, then the field at which material exhibit CMR must be reasonably low and must be able to produce in the laboratory cost effectively. So attempts were made by scientists and engineers to vary the composition and investigate its magneto transport properties. Such a study is an on going activity.

Multiferroic materials are fascinating and have potential applications as memory devices, spintronic devices, sensors and actuators. Multiferroicity is the simultaneous occurrence of ferroelectricity, ferromagnetism and or ferroelasticity. In the early 2000, manganites were considered as potential material for multiferroic applications because of the leverage with which one can control various properties by compositional changes. Manganites exhibit peculiar electric and structural properties including orbital and charge ordering, formation of local moments, Jahn teller distortions, double exchange and super exchange. It was thought that a proper understanding of these parameters will lead not only to the understanding of mechanism of multiferroicity but also enable to fabricate devices based on multiferroics. The ease with which these compounds can be synthesized made them very attractive for research in material science.

The CMR property exhibited by manganites and other compounds can be explained by double exchange interaction and Jahn Teller distortion. The hopping of electrons mediated by double exchange interaction depends on the extent of orbital overlapping and spin alignment between neighboring sites. Hence the amount of distortion in the structure and consequently cation radii determine the hopping rate of electrons and in turn the magneto resistance of manganites. In the case of manganites, the width of conduction band formed by the hybridization of manganese e_g level and oxygen p level is termed as band width. Based on that electron bandwidth, manganites can be divided into three. They are high, intermediate and low bandwidth manganites. In a series resembling $La_{1-x}A_xMnO_3$, if A cation is chosen judiciously it can give rise to different compositions. If A cation is an alkali metal and if it is Na which has the right ionic radii and does not produce distortion, the compound with varying x can be interesting from a fundamental point of view. Moreover if for a particular x produces the right Mn^{4+}/Mn^{3+} ratio conducive for double exchange then this compound is all the more attractive for investigation from a transport property study angle. The above is true for low concentration of x.

However for intermediate bandwidth manganites with $x=0.5$ can lead to charge ordering. A very simple calculation establishes the fact that for the composition corresponding to $x=0.25$, the ratio of Mn^{4+}/Mn^{3+} will be 1. It is presumed that at $x=0.25$ it can give rise to multiferroicity and then these compositions are of interest from a fundamental perspective. More over it has been reported that size alters many of the useful properties exhibited by these class of materials and if $La_{1-x}Na_xMnO_3$ can be prepared in the nano regime the effect of size can also be studied. This is especially true since charge ordering can be influenced by particle size distribution. This is another motivation of the present study. Similarly for the low band width manganites charge ordering is exhibited by composition $0.3 \leq x \leq 0.5$. From literature one can notice that studies on the charge ordering properties of Pr and Nd based manganites are in plenty. However studies on Gd based manganites are not very common in literature. Compounds having the formula $Gd_{1-x}Sr_x MnO_3$ are also interesting since they also belong to the class of low bandwidth manganites. Such a study also provide an opportunity for a comparative study vis a vis low band width versus intermediate bandwidth.

The thermoelectric effect is the generation of an electric field due to a thermal gradient, and the rate of change of thermoelectric voltage with temperature is called the thermoelectric power or Seebeck coefficient. Possible applications of thermoelectric materials are in eco-friendly refrigeration and in electrical power generation. The efficiency of a thermoelectric conversion is determined by the figure of merit Z which can be written in the form $Z = Q^2 \sigma / K$. Here, Q is the Seebeck coefficient, σ is the electrical conductivity and K is the thermal conductivity. Accordingly, high Seebeck coefficient and electrical conductivity and low thermal conductivity are necessitated for potential applications. Metals are poor thermoelectric materials because they possess small values of Seebeck coefficient. Insulators display large values of Seebeck coefficient, but the poor electrical conductivity sets limitations to their applications. The best thermoelectric materials are semiconductors with an

electronic density of $10^{19}/\text{cm}^3$. A survey of literature reveals that normal broad band semiconductors, rattling semiconductors with skutterudite crystal structure, correlated metals and semiconductors, Kondo insulators and semiconductor quantum wells were also found to be promising thermoelectric materials. Rare earth inter-metallic compounds where 4f levels are close to the Fermi energy and having a high density of states near the Fermi energy scatter most of the conduction electrons. Moreover the thermoelectric effect is inversely proportional to thermal conductivity. Therefore, materials with large number of atoms per unit cell, large average atomic mass and large coordination number per unit atom are likely to display large thermoelectric effect. It is seen from literature that the Seebeck coefficient of manganites is routinely investigated to explain the transport properties of manganites and not much attention is paid to the fact that such materials can be a potential thermoelectric material with colossal Seebeck coefficient. Large bandwidth manganites like $\text{La}_{1-x}\text{Sr}_x\text{MnO}_3$, though they possess large value of electrical conductivity, possess only small value of Seebeck coefficient. However, low band width manganites like $\text{Gd}_{1-x}\text{Sr}_x\text{MnO}_3$ compounds can be a potential material for large Seebeck coefficient.

Even though the multiferroism is discovered in some manganites, a detailed analysis on dielectric property of manganites was not forthcoming. Moreover the low temperature dielectric studies also can throw light on the different relaxation mechanisms that exist in these compounds. When materials are prepared in the nano regime the role of grains and grain boundaries decide the vital performance of these materials. Hence impedance spectroscopic studies are relevant here. Thus both dielectric spectroscopy and impedance spectroscopy are considered vital tools in understanding the transport properties of these class of manganites. This is yet another motivation of the present investigation.

This thesis lays importance in the investigation on the multiferroic and thermoelectric properties of selected representatives of low bandwidth and intermediate band width manganites. The first candidate, Strontium doped Gd

manganite, is prepared by wet solid state reaction method and the second candidate, Na doped La manganite, by citrate gel method. In addition to the above mentioned properties, magneto resistance and dielectric properties are investigated. Using dielectric spectroscopic the dispersion parameters are correlated to the relaxation mechanisms and an attempt is made to obtain the grain and grain boundary contribution to the impedance of the sample through impedance spectroscopy studies. Thus the objectives of the present work can be summarized and are listed as follows

- Synthesis of low bandwidth manganites belonging to the series of $Gd_{1-x}Sr_x MnO_3$ ($x = 0.3, 0.4$ and 0.5) by wet solid state reaction method
 - Synthesis of intermediate manganites belonging to the series of $La_{1-x}Na_xMnO_3$ ($x = 0.05, 0.1, 0.15, 0.2$ and 0.25) by citrate gel method
 - Structural and magneto-resistance studies of $Gd_{1-x}Sr_x MnO_3$ where $x = 0.3, 0.4$ and 0.5 .
 - Structural and magneto-resistance studies of $La_{1-x}Na_xMnO_3$ where $x = 0.05, 0.1, 0.15, 0.2$ and 0.25 .
 - Study the electrical properties of samples $Gd_{1-x}Sr_x MnO_3$ and $La_{1-x}Na_xMnO_3$
 - Evaluation of dielectric parameters using dielectric spectroscopic studies of the manganite samples
 - Study the grain and grain boundary contribution of impedance using impedance spectroscopic studies of the manganite samples
 - Evaluate the thermoelectric power of the samples $Gd_{1-x}Sr_x MnO_3$ and $La_{1-x}Na_xMnO_3$
- and
- Correlation of results

Thus the proposed thesis is entitled “**Investigations on the Multiferroic and Thermoelectric properties of Low and Intermediate band width Manganites**” and consists of eight chapters.

Chapter 1 gives an introduction and basic principles about perovskite structure, conduction mechanisms in manganites. Ferromagnetism and ferroelectricity, multiferroism and thermoelectric power are also discussed in brief.

Chapter 2 deals with the analytical techniques like X-ray diffraction, Scanning electron microscopy (SEM) and Transmission electron microscopy (TEM) used for the structural characterization of the manganite samples. The theoretical and experimental aspects of magnetic, magnetoresistance and thermoelectric power measurements are also explained in this chapter.

Chapter 3 essentially discusses the synthesis, structural, dc conductivity, magnetic and magnetoresistance of the low band width manganite series $Gd_{1-x}Sr_xMnO_3$ ($x = 0.3, 0.4$ and 0.5).

Chapter 4 deals with the synthesis, structural, dc conductivity, magnetic and magnetoresistance of the intermediate band width manganite series $La_{1-x}Na_xMnO_3$ ($x = 0.05, 0.1, 0.15, 0.2$ and 0.25).

Chapter 5 deals with the dielectric, impedance and ac conductivity studies of Gd based manganites with special emphasis to their relaxor multiferroic property. The ferroelectric behavior is verified using capacitance – voltage (CV) studies.

Chapter 6 discusses the results obtained from dielectric spectroscopic and impedance spectroscopic studies of nano sized Na doped La manganite. The dispersion parameters obtained are correlated to the conduction mechanism and nano size of the manganite sample.

Chapter 7 reports the colossal thermoelectric power shown by charge ordered manganites. The thermoelectric properties of non charge ordered manganites are also discussed.

Chapter 8 is the concluding chapter of the thesis and in this chapter the salient observations and the inferences drawn out of these investigations are presented in a nutshell. The scope for future work is also proposed here.

Contents

Chapter 1

<i>Introduction</i>	<i>1</i>
1.1 Magneto-Resistance (MR)	2
1.1.1 Giant Magneto-Resistance (GMR)	3
1.1.2 Colossal Magneto-Resistance (CMR)	4
1.1.3 Applications and Limitations	5
1.2 Manganites	7
1.2.1 Structure of manganites	8
1.2.2 Electronic structure and Crystal field splitting	11
1.2.3 Orbital degeneracy and Jahn Teller effect	14
1.2.4 Tolerance Factor	15
1.2.5 Double Exchange Mechanism	16
1.2.6 Low, Intermediate and High Bandwidth Manganites	18
1.2.7 Charge Ordering in Manganites	19
1.2.8 Conduction mechanisms in the insulating phase of manganites	20
1.3 Multiferroics	24
1.3.1 Ferroelectricity	24
1.3.2 Ferromagnetism	28
1.3.3 Multiferroism	31
1.3.4 Requirements of multiferroicity	33

1.3.5	Applications of multiferroics	34
1.4	Thermoelectric Power	35
1.4.1	Seebeck effect and other thermoelectric effects	35
1.4.2	Applications of Thermoelectric Power	36
1.5	Motivation of the Thesis	39
1.6	Objectives of the work	42
	References	43

Chapter 2

Experimental Techniques

2.1	Synthesis Techniques	49
2.1.1	Wet solid state reaction method	49
2.1.2	Citrate gel method	49
2.2	Structural Characterisation	50
2.2.1	X-Ray Diffraction Analysis	51
2.2.2	Transmission Electron Microscopy (TEM)	52
2.2.3	Selected Area Electron Diffraction Pattern (SAED)	53
2.2.4	Scanning Electron Microscopy (SEM)	54
2.2.5	Atomic Absorption Spectroscopy (AAS)	55
2.3	D. C conductivity and Magneto-Resistance Measurements	55
2.3.1	D. C conductivity measurements	55
2.3.2	Magneto Resistance measurement	57

2.4	Dielectric and Impedance Measurements	60
2.4.1	Dielectric measurements	60
2.4.2	Dielectric Spectroscopy (Cole-Cole Plot)	64
2.4.3	Impedance Spectroscopic studies	66
2.5	Magnetic Characterisation	68
2.5.1	Vibrating Sample Magnetometer (VSM)	68
2.5.2	Field Cooled and Zero Field Cooled Measurements	71
2.6	Thermo Electric Power Measurements	72
	References	73

Chapter 3

Investigation on the Magnetoelectric Transport Properties of Gadolinium Based Manganites

3.1	Introduction	77
3.2	Sample preparation and structural characterization	78
3.3	D. C Conductivity and Magnetization Studies of GSMO samples	80
3.3.1	D. C Conductivity studies	80
3.3.2	Magnetisation studies	86
3.4	Magneto-Resistance (MR) studies of GSMO	88
3.5	Conclusion	91
	References	92

Chapter 4

Studies on the Magnetoelectric Transport Properties of Sodium Doped Lanthanum Manganites

4.1	Introduction	95
4.2	Sample preparation and structural characterisation of LNMO samples	96
4.3	D. C Conductivity and Magnetisation Studies of LNMO samples	
4.3.1	D. C Conductivity studies	101
4.3.2	Magnetisation studies	104
4.3.3	Conduction mechanism in paramagnetic region	105
4.3.4	Conduction mechanism in ferromagnetic region	109
4.4	MR studies of LNMO	112
4.5	Conclusion	116
	References	116

Chapter 5

On the Multiferroic Behaviour of Gadolinium Based Manganites

5.1	Introduction	121
5.2	Dielectric permittivity studies of GSMO	122
5.3	Capacitance Voltage (CV) measurements in GSMO	129
5.4	A. C conductivity studies in GSMO	130
5.5	Conclusion	134
	References	135

Chapter 6

Dielectric and Impedance Spectroscopic Studies of Sodium Doped Lanthanum Manganites

6.1	Introduction	137
6.2	Dielectric studies of LNMO	138
6.3	Cole-Cole plot studies of LNMO	143
6.4	Impedance spectroscopic studies of LNMO	155
6.5	Dielectric and impedance studies of charge ordered LNMO	158
6.6	Conclusion	159
	References	161

Chapter 7

On the Colossal Thermoelectric power of Charge ordered Manganites

7.1	Introduction	163
7.2	Thermoelectric power studies of GSMO and LNMO samples	164
	7.2.1 Colossal thermoelectric power exhibited by charge ordered GSMO and LNMO manganites	165
	7.2.2 Thermoelectric power in non charge ordered LNMO	170
7.3	Conclusion	177
	References	177

Chapter 8

	<i>Conclusion</i>	180
--	--------------------------	-----

Chapter 1

Introduction

Material science and engineering have been at the frontier of technological development since the bronze and iron ages. The evolution of material science is always an indicator to man's progress and his urge to improve upon the existing and replace the obsolete with novel materials often results in newer materials and innovations. One prime example of a small but diverse group of materials is the perovskite family. Physicists, chemists and material scientists have shown great interest in these materials, because of properties such as high temperature superconductivity, colossal magneto-resistance and ferroelectricity. A wide variety of fundamental properties like magnetism, ferroelectricity, colossal magneto-resistance and half-metallicity exhibited by perovskite materials make them fascinating from a fundamental perspective as well as an application point of view. They are used in a number of important technological applications such as transducers and memories. A classic example of perovskite structured material is BaTiO_3 which is a well known ferroelectric material.

Manganites are mixed valent manganese oxide material with perovskite structure. They are good candidates for research because of their rich phase diagram and colossal magnetoresistance property. They attracted lot of attention due to their properties like charge ordering, orbital ordering, Jahn Teller distortion etc. [1 - 4]. They find numerous applications in the field of technology as magnetic read heads, sensors and switches. The discovery of Giant Magneto-Resistance (GMR) in multilayer films and later the revelation of Colossal Magneto-Resistance (CMR) in perovskites opened the flood gates for renewed research activities in these class of materials. Multiferroicity is the simultaneous

occurrence of ferroelectricity, ferromagnetism and or ferroelasticity. Multiferroic materials are fascinating and have potential applications as memory devices, spintronic devices, sensors and actuators. Hundreds of perovskite materials are magnetic and hundreds of others are ferroelectric. But these properties very seldom co-exist. Manganites were considered as potential material for multiferroic applications because of the leverage with which one can control various properties by compositional changes. Seebeck coefficient of manganites is routinely investigated to explain the transport properties of manganites and not much attention is paid to the fact that such materials can be a potential thermoelectric material with colossal Seebeck coefficient. The magnetoresistance property and its applications are briefly introduced, in this part of the thesis, along with an overview of manganite structure, crystal field splitting and double exchange mechanism. A comprehensive picture of charge ordering, ferromagnetism, ferroelectricity and multiferroism is also included in this chapter. Thermoelectric effects and their applications are also incorporated.

1.1 Magneto-Resistance (MR)

Usually the resistivity of a material depends on temperature only. But for some materials the electrical resistivity depends on the value of applied magnetic field. This property, by virtue of which certain materials exhibit different values of resistance with and without magnetic field, is called magneto-resistance. The physical quantity magneto-resistance (MR) is defined as the ratio of change in resistance to the zero field resistance.

$$MR = \frac{R(H) - R(0)}{R(0)} \quad (1.1)$$

where $R(H)$ and $R(0)$ designate resistance in the applied field (H) and zero field respectively. It can be broadly classified into two; Giant Magneto-resistance (GMR) and Colossal Magneto-resistance (CMR). GMR was discovered in 1988 by Baibich *et al* in Paris [5]. It is the phenomenon where the resistance of

specially designed magnetic multi-layers drops dramatically when magnetic field is applied. It is described as giant because it has a much larger effect than that had been previously seen in metals. In 1991 Jin *et al* discovered very large magneto-resistance in certain type of materials, in their bulk form, called manganites [6]. Manganites are mixed valent manganese oxides. This phenomenon is called Colossal Magneto-Resistance. The word colossal is used to distinguish it from GMR.

1.1.1 Giant Magneto-Resistance (GMR)

GMR has been the subject of a huge international research leading to numerous technological applications. It is observed in magnetic multilayered structures, where two magnetic layers are closely separated by a thin nonmagnetic spacer layer. The first magnetic layer allows electrons with only one spin state to pass through easily. If the second magnetic layer is ferro-magnetically aligned, then that electron can easily find its way to the other end and hence the electrical resistance becomes low. But if the second layer is misaligned, then neither electrons (spin up and spin down) can get through the structure easily and the electrical resistance becomes high. This is illustrated in figure 1.1.

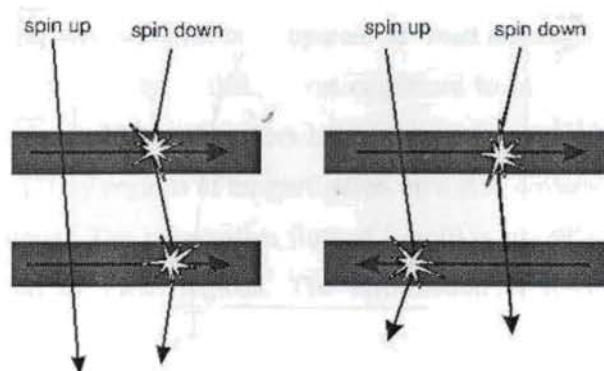


Figure 1.1 Spin alignment effect in GMR

By applying a magnetic field, ferromagnetic alignment can be achieved in the magnetic layers and this diminishes the resistance. The largest application of GMR is in the data storage industry. Other applications are in solid state compasses, automotive sensors, nonvolatile memory and detection of land mines [7].

1.1.2 Colossal Magneto-resistance (CMR)

Colossal magnetoresistance is a bulk property which originates from magnetic ordering and is usually confined to the vicinity of curie temperature (T_c). CMR materials are good candidates for research because of their structural, electronic and magnetic properties, which are interrelated and not very well understood. These materials exhibit a very rich phase diagram, ranging from ferromagnetic metal to antiferromagnetic insulator.

The variation of magnetisation and resistivity in CMR materials with temperature is shown in figure 1.2.

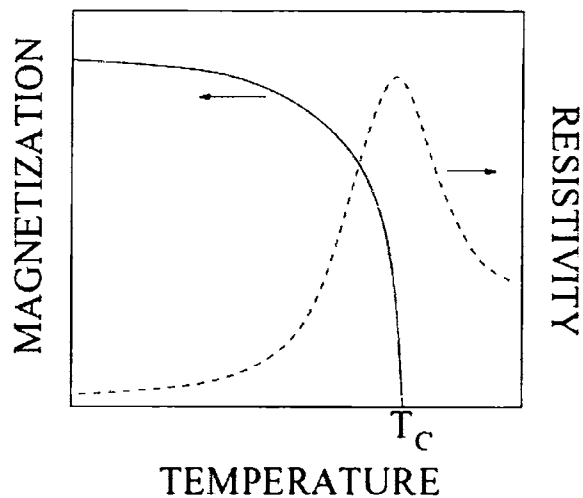


Figure 1.2 Magnetisation and resistivity vs temperature for CMR material

As temperature increases the material undergoes a phase transition from ferromagnetic to paramagnetic (or antiferromagnetic) and a simultaneous metal to insulator transition. These two transitions take place nearly at the same temperature, which is indicative of the existence of a strong relationship between magnetic ordering and transport properties in the case of CMR materials. Manganites, cobaltites and nickelates are examples of materials exhibiting colossal magnetoresistance.

1.1.3 Applications and Limitations of Magnetoresistance

Magneto-resistance already has magnetic appeal. It allows more data to be packed on computer disks. If improvements are made in the interfaces between magnetic layers in thin-film structures, the number of new applications could prove irresistible. For example, it would be possible to make computer operating memories [random access memory (RAM)] that are immune to power disruptions and ionizing radiation. MR motion sensors could be developed to increase the efficiency and safety of home appliances, automobiles, and factories. Magnetoelectronic devices may someday complement or even replace semiconductor electronic devices.

MR recently come out of the laboratory and started finding places in our computers. This is because of the development of “read sensors” for magnetic disk drives [8 , 9]. The capacity of disk drives continues to increase rapidly as they shrink in size and thus MR read sensors have become increasingly important. The data are written as tiny regions of magnetisation on a disk covered with a thin film of magnetic material. The information (bits of 1 or 0) is stored as the direction of the magnetisation of these regions. The information is read by sensing the magnetic fields just above these magnetised regions on the disk. As the density gets higher, these regions get smaller, so the fields that must be sensed to read the data become weaker. Read sensors that employ the MR effect provide the best technology currently available for detecting the fields from these tiny regions of

magnetisation. These tiny sensors can be made in such a way that a very small magnetic field causes a detectable change in their resistivity; such changes in the resistivity produce electrical signals corresponding to the data on the disk, which are sent to the computer. It is expected that the MR effect will allow disk drive manufacturers to increase the density at least until disk capacity reaches 10 gigabits per square inch. At this density, 120 billion bits could be stored on a typical 3.5-inch disk drive, or the equivalent of about a thousand 30-volume encyclopedias.

Today's technology uses semiconductor RAM because it is fast, dense, and relatively inexpensive. In semiconductor RAM, data are stored as small regions that have an excess or deficit of electrons. This use of electrical charges to represent data has two serious drawbacks. First, since these charges leak away, the data must be refreshed several times a second by an electrical circuit. Thus, if the power goes off before the data can be written back to the hard disk for permanent storage, they will be lost. Second, because ionizing radiation temporarily destroys a semiconductor chip's semiconducting properties, it can destroy data. Using GMR, it may be possible to make thin-film of magnetic RAM that would be just as fast, dense, and inexpensive. It would have the additional advantages of being nonvolatile and radiation-resistant. Data would not be lost if the power failed unexpectedly, and the device would continue to function in the presence of ionizing radiation, making it useful for space and defense applications.

The application of GMR in motion sensors is also likely to be important in our homes, automobiles, and factories. It provides a convenient way of sensing the relative motion and position of objects without physical contact. Just attach a magnet to one object and a GMR sensor to another. Alternatively, if one of the objects contains a magnetic material such as iron or steel, the object in motion will alter any magnetic field that is present. A GMR sensor could detect these small changes in the magnetic field.

Applications of this effect could become widespread in the industrial, commercial, and military worlds. Here's a possible list: sensitive detectors for wheel-shaft speed such as those employed in machine-speed controllers, automotive antilock brakes, and auto-traction systems; motion and position sensors for electrical safety devices; current transformers or sensors for measuring direct and alternating current, power, and phase; metal detectors and other security devices; magnetic switches in appliance controls, intrusion alarms, and proximity detectors; motor-flux monitors; level controllers; magnetic-stripe, ink, and tag readers; magnetic accelerometers and vibration probes; automotive engine control systems; highway traffic monitors; industrial counters; equipment interlocks; and dozens of other applications requiring small, low-power, fast sensors of magnetic fields and flux changes [11]. Furthermore, suitable film-deposition processes could also permit fabrication of MR devices on electronic-circuit chips to produce highly integrated MR sensors at low cost and high volumes for mass industrial markets. With its promise for tomorrow's technologies, MR is bound to attract lots of attention.

Manganites are finding some difficulties in their way to technological applications. Single crystalline samples and epitaxial thin films show intensive magneto-resistance only close to T_c . The larger the T_c , smaller the magneto-resistance. Therefore an improvement of magneto-resistance leads to a decrease of T_c below room temperature. Moreover magnetic fields of several Tesla are required to get CMR. Therefore the main challenge in this field is the synthesis of a material which shows very high value of MR near room temperature with the application of a small magnetic field.

1.2 Manganites

Manganese (Mn), with its five 3d and two 4s electrons, is a transition metal. As such it exhibits variable valency and forms stable compounds in several formal oxidation states. Manganese dioxide ($Mn^{4+}O_2^{2-}$) or pyrolusite, for example

has a high natural abundance in earth's crust. It was first recognized as an element by Swedish chemist Karl Wilhelm Scheele in 1774, which was obtained by treating manganese dioxide with hydrochloric acid. Manganese dioxide's next claim to fame occurred in 1938 with the first observation of antiferromagnetism, two years after its production by Louis Neel. In the second half of twentieth century; another class of manganese oxide called manganites attracted attention of material scientists. 1950, C. H Jonker and J. H van Santen crystallized the first mixed-valence manganites [12]. Manganites are usually perovskite structured manganese oxides showing colossal magnetoresistance property. The mixed valency can be usually obtained by doping alkaline earth in the rare earth manganite. Since rare earth atom is trivalent, manganese has valency 3+ in rare earth manganites. In the case of alkaline earth manganite (eg. CaMnO_3), since the valency of alkaline earth is 2+, Mn has a valency of 4+. Thus in the alkaline earth doped rare earth manganite, Mn ions can have valencies 3+ and 4+ (i.e., mixed valency).

1.2.1 Structure of manganites

Structurally there are three types of manganites namely perovskite manganites, layered manganites and pyrochlore manganites. They are shown in figure 1.3. The perovskite has the general formula ABO_3 , where 'A' and 'B' are cations. Manganites are the three dimensional perovskites. The perovskite structure consists of a lattice of oxygen octahedra with a 'B' ion at its centre. 'A' cations occupy the vacancies in the octahedra. The perovskite crystal structure is a 3D network of corner shared BO_6 octahedra. Figure 1.4 represents the typical perovskite structure.

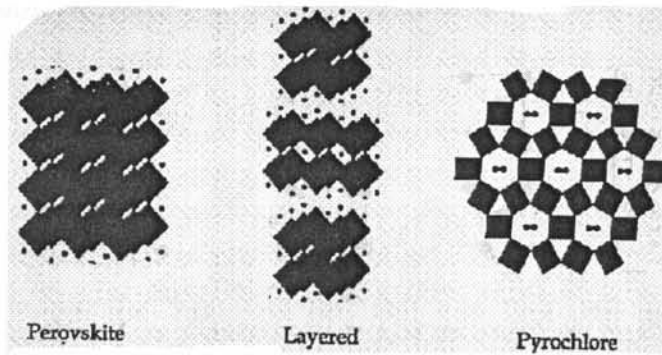


Figure 1.3 Different manganite structures

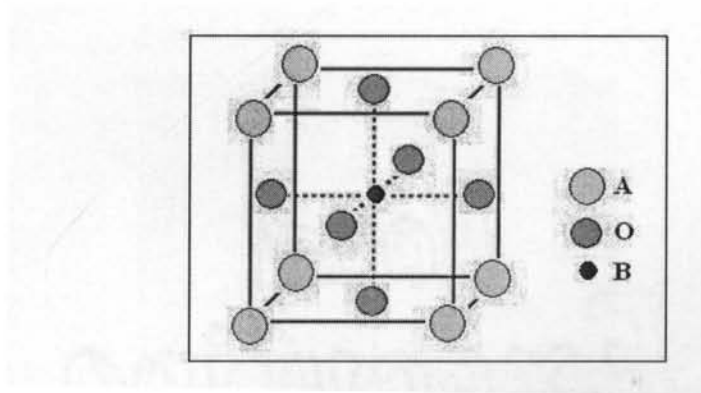


Figure 1.4 Perovskite structure

Perovskite manganites have the structural formula $A_{1-x}B_x\text{MnO}_3$, where A is the rare earth ion and B is the alkaline earth ion. $\text{La}_{2/3}\text{Sr}_{1/3}\text{MnO}_3$ is a typical example. In the crystal structure the larger rare earth or alkaline earth ion is at the centre of the cube, the smaller manganese ions at the corners and the oxygen ions at the midpoint of the cube edges (figure 1.5). The structure can be viewed in a different way; manganese at the centre, rare earth or alkaline earth ions at the corner and oxygen at the centre of the face. The Perovskite manganite structure can be regarded as a 3D network of corner shared MnO_6 octahedra with rare earth or alkaline earth metal ions occupying the holes between the octahedral as shown in figure 1.6.

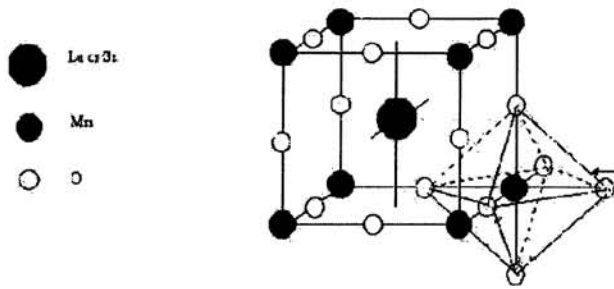


Figure 1.5 Perovskite manganite structure

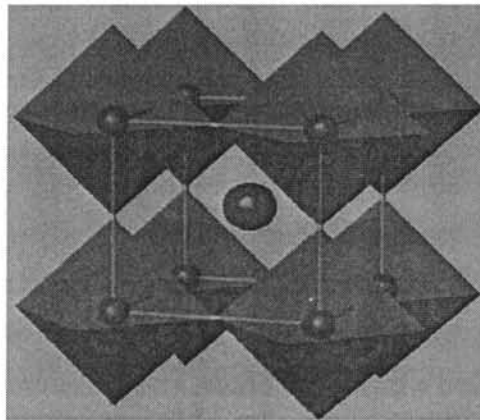


Figure 1.6 Corner shared network of MnO₆ octahedra in manganite.

In layered structure, corner shared MnO₆ octahedra forms a double layer with an insulating rock-salt layer of rare earth or alkaline earth ion (e.g. La_{2-2x}Sr_{1+2x}Mn₂O₇). In pyrochlore structure six MnO₆ octahedra forms a circle with metal ion at its centre (e.g. Tl₂Mn₂O₇).

1.2.2 Electronic structure and Crystal field splitting

In order to understand the electron transfer mechanism in manganites, we have to consider the electronic structure. The outer electronic configuration of manganese is $3d^5 4s^2$. For partially filled d shell, $l = 2$ and hence isolated ions have 5-fold degenerate orbitals $(2l+1)$, in which we can put upto 10 electrons $[2 \cdot (2l+1)]$. Filling of these levels follows Hund's first rule to minimize the Coulomb repulsion energy and electrons form a state with the maximum possible spin. The orbitals are d_{xy} , d_{xz} , d_{yz} , $d_{x^2-y^2}$ and $d_{3z^2-r^2}$ which are shown in figure 1.7.

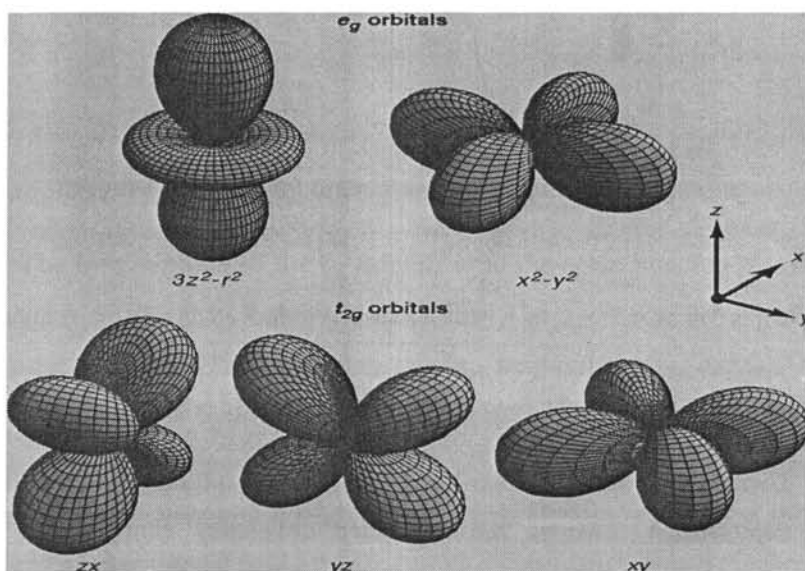


Figure 1.7 3d-orbitals

When a transition metal (TM) ion is put into a crystal, the spherical symmetry of an isolated ion is reduced and consequently some of the orbital degeneracy is lifted. This splitting of degenerate levels is called crystal field splitting. If a TM ion is introduced into a cubic crystal field, the 5-fold orbitally degenerate levels are split into two groups as shown in figure 1.8.

Three levels go down in energy, forming triply degenerate t_{2g} levels and doubly degenerate e_g levels go up [13]. The state with lower energy contains d_{xy} , d_{xz} , d_{yz} while the higher one is composed of $d_{x^2-y^2}$ and $d_{3z^2-r^2}$ [14]. The electron density of e_g orbital is directed towards the negatively charged oxygen ions (called ligands) surrounding the transition metal ion. In contrast, the three t_{2g} orbitals have lobes directed along diagonals in between the ligands as shown in figure 1.9. Hence the e_g orbitals will experience a stronger coulomb repulsion with ligands which raises their energies compared to those of the t_{2g} levels.

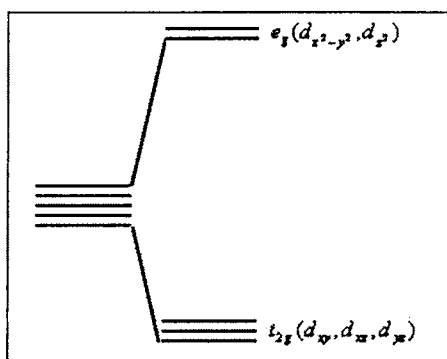


Figure 1.8 Crystal field splitting of Mn 3d orbitals

There exists another contribution to the CF splitting besides the point charge contribution. This is the so called covalency contribution, due to hybridization of the d- orbitals of the TM ion with the p orbitals of the ligands. Due to this hybridization a mixing of these orbitals occurs, which causes the splitting of the d and p levels [15]. The e_g orbitals have a rather large overlap and hence a strong hybridization with the p- orbitals of oxygen occurs (directed towards the TM ions) leading to the so called σ - orbitals. Consequently the mixing of e_g and p- orbitals will be strong and gives a corresponding upward shift of the e_g levels.

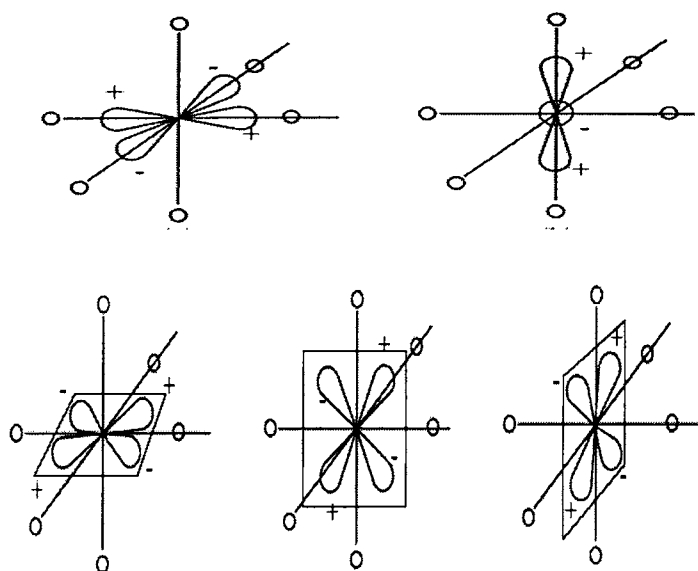


Figure 1.9 d orbital orientation with ligand oxygen atoms

The hybridization of the t_{2g} orbitals with the corresponding p- orbitals of the ligands is smaller than that of the e_g orbitals. The overlap of $p\sigma$ – orbitals with the t_{2g} orbital is zero. The remaining overlap between the t_{2g} orbitals and p – orbitals is known as π - hybridization. This overlap is permitted by symmetry but it is smaller than the σ - overlap of e_g orbitals. Thus both of the contribution to the CF, Coulomb repulsion with ligands and p- d hybridization causes the splitting of d- levels in a cubic crystal field.

From the formal valency of a TM in a given compound, the number of d electrons left on the ion is found and these electrons may be put in the CF – split levels, one after another following Hund's rule (i.e., putting as many electrons with parallel spins as possible). If total number of d- electrons $n_d \leq 3$, then, the total spin of the ion will be $S = n_d/2$. However if we have four d – electrons ($n_d=4$) a problem may arise. If the fourth electron is placed with the spin parallel to those of the first three electrons (ie according to Hund's rule), then we should place it in

a higher lying e_g level, which costs us an energy Δ_{CF} . Alternatively, the fourth electron could be put on one of the lower levels with opposite spin violating Hund's first rule.

Both these situations are met in practice. The first one leads to the so called high – spin state of a TM ion, whereas the second one to the low spin state. The relative stability of one state with respect to another is determined by the ratio of the CF splitting Δ_{CF} and the Hund's rule stabilization energy (which may be described as an on site ferromagnetic exchange interaction - $J_H \sum_{\alpha, \beta} S_{i\alpha} S_{i\beta}$ where i is the site – index and α and β are indices of different d- orbitals). If $\Delta_{CF} > J_H$, then it would be favourable to form a low - spin state, occupying the lowest CF level at the expense of Hund's rule exchange. In the opposite case the high spin state will be stabilized. Mn^{3+} (d^4) has a high spin state.

1.2.3 Orbital degeneracy and Jahn -Teller effect

Crystal field splitting is not the end of degeneracy lifting. In mixed valent manganese oxide the MnO_6 octahedra undergo a deformation called Jahn teller distortion (figure 1.10). Jahn teller theorem states that “*any non linear molecule with an electronically degenerate state will undergo spontaneous deformation so as to reduce symmetry, lower energy and thereby attain stability*”. In simple terms it is the degeneracy of the spin up and spin down states (in systems without magnetic order). All the other types of degeneracy including orbital degeneracy are forbidden and should be lifted by the corresponding decrease of symmetry. The essence of the theorem is that there is always a perturbation reducing the symmetry with a linear term representing the splitting of the degenerate levels (an energy gain) and a quadratic term representing the energy loss.

Following the standard perturbation theory of degenerate levels in quantum mechanics, the energy of the system as a function of perturbation ‘u’ has the form

$$E(u) = -gu + \frac{Bu^2}{2} \quad (1.2)$$

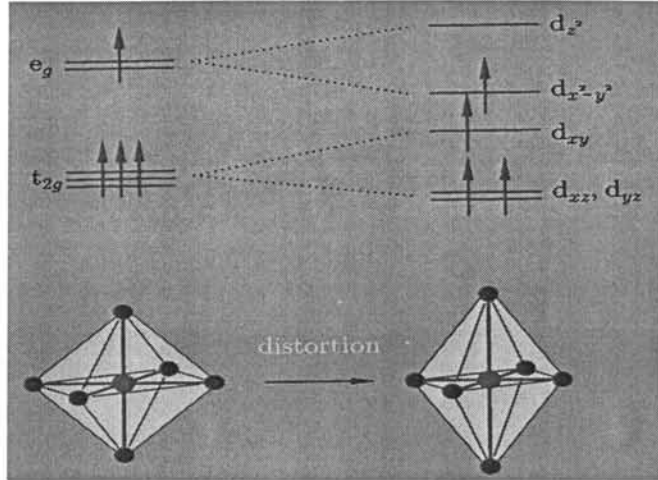


Figure 1.10 Jahn – Teller distortion in manganites

Since the neighbouring TM ions have common ligands (eg:oxygen), a local JT deformation around one centre interacts with the corresponding deformation, giving rise to correlated displacements. Consequently the symmetry of the crystal is further reduced. This is known as Cooperative Jahn Teller Effect (CJTE) or as orbital ordering [16, 17]. Jahn-Teller distortion is possible only when there is an electron in the e_g level. So in the case of manganites, Mn^{3+} is Jahn – Teller active and Mn^{4+} is Jahn-Teller inactive.

1.2.4 Tolerance factor

The extend of deformation of MnO_6 octahedron can be expressed as a geometrical quantity called tolerance factor. It is defined as the ratio of distance between rare earth or alkaline earth ion and oxygen ion to $\sqrt{2}$ times that between Mn ion and oxygen ion (equation 1.3). For a perfect cubic structure $t=1$. The properties of manganites strongly depend on tolerance factor [18].

$$t = \frac{\langle r_A \rangle + r_o}{\sqrt{2} * (r_{Mn} + r_o)} \quad (1.3)$$

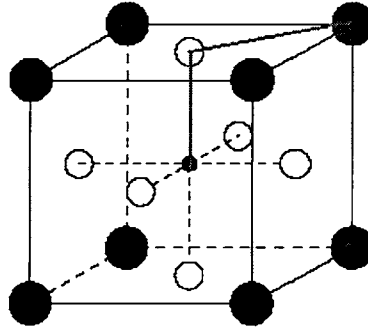


Figure 1.11 Tolerance factor calculation in manganite

1.2.5 Double exchange Mechanism

Jonker and Van Santen considered that, for the observed simultaneous good electrical conductivity and ferromagnetism, migration of electrons with their spins unpaired from Mn^{3+} to Mn^{4+} sites is a necessity [12]. This idea was put forward and developed into the double exchange model [19] by Zener (1951). In mixed valent manganites, Mn^{3+} has e_g electron while Mn^{4+} has t_{2g} electrons only. Consider an oxygen ion in between Mn^{3+} and Mn^{4+} in a system of overlapping Mn-O- Mn molecular orbital with delocalized electrons.

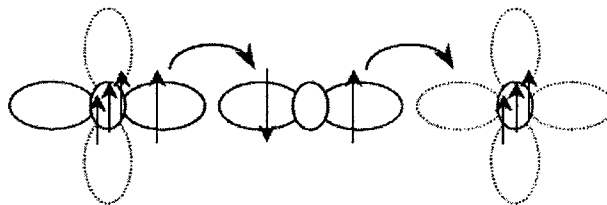


Figure 1.12 Double exchange mechanism

Zener visualized the electron transfer from one Mn ion to the adjacent Mn ion as the transfer of an electron from one Mn to the oxygen, which is in the middle, simultaneously with the transfer of an electron from the central oxygen to the other Mn ion as shown in figure 1.12. As two simultaneous processes are involved, this model is called double exchange. The configurations of the system before and after the process are given in figure 1.13.

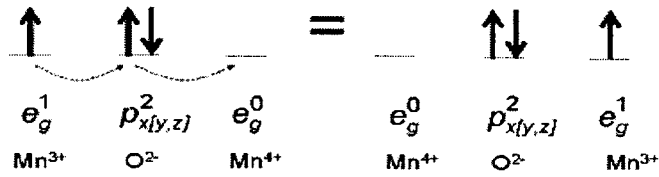


Figure 1.13 Degenerate configurations in double exchange

From figure 1.13, it is clear that the two configurations are degenerate. Due to degeneracy, no activation energy is required for electron hopping. The two states, which are degenerate in energy, are $\Psi_1 = \text{Mn}^{3+}\text{O}^{2-}\text{Mn}^{4+}$ & $\Psi_2 = \text{Mn}^{3+}\text{O}^{2-}\text{Mn}^{4+}$. A necessary condition for this degeneracy is that the spins of the two Mn d-shells (spin of the localized t_{2g} electrons) point in the same direction because the carrier spin does not change in the hopping problem and Hund's coupling punishes anti-alignment of unpaired electrons. In the double exchange mechanism, hopping of itinerant electron takes place from Mn^{3+} to Mn^{4+} via oxygen and the electrons hop easily along the bonds between the pair of ferro-magnetically ordered Mn^{3+} ($t_{2g}^3 e_g^1$) and Mn^{4+} (t_{2g}) ions, while its motion is hindered between disordered spins due to Hund's coupling [20].

The motion of e_g electrons is thus dependent on the relative spin orientation of the localized t_{2g} moments, which is described by the so called transfer integral:

$$T_{ij} \propto \cos(\phi_{ij}/2)$$

where ϕ_{ij} is the angle between moments i and j ; T_{ij} has of course a maximum when i and j are parallel to each other and a minimum when they are anti-parallel [20, 21]. The double exchange can quantitatively explain parts of the co-relation between electrical conductivity, ferromagnetism and doping level in mixed valent compounds, but fails to describe the complete phase diagram. This model can be modified to take into account lattice polarons formed on localization of an e_g electron on Mn^{3+} (Jahn Teller Distortion).

It is easily understood from the double exchange mechanism that the transport and magnetic properties of mixed valent manganites are connected to the tolerance factor. If tolerance factor is nearly one, then the Mn -O- Mn bond angle is nearly 180° . In this case, the hopping amplitude is maximum due to the effective overlapping of the orbitals. Small changes in Mn -O- Mn angle, induced by the cooperative tilting of octahedral or distortions in the octahedral, cause change in the overlap between e_g and p - orbitals and thus affect double exchange. It has been pointed out by Goodenough that ferromagnetism is also influenced by super exchange interaction. In super exchange interaction, virtual hopping of electrons takes place between occupied orbitals leading to anti-ferromagnetic coupling [14].

1.2.6 Low, Intermediate and High Bandwidth Manganites

In double exchange, e_g levels are the active ones for conductivity. These levels hybridize with oxygen p -levels constituting the conduction band, whose width is called band width. It depends on the overlap of e_g orbitals of the Mn and p levels of the oxygen [22]. The orbital's overlap decreases with the distortion and the relation between bandwidth w and Mn -O- Mn bond angle θ has been estimated as [23]

$$w \cong \cos^2\theta \quad (1.4)$$

Based on band width, manganites are classified into three namely large band width manganite, intermediate band width manganite and low band width manganite. In large bandwidth manganites (eg. $\text{La}_{1-x}\text{Sr}_x\text{MnO}_3$), the hopping amplitude of electrons in e_g band is believed to be greater than that in other manganites. The metal insulator transition temperature of these manganites is relatively large over a wide doping region. The intermediate bandwidth manganites (eg. $\text{La}_{1-x}\text{Ca}_x\text{MnO}_3$) have some characteristics of large bandwidth manganites like the presence of a robust ferromagnetic phase [24]. But in some aspects they differ from the large bandwidth manganites like the existence of charge/ orbital – ordered phase. In low bandwidth manganites ($\text{Pr}_{1-x}\text{Ca}_x\text{MnO}_3$) there is very weak ferromagnetic phase and they exhibit stable charge / orbital – ordered phase for a large doping region. The metallic ferromagnetic phase is not stabilized at zero magnetic field in low bandwidth manganites [25].

1.2.7 Charge ordering in manganites

Charge ordering is a phase transition when atoms with different oxidation states form an ordered superlattice. It is usually present in mixed valent compounds like manganites, ferrites etc. In charge ordering, electrons become localized due to ordering of cations of different charges on specific lattice sites and hence leads to insulating behaviour of the material. Wollan and Koehler discovered the charge ordering in rare earth manganites [26]. Charge ordering competes with double exchange and promotes insulating behaviour. In rare earth manganites $\text{Ln}_{1-x}\text{A}_x\text{MnO}_3$, $x=0.5$ usually favours charge ordering state because of equal number of Mn^{3+} and Mn^{4+} states. But various compositions in the range $0.3 < x < 0.75$ also exhibits charge ordering depending on Ln and A ions [27]. Charge ordering arises because the carriers are localized into specific sites below a certain temperature, called charge ordering temperature (T_{CO}), giving rise to long range order through out the crystal. At low temperatures, the rare earth manganites

are antiferromagnetically ordered with CE type charge ordering, where Mn^{3+} and Mn^{4+} ions order alternately [27]. Investigations of the charge ordering reveal extraordinary variety in the properties which include their fine sensitivity to the average size of the A-site cations, pressure, magnetic field and electric field [28].

1.2.8 Conduction mechanisms in the insulating phase of manganites

In paramagnetic insulating phase mainly three types of mechanism have been found to rule the conduction process in manganites. They are

- (1) Thermal activation or band gap model,
- (2) Variable range hopping model (VRH) and
- (3) Small polaron hopping model (SPH).

1.2.8.1 Small polarons and Large polarons

A localized electron will always distort its surroundings relative to an unoccupied site simply because of the coulombic interaction of the electron and the surrounding atoms. The potential well produced by this distortion acts as a trapping center for the self-trapped carrier. The quasi particle composed of a self-trapped electronic carrier taken together with the pattern of atomic displacements that produces the self-trapping became known as a polaron because self-trapping was first considered in ionic (polar) materials. The quasi particle (i.e the electron and the distortion) can move as a whole. The spatial extent of the self trapped states depends on the range of the interaction. In long-range electron-lattice interactions, the self-trapped electronic carrier extends over multiple sites produces large polarons [29]. The multi-site extension of the large polaron results in its itinerant motion. The radius of the large polaron decreases continuously as the strength of the electron-lattice interaction is increased. When electronic carrier is confined to a single lattice position, it is called small polaron.

1.2.8.2 Band gap model

Band gap model is widely employed in most of the semiconductors and insulators [30-32]. There is an energy gap between conduction band and valence band. If the thermal energy is sufficient to overcome the band gap, the electron becomes free to conduct. The expression for resistivity can be written in the following form

$$\rho = \rho_0 \exp(E_A/k_B T) \quad (1.5)$$

where T is the absolute temperature, ρ_0 is the value of resistivity at infinite temperature, E_A is the activation energy and k_B is the Boltzmann's constant.

1.2.8.3 Small Polaron Hopping (SPH) Model

In the case of small polarons (deeply trapped electrons), the thermal energy is not sufficient to overcome the deep potential well and to hop out of its site. Then the hopping is possible by a multi-phonon assisted process [33]. The expression for resistivity in SPH model can be obtained in the following section [34-36].

If the charge carrier must overcome an activation energy, E_A , to hop to a neighbouring site, the probability for hopping will be proportional to $\exp(-E_A/k_B T)$. From the theory of the random walk, the diffusion constant D can be estimated using this hopping probability, the frequency (ω) with which an attempt to hop is made and the site to site distance (a) is given by

$$D = \lambda \omega a^2 \exp\left(-\frac{E_A}{k_B T}\right) \quad (1.6)$$

where λ is the geometrical factor. The mobility μ is related to the diffusivity through the Nernst-Einstein relation

$$\mu = eD/k_B T \quad (1.7)$$

But conductivity is given by

$$\sigma = ne\mu \quad (1.8)$$

i.e. $\sigma = ne^2D/k_B T \quad (1.9)$

Putting value of D from equation (1.6) in equation (1.9) we get

$$\sigma = \frac{ne^2\lambda\omega a^2}{k_B T} \exp\left(-\frac{E_A}{k_B T}\right) \quad (1.10)$$

Then resistivity can be written as

$$\rho = AT \exp\left(\frac{E_A}{k_B T}\right) \quad (1.11)$$

where A is a constant given by

$$A = k_B/\lambda ne^2\omega a^2 \quad (1.12)$$

Thus in the case of materials obeying SPH model logarithm of (ρ/T) is proportional to reciprocal of temperature.

1.2.8.4 Variable Range Hopping (VRH) model

For a semiconductor or insulator at low temperatures, the predominant conduction mechanism may no longer be by thermally activated hopping to the nearest neighbour (SPH) but by variable range hopping (VRH). At low temperatures, the mechanism with the lowest barrier energy will dominate. Due to randomness in the sample, the hopping site with the lowest barrier energy will not in general be the nearest neighbour. The increased hopping distance will of course reduce the probability that the carrier will tunnel to this position; however, this is always offset by the lower barrier energy at sufficiently low temperatures. The simplest quantitative derivation of the form of variable range hopping is the following [37].

For a given site, the number of states within a range R per unit energy is given by

$$n = \frac{4}{3}\pi R^3 N(E_F) \quad (1.13)$$

where $N(E_F)$ is the density of localized states.

Thus the smallest energy difference (ΔE) for a site within a radius R is on average the reciprocal of 'n'.

$$\Delta E = \frac{1}{n} \quad (1.14)$$

i.e.
$$\Delta E = \frac{3}{4\pi R^3 N(E_F)} \quad (1.15)$$

Thus, the further the carrier hops, the lower the activation energy. The carrier has an electronic wave function exponentially localized on a particular site with a decay or localization length of ' α '. The tunneling probability that the electron will hop to a site a distance ' R ' away will contain a factor $\exp(-2R/\alpha)$. The farther is the distance; the lower is the tunneling probability. Since the hopping favours large R while the tunneling favours small R , there will be an optimum hopping distance R for which the hopping probability proportional to $\exp(-2R/\alpha) * \exp(\Delta E/k_B T)$ is a maximum. This will occur when

$$\frac{1}{R^4} = \frac{8\pi N(E_F)k_B T}{\alpha} \quad (1.16)$$

Substituting this value for R , the hopping probability and thus the conductivity is proportional to $\exp(-(T_0/T)^{1/4})$ where

$$T_0 = C\alpha^3/[k_B N(E_F)] \quad (1.17)$$

where C is a constant. Therefore the conductivity for variable range hopping can be obtained in the form

$$\sigma = \sigma_0 \exp (-T_0/T)^{1/4} \quad (1.18)$$

and resistivity is given by

$$\rho = \rho_0 \exp (T_0/T)^{1/4} \quad (1.19)$$

where ρ_0 is the resistivity at infinite temperature.

1.3 Multiferroics

1.3.1 Ferroelectricity

Ferroelectric materials display a spontaneous polarisation (at $E=0$) that can be oriented and switched by an electric field, and similarly to ferromagnets, ferroelectrics show hysteresis loop. Contrary to ferromagnets, ferroelectrics need to be insulators. Examples of ferroelectrics are perovskite materials such as barium titanate or lead zirconate titanate. The electric polarisation and the magnetisation are influenced by temperature. They are largest at low temperatures and at high enough temperatures (above the so called Curie temperature, T_c) they vanish. The origin of ferroelectricity is determined by balancing the two factors between the long range coulomb forces (which favour the ferroelectric state) and the short range repulsions of the adjacent electron clouds (which favour non polar cubic structure).

Ferroelectricity is one of the most fascinating properties of dielectric solids. Materials exhibiting ferroelectric properties must be either single crystals or polycrystalline solids composed of crystallites; they must also possess reversible spontaneous polarisation [38]. The polarisation induced by an externally applied field in normal dielectric materials is very small, with the dielectric constant usually less than 100, and its effects on other physical properties are also very small. However, there are a number of crystals with a nonsymmetrical structure that exhibit a large polarisation, with the dielectric constant up to 10^5 , under certain conditions. A ferroelectric crystal shows a reversible spontaneous

electric polarisation and a hysteresis loop that can be observed in certain temperature regions, delimited by a transition point called the Curie temperature, T_c . At temperatures above T_c , the crystal is no longer ferroelectric and exhibits normal dielectric behaviour. Ferroelectric materials usually, but not always, exist in a nonpolar state at temperatures above T_c . The dielectric constant increases very rapidly to a very high peak value at T_c . This is known as anomalous value. At $T > T_c$, anomalous behaviour follows closely the Curie-Weiss relation

$$\epsilon_r = \frac{C}{T - T_c} \quad (1.20)$$

where C is known as the Curie constant. In fact anomalous behaviour always appears near any transition point between two different phases, even at T below T_c . At the transition points, there are anomalies not only in the dielectric constant and polarisation, but also in piezoelectric elastic constants and specific heat, because of the change in crystal structure.

Ferroelectrics have reversible spontaneous polarisation. The word spontaneous means that the polarisation has a nonzero value in the absence of an applied electric field. The word reversible refers to the direction of the spontaneous polarisation, that can be reversed by an applied field in opposite direction. The spontaneous polarisation P_s usually increases rapidly on crossing the transition point and then gradually reaches a saturation value at lower temperatures. The most prominent features of ferroelectric properties are hysteresis and nonlinearity in the relation between the polarisation P and the applied electric field F .

Immediately below the Curie temperature of a continuous ferroelectric transition, the crystal spontaneously and continuously distorts to a polarized state. One would therefore expect the dielectric constant to be anomalously large in the neighbourhood of T_c , reflecting the fact that it requires very little applied field to

alter substantially the displacement polarisation of the crystal. In an ideal experiment the dielectric constant should actually become infinite precisely at T_c . A typical hysteresis loop of a ferroelectric material is shown schematically in figure 1.14.

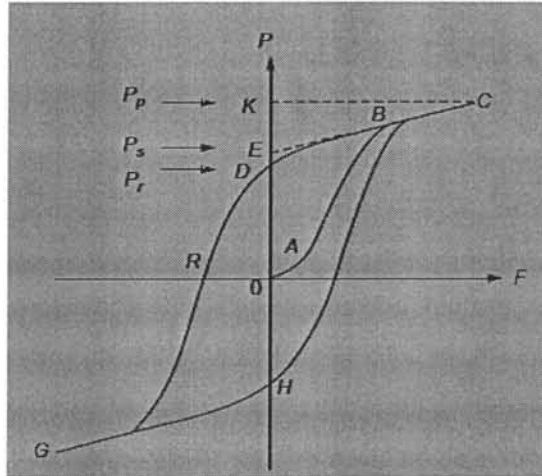


Figure 1.14 Ferroelectric hysteresis loop

When the field is small, the polarisation increases linearly with the field. This is mainly due to field-induced polarisation; because the field is not large enough to cause orientation of the domains (portion OA). At fields higher than the low-field range, polarisation increases nonlinearly with increasing field, because all domains start to orient towards the direction of the field (portion AB). At high fields, polarisation will reach a state of saturation corresponding to portion BC, in which most domains are aligned toward the direction of the poling field. Now, if the field is gradually decreased to zero, the polarisation will decrease, following the path CBD. By extrapolating the linear portion CB to the polarisation axis (or zero-field axis) at E, OE represents the spontaneous polarisation P_s and OD represents the remanent polarisation P_r . The linear increase in polarisation from P_s to P_p is mainly due to the normal field-induced dielectric polarisation. P_r is smaller than P_s because when the field is reduced to zero, some domains may

return to their original positions due to the strain situation, thus reducing these domains's contribution to the net polarisation.

For most ferroelectric materials, the component due to the normal field-induced dielectric polarisation is very small compared to the spontaneous polarisation; therefore, for most applications, this component can be ignored. The magnitude of differences between P_p and P_s in figure 1.10 is exaggerated for the purpose of clear illustration. The field required to bring the polarisation to zero is called the coercive field F_c (portion OR on zero polarisation axis). F_c depends not only on temperature, but also on the measuring frequency and the waveform of the applied field. When the field in the opposite direction decreases to zero, the polarisation is reversed, indicating that domains have already been formed before poling and that the motion of the domain walls results in the change of direction of polarisation. The hysteresis arises from the energy needed to reverse the metastable dipoles during each cycle of the applied field. The area of the loop represents the energy dissipated inside the specimen as heat during each cycle.

In general, ferroelectricity is harder to demonstrate in polycrystalline materials composed of crystallites, such as ceramics, than in a single crystal because of the random orientation of crystallites [39]. This is why in some single crystals the polarisation reverses quite abruptly to form a square loop, while in most ceramics the loop is rounded, because of the more sluggish reversal, which is partly due to the axes of the unit cells in the randomized arrangement of the nonuniform crystallites. Ferroelectric materials exhibit ferroelectric properties only at temperatures below T_c because they are polar; at temperatures above it, they are non polar. Obviously, the shape of the hysteresis loop depends on temperature.

1.3.2 Ferromagnetism

Ferromagnetism arises when the magnetic moments of adjacent atoms are arranged in a regular order i.e. all pointing in the same direction. The ferromagnetic substances thus possess a magnetic moment even in the absence of the applied magnetic field. This magnetisation is known as the spontaneous magnetisation, and it is stable only below a critical temperature, called the Curie temperature. Also, the spontaneous magnetisation decreases as the temperature increases. But above Curie temperature, the regular order disappears (i.e. the atomic magnetic moments lie randomly oriented) and the substance becomes paramagnetic. P. Weiss has developed a simple theory to account for these features of ferromagnetism. According to which i) a ferromagnetic specimen contains, in general, a number of small regions, called domains, which are spontaneously magnetised [40-42]. The magnitude of the spontaneous magnetisation of the specimen is determined by the vector sum of the magnetic moments of individual domains. ii) within each domain, the spontaneous magnetisation is due to the existence of a molecular field which tends to produce parallel alignment of the atomic dipoles (despite the effect of thermal energy). Further, this internal field is equivalent to a magnetic field H_m , which is proportional to the magnetisation M within a domain; that is

$$H_m = \lambda M. \quad (1.21)$$

where λ is a constant independent of temperature, called the molecular field constant or Weiss constant. Thus, if H is the external magnetic field, the effective field acting on an ion or atom is given as

$$H_{\text{eff}} = H + \lambda M. \quad (1.22)$$

There exists a critical temperature known as the ferromagnetic Curie temperature, θ_f , beyond which the spontaneous magnetisation vanishes. θ_f is related to the molecular field constant as

$$\theta_f = \frac{n\lambda\mu^2}{k_B} \quad (1.23)$$

where μ is the total magnetic moment per atom.

With the help of molecular field Weiss was able to explain the principle features of ferromagnetism, but he did not touch upon the problem of the origin and the nature of this field. Ideas on the nature and origin of this field were first formulated by Heisenberg on the basis of quantum theory. It is proved that the value of molecular field is large and hence it cannot be due to simple dipole – dipole interaction (i.e. due to the magnetic interaction between neighbours). Heisenberg's explanation for the large value of the molecular field is based on the non magnetic interaction, called the exchange interaction, between atoms. The exchange interaction arises as a consequence of the Pauli's exclusion principle: because of this principle we can not change the relative orientation of two spins without changing the spatial distribution of charge, clearly indicating that the interaction exists between the two atoms. It is also clear that this interaction depends upon the relative orientation of the electron spins but not on the spin magnetic moments. The energy of the interaction between atoms i, j bearing spins S_i, S_j is of the form

$$E_{ex} = -2J_e S_i \cdot S_j \quad (1.24)$$

where J_e is the exchange integral, the value of which is related to the overlap of the charge distributions of the atoms i and j , i.e. on their interatomic separation: J_e is positive for somewhat larger interatomic separations and negative for smaller ones. The above expression is called the Heisenberg model of exchange energy [43]. The exchange integral is positive for iron group of atoms and negative for others: a negative value corresponds to anti- parallel spin configuration, and thus favours non magnetism. According to Bethe J_e is positive for the iron group atoms because there exists a certain critical ratio of the distance r_{ij} between neighbouring

atoms i, j in these crystals to the radius r_{3d} of the unfilled 3d- shell. The ratio r_{ij}/r_{3d} is larger than 3 for elements like Fe, Co, Ni etc.

Actual specimens are composed of small regions called domains, within each of which the local magnetisation is saturated. The direction of magnetisation of different domains need not be parallel. Domains also form in antiferromagnetics, ferroelectrics, antiferroelectrics, ferroelastics, superconductors and sometimes in metals under conditions of a strong de Hass – van Alphen effect. The increase in the gross magnetic moment of a ferromagnetic specimen in an applied magnetic field takes place by two independent processes:

- i) In weak applied fields the volume of domains favourably oriented with respect to the field increases at the expense of unfavourably oriented domains.
- ii) In strong applied fields the domain magnetisation rotates towards the direction of the field.

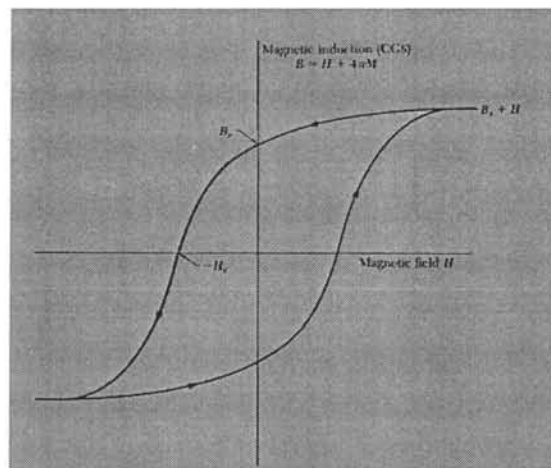


Figure 1.15 Ferromagnetic hysteresis loop

Ferromagnetic materials have a spontaneous polarisation (at $H=0$) that can be aligned and switched with a magnetic field. Unlike in paramagnetic or diamagnetic materials, the response of the magnetisation to the field is highly non

linear and represents hysteresis as shown in figure 1.15. The coercivity is usually defined as the reverse field H_c that reduces the induction B to zero, starting from saturation.

1.3.3 Multiferroism

Multiferroics are materials in which ferromagnetism, ferroelectricity and ferroelasticity occur in the same phase. This implies that they possess spontaneous magnetisation which can be reoriented by an applied magnetic field, spontaneous polarisation which can be oriented by an applied electric field and spontaneous deformation which can be oriented by an applied stress [44]. It is however, customary to exclude ferroelasticity and only consider magnetic and ferroelectric characteristics.

Electricity and magnetism were combined into one common discipline in the 19th century, culminating in the Maxwell equations. But electric and magnetic ordering in solids are most often considered separately—and usually with good reason: the electric charges of electrons and ions are responsible for the charge effects, whereas electron spins govern magnetic properties. There are, however, cases where these degrees of freedom couple strongly. For example, in the new, large field of spintronics, the effects of spins on the transport properties of solids (and vice versa) allow the possibility to control one by the other. The finding of a strong coupling of magnetic and electric degrees of freedom in insulators can be traced back to Pierre Curie, but the real beginning of this field started in 1959 with a short remark by Landau and Lifshitz in a volume of their *Course of Theoretical Physics* [45].

The situation changed soon thereafter, when Dzyaloshinskii predicted, and Astrov observed, this type of coupling, which is now known as the linear magnetoelectric effect. This was rapidly followed by the discovery of many other compounds of this class and by a rather complete classification of possible symmetry groups allowing for the effect.

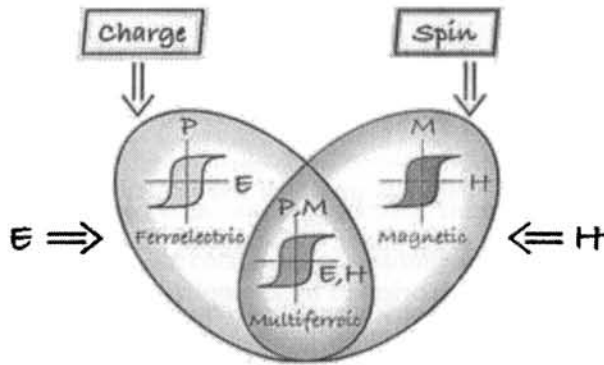


Figure 1.16 Schematic illustration of multiferroism

Multiferroic materials have attracted many scientists since the discovery of their ancestor nickel boracite ($\text{Ni}_3\text{B}_7\text{O}_{13}$) [46]. Nowadays people are trying to find a simple structure, for instance among the perovskite oxides, in order to have easier access to their fundamental behaviour. These materials can exhibit magnetism and ferroelectricity simultaneously within one phase. The coupling between the magnetisation and electric polarisation give place to magnetoelectric (ME) effects, which offer an extra degree of freedom in the design of conventional actuators or storage devices. Interesting applications can be thought of using this coupling, for instance novel multi – state memory devices that allow to write data using electric fields and to read out by means of magnetic fields. In 1992, Cohen and Krakauer used the first principle calculation to learn about the ferroelectric in the best - known perovskite structure materials such as PbTiO_3 and BaTiO_3 compounds [47]. They pointed out that both crystals showed Ti 3d – O 2p hybridization, which is very important to stabilize the ferroelectric distortion. This tendency to hybridize requires d^0 ion state (as in Ti^{4+}). Unfortunately, d orbital occupancy is required for the existing of magnetic moments and magnetic ordering, so it seems that ferroelectricity and magnetism exclude each other. Recently it was found that hexagonal manganites like YMnO_3 , LuMnO_3 exhibit multiferroic nature [48, 49].

1.3.4 Requirements of multiferroicity

The following limitations indicate why multiferroic materials are so rare.

1. Symmetries

The existence of ferroelectricity can not be separated from the existence of a structural distortion from a highly symmetric phase. This distortion removes the centre of symmetry and the atomic displacements produce a dipole per unit cell and, therefore, a spontaneous electric polarisation. There are 31 point groups that allow the spontaneous electric polarisation and 31 point groups of spontaneous magnetisation as well. 13 point groups (1, 2, 2', m, m', 3, 3m', 4, m'm', m'm2', m'm'2', 6 and 6m'm') are found in both states, allowing both properties to exist in the same phase. Many candidate materials which are not in fact ferromagnetic and ferroelectric exist in one of the allowed symmetries. Therefore it is unlikely that symmetry considerations are responsible for the scarcity of ferromagnetic, ferroelectric materials.

2. Electrical Properties

Ferroelectric material must be an insulator (otherwise an applied electric field would induce an electric current to flow, rather than causing an electrical polarisation). Ferromagnets are often metals. So the lack of simultaneous occurrence of magnetic and ferroelectric ordering is simply result a dearth of magnetic "insulators". Also there are very few antiferromagnetic ferroelectrics, even though antiferromagnets are usually insulating materials.

3. Chemistry – "d⁰–ness"

If there are no d electrons creating localized magnetic moments, then there can be no magnetic ordering of any type—either ferro-, ferri-, or antiferromagnetic. But as soon as the d- shell on the small cation is partially

occupied, the tendency for it to make a distortion, which removes the center of symmetry, is eliminated.

This could be due to the following two factors

i) Size of the small cation – It is determined that for the perovskite oxides the radii of typical d^0 B site cations are identical with those of typical B site cations with d electron occupation. Hence the size of B cations is not the deciding factor in the existence of ferroelectricity.

ii) Structural distortions- Ferroelectric material must undergo a phase transition to a low temperature phase that does not have a centre of symmetry. This is achieved in conventional perovskite ferroelectrics by an off – centre displacement of the small (B) cation from the centre of the oxygen octahedron. However for cations with certain d orbital occupancies, the tendency to undergo a Jahn - Teller distortion is strong, and will likely be the dominant structural effect. The Jahn–Teller distorted structure might have a lower driving force for off–centre displacement than the otherwise undistorted structure.

1.3.5 Applications of multiferroics

1) Multiferroic materials are of interest because of their potential applications in information storage [50, 51]. The coupling between magnetism and ferroelectricity could be exploited to induce electrical polarisation by the application of magnetic fields, and vice versa.

2) Multiferroic composite structures in bulk form are explored for high-sensitivity ac magnetic field sensors and electrically tunable microwave devices such as filters, oscillators and phase shifters (in which the ferri-, ferro- or antiferromagnetic resonance is tuned electrically instead of magnetically) [52, 53].

3) In multiferroic thin films, the coupled magnetic and ferroelectric order parameters can be exploited for developing magnetoelectronic devices [54, 55].

These include novel spintronic devices such as tunnel magneto resistance (TMR) sensors and spin valves with electric field tunable functions. A typical TMR device consists of two layers of ferromagnetic materials separated by a thin tunnel barrier ($\sim 2\text{nm}$) made of a multiferroic thin film. In such a device, spin transport across the barrier can be electrically tuned.

4) In another configuration, a multiferroic layer can be used as the exchange bias pinning layer. If the antiferromagnetic spin orientations in the multiferroic pinning layer can be electrically tuned, then magnetoresistance of the device can be controlled by the applied electric field. One can also explore multiple state memory elements, where data are stored in the electric and the magnetic polarisations [56].

1.4 Thermoelectric Power

1.4.1 Seebeck effect and other thermoelectric effects

In 1821, Thomas Seebeck discovered that a continuously flowing current is created when two wires of different materials are joined together and heated at one end. This idea is known as the Seebeck effect. Thirteen years later Jean Charles Athanase reversed the flow of electrons in Seebeck circuit to create refrigeration. This effect is known as the Peltier effect. This idea forms the basis for the thermoelectric refrigerator. Scottish scientist William Thomson (later Lord Kelvin) discovered in 1854 that if a temperature difference exists between any two points of a current-carrying conductor, heat is either evolved or absorbed depending upon the material.

The thermo electric power or Seebeck coefficient (S) is defined as the rate of change of thermoelectric potential with respect to temperature. It is usually expressed in $\mu\text{V}/\text{K}$.

$$S = -dV/dT \quad (1.25)$$

The thermoelectric efficiency of a material depends on three factors, namely Seebeck coefficient, electrical conductivity and thermal conductivity [57]. For an efficient thermoelectric material the Seebeck coefficient should be high in order to produce maximum thermoelectric voltage for unit temperature difference, the electrical conductivity should be high in order to reduce Joule's heating as small as possible and the thermal conductivity should be low for maintaining the temperature gradient. The performance parameter (called figure of merit) of a thermoelectric material is given by

$$Z = S^2\sigma/K \quad (1.26)$$

where S is the Seebeck coefficient, σ is electrical conductivity and K is thermal conductivity. The performance parameter is usually represented as dimensionless figure of merit ZT, where T is absolute temperature [49]. The value of ZT near to 1 is considered as a good thermoelectric material. The thermoelectric efficiency of a thermoelectric generator is given in equation (1.27).

$$\eta = \frac{\text{energy provided to the load}}{\text{heat energy absorbed at hot junction}} \quad (1.27)$$

And the maximum value of thermoelectric efficiency is given in equation (1.28).

$$\eta_{\max} = \frac{T_H - T_C}{T_H} * \frac{\sqrt{1+ZT}-1}{\sqrt{1+ZT} + \frac{T_C}{T_H}} \quad (1.28)$$

where T_H is the temperature of hot junction, T_C is that of cold junction, Z is figure of merit and T is absolute temperature [58]. From equation (1.28) it is clear that the thermoelectric efficiency depends on figure of merit and hence strongly depends on Seebeck coefficient.

1.4.2 Applications of thermoelectric effect.

The main applications of thermoelectric effect are power generation from waste heat, temperature sensing and eco friendly refrigeration. The power

generation from waste heat reduces global warming and hence thermoelectric power generation technology is called green technology [57].

Thermoelectric modules can also be used as thermocouples for measuring temperature or providing the temperature-sensing element in a thermostat [58]. To measure temperature the thermoelectric circuit is broken so the current quits flowing. When the current ceases, voltage is measured by a voltmeter as shown in figure 1.17. The voltage generated is a function of the temperature difference and the materials of the two wires used. Two wires used to measure temperature in this manner form a thermocouple. Thermoelectric modules can also be used as power generators [59-61]. A thermoelectric generator (figure 1.18) has a power cycle closely related to a heat engine cycle with electrons serving as the working fluid. Heat is transferred from a high temperature heat source to a hot junction and then rejected to a low temperature sink from the cold junction. The difference between the two quantities is the net electrical work produced.

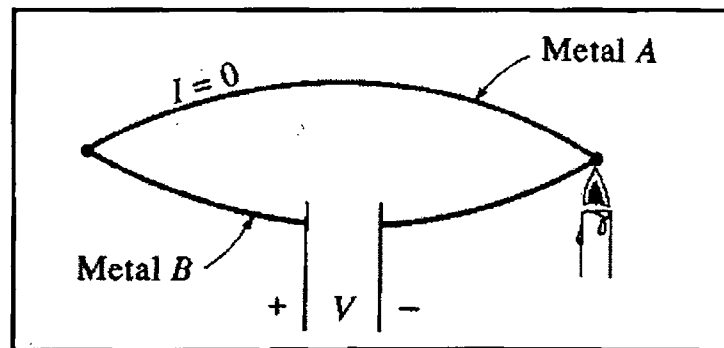


Figure 1.17 Thermocouple used for measuring temperature.

The voltage output has been increased significantly with the use of semiconductors instead of metal pairs. Some use n-type and p-type materials connected in series for greater efficiency (figure 1.19). N-type materials are heavily doped to create excess electrons, while p-type materials are used to create

a deficiency of electrons. The couple is connected in series electrically and in parallel thermally then integrated into modules. The modules are placed between ceramic plates to offer optimum stability, electrical insulation, and thermal conductivity. The modules can be either mounted in parallel to increase the heat transfer effect or stacked to achieve high differential temperatures. Thermoelectric devices can also be used as refrigerators on the basis of the Peltier effect [59-61]. To create a thermoelectric refrigerator (figure 1.20), heat is absorbed from a refrigerated space and then rejected to a warmer environment. The difference between these two quantities is the net electrical work that needs to be supplied. These refrigerators are not overly popular because they have a low coefficient of performance.

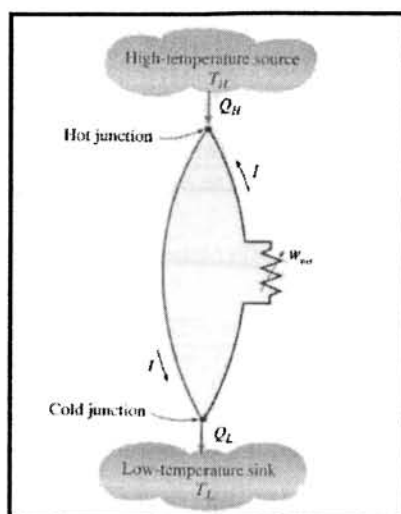


Figure 1.18 A simple thermoelectric generator

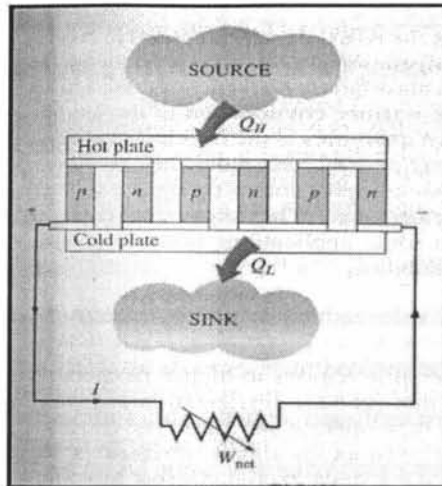


Figure 1.19 Thermoelectric generator using n and p-type materials.

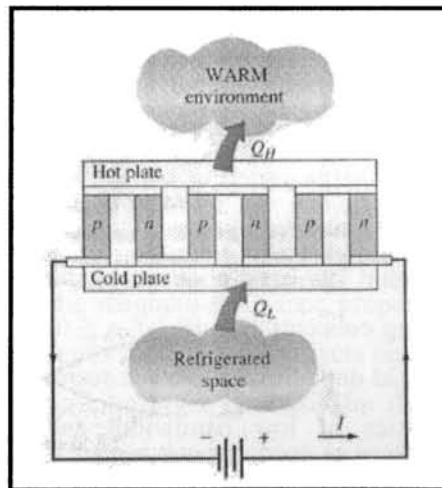


Figure 1.20 A Thermoelectric refrigerator based on the Peltier effect.

1.5 Motivation of the work

Manganites which belong to the perovskite family are technologically important because of its colossal magneto-resistance property. The electrical conductivity and ferromagnetic properties of such manganites were explained in

terms of the double-exchange interaction. However, recent investigations have shown that the double exchange alone can not explain the observed behaviour in these systems, suggesting strong electron–phonon coupling and the average size of the A and B site cations and the mismatch effect play a crucial role. Thus from physics point of view, low and intermediate band width manganites need much more attention, especially in the low temperature studies. Lanthanum ions may be replaced not only by divalent ions but also by others like alkali metal ions. There are a few reports on perovskite manganites doped with monovalent alkali-metal ions. The manganites recently attracted attention of scientific community because of multiferroic property exhibited by Ca doped rare earth manganites. Charge ordering plays a crucial role in the ferro-electricity. In large band width manganites with divalent alkaline earth cation shows charge ordering (equal amounts of Mn^{3+} and Mn^{4+} ions) at doping level $x = 0.5$. In the case of Na doping, for every amount of Na twice amount of Mn^{3+} will be converted to Mn^{4+} and hence even a small amount of Na doping results in a large number of charge carriers and consequently charge ordering can be expected at $x = 0.25$. Thus charge ordering can be easily attained by low doping without distorting the crystal structure considerably. Again low band width manganites exhibit charge ordering for a wide range of doping concentration ($0.3 \leq x \leq 0.5$). Among the low doped manganites, literature on Gd doped manganites is scarce. Thus an investigation on the multi-ferroic properties of low bandwidth and intermediate bandwidth manganites is an interesting proposition not only from a theoretical point of view but also from practical consideration.

One of the alternatives to the present day energy crisis is the so called green technology, in which energy production is based on Seebeck effect. Large Seebeck coefficient, high electrical conductivity and low thermal conductivity are prerequisites for materials with potential for applications. Metals are poor thermoelectric materials because they possess small values of Seebeck coefficient. Insulators display large values of Seebeck coefficient, but are poor electrical

conductors and are not in demand. Therefore semiconductors are considered as ideal thermoelectric materials. From literature it is seen that SrTiO_3 , a metal oxide with cubic perovskite structure, is a good thermoelectric material, while rare earth inter-metallic compounds, whose 4f levels are close to the Fermi energy and by virtue of their high density of states near the Fermi energy, scatter most of the conduction electrons, are also considered to be good thermoelectric materials. So perovskite structured manganites with large number of atoms per unit cell, large average atomic mass and large coordination number per unit atom, are capable of displaying large Seebeck coefficient. High bandwidth manganites like $\text{La}_{1-x}\text{Sr}_x\text{MnO}_3$, though they possess large value of electrical conductivity, display very small values of Seebeck coefficient. However, low band width Gd based manganite and intermediate bandwidth Na doped manganites will be materials with potential for displaying a large Seebeck coefficient. Thus an investigation on the thermo electric properties of the above mentioned manganites will be in the right direction in order to develop thermoelectric power generators.

Recently nano size effects on the material properties capture much attention among the scientific community worldwide. The increased surface to volume ratio may affect the magneto-resistance property, especially in the low temperature regime. In order to study the size effects on the transport properties of manganites we attempted a citrate gel synthesis for the Na doped intermediate band width manganites. Dielectric spectroscopy is used to elucidate the different relaxation mechanisms in the polarisation of materials. Impedance spectroscopy studies will help to gather information on the grain and grain boundary contribution of impedance, which has specific importance in the low temperature region. Manganites show hopping of charge carriers via double exchange and super exchange during their ferromagnetic and paramagnetic (or anti-ferromagnetic) phases respectively. This hopping mechanism along with the interfacial polarisation from grain-grain boundary interface contribute space charge polarisation and hence dielectric and impedance spectroscopic

measurements of the materials under study will shed light into the different polarisation mechanisms of the manganites. Hence the present investigation has following objectives.

1.6 Objectives of the work

- Synthesis of low bandwidth manganites belonging to the series of $\text{Gd}_{1-x}\text{Sr}_x\text{MnO}_3$ ($x = 0.3, 0.4$ and 0.5) by wet solid state reaction method
- Synthesis of intermediate manganites belonging to the series of $\text{La}_{1-x}\text{Na}_x\text{MnO}_3$ ($x = 0.05, 0.1, 0.15, 0.2$ and 0.25) by citrate gel method
- Analysis of structural and magneto-resistance studies of $\text{Gd}_{1-x}\text{Sr}_x\text{MnO}_3$
- Analysis of structural and magneto-resistance studies of $\text{La}_{1-x}\text{Na}_x\text{MnO}_3$
- Evaluation of the thermoelectric power of the samples $\text{Gd}_{1-x}\text{Sr}_x\text{MnO}_3$ and $\text{La}_{1-x}\text{Na}_x\text{MnO}_3$
- Study the electrical properties of samples $\text{Gd}_{1-x}\text{Sr}_x\text{MnO}_3$ and $\text{La}_{1-x}\text{Na}_x\text{MnO}_3$
- Evaluation of dielectric parameters using dielectric spectroscopic studies of the manganite samples
- Study the grain and grain boundary contribution of impedance using impedance spectroscopic studies of the manganite samples
- Correlation of results

References

- [1] Kusters R. M, Singleton J, Keen D. A, McGreevy R and Hayes W, *Physica B* **155** (1989) 362.
- [2] von Helmolt R, Wecker J, Holzapfel B, Schultz L and Samwer K, *Phys. Rev. Lett.* **71** (1993) 2331.
- [3] Chahara K, Ohno T, Kasai M and Kozono Y, *Appl.Phys. Lett.* **63** (1993) 1990.
- [4] Cheng S-W, *Nature Materials* **6** (2007) 927.
- [5] Baibich M. N, Broto J. M, Fert A, Dau F. N. V, Petroff F, Etienne P, Creuzet G, Friedrich A and Chazelas J, *Phys. Rev. Lett.* **61** (1988) 2472.
- [6] Jin S, Tiefel T. H, McCormack M, Fastnacht R. A, Ramesh R and Chen L. H, *Science* **264** (1994) 413.
- [7] Daughton J. M, *Journal of Magnetism and Magnetic Materials* **192** (1999) 334.
- [8] Tsang C, Fontana R, Lin T, Heim D, Sperisou V, Gurney B and Williams M, *IEEE Transactions on Magnetics* **30** (1994) 3801.
- [9] Daughton J. M, *IEEE Transactions on Magnetics* **36** (2000) 2773.
- [10] Daughton J. M, *Thin Solid Films* **216** (1992) 162.
- [11] Pal S. K, Madhukar A and Mitra A, *Journal of Intellectual Property Rights* **10** (2005) 99.
- [12] von Santen J. H and Jonker G. H, *Physica* **16** (1950) 599.
- [13] Robert S. Mulliken, *Physical Review* **43** (1933) 279.
- [14] Goodenough J. B, *Magnetism and Chemical Bond*, Interscience Publishing, New York, London (1963).
- [15] Siwach P. K, Singh H. K and Srivastava O. N, *J. Phys.: Condens. Matter* **20** (2008) 273201.

- [16] Pollert E, Krupicka S and Kuzwiczova E, *J. Phys. Chem. Solids* **43** (1982) 1137.
- [17] Zhao G, Conder K, Keller H and Muiller K. A, *Nature* **381** (1996) 676.
- [18] Myron B. Salamon and Marcelo Jaime, *Reviews of Modern Physics* **73** (2001)583.
- [19] Zener C, *Phys.Rev.* **81**(1951) 403.
- [20] Anderson P. W and Hasegawa H, *Phys.Rev.* **100** (1955) 675.
- [21] Kaplan T. A and Mahanti S. D, *Physics of Manganites*, Kluwer Academic / Plenum Publishers, New York (1999).
- [22] Cullen J. R and Callan E, *Phys. Rev.* **7** (1973) 397.
- [23] Tokura Y, *Colossal Magneto-resistive oxides*, Gordon and Breach Science Publishers, New York (2000).
- [24] Moritomo Y, Kuwahara H, Tomioka Y and Tokura Y, *Phys. Rev. B* **55** (1997) 749.
- [25] Coey J. M. D and Viret M, *Advances in Physics* **48** (1999) 167.
- [26] Wollan E. O and Koehler W. C, *Phys. Rev.* **100** (1955) 545.
- [27] Jirak Z, Krupicka S, Simsa Z, Dlouha M and Vratislav Z, *Journal of Magnetism and Magnetic Materials* **53** (1985) 153.
- [28] Rao C. N. R, Arulraj A, Cheetham A. K and Raveau B, *J. Phys. Condens. Matter* **12** (2000) R83.
- [29] Frolich H, *Adv. Phys.* **3** (1954) 325.
- [30] Kusters R. M, Singleton J, Keen D. A, Mc Greevy R and Hayes W, *Physica B* **155** (1989) 362.
- [31] Xiong G. C, Bhagat S. M, Dominguez M, Ju H. L, Greene R. L, Venkatesan T, Byers J. M and Rubinstein M, *Solid St. Commun.* **97** (1996) 599.

- [32] Hundley M.F, Hawley M, Heffner R. H, Jia Q. X, Neumeier J. J, Tesmer J, Thomson J. D and Wu X. D, *Appl. Phys. Lett.* **67** (1995) 860.
- [33] Young Sun, Xiaojun Xu and Yuheng Zhang, *J.Phys.Condens. Matter* **12** (2000)10475.
- [34] Cox P. A, *The Electronic Structure and Chemistry of Solids*, Oxford University Press, Oxford, (1987).
- [35] Goodenough J. B, *Progress in Solid State Chemistry* **5**, Chap. 4, Pergamon, Oxford (1970).
- [36] Mott N. F, *Conduction in non-Crystalline Materials*, Clarendon Press, Oxford (1993).
- [37] Mott N. F and Davis E. A, *Electronic Processes in non-Crystalline Materials*, Clarendon Press, Oxford (1979).
- [38] Toshio Mitsui, Taksuzaki I and Nakamura E, *An Introduction to The Physics of ferroelectrics*, Gordon and Breach, London, New York (1976).
- [39] Herbert J. M, *Ferroelectric Transducers and sensors*, Gordon and Breach science Publishers. Inc, New York (1982).
- [40] Cullity B. D, *Introduction to Magnetic Materials*, Addison Wesley Publishing Company, London (1972).
- [41] Soshin Chikazumi, *Physics of Magnetism*, John Wiley and Sons Inc., New York (1964).
- [42] Hadfield D, *Permanent Magnets and Magnetism*, John Wiley and Sons, London (1962).
- [43] Heisenberg W, *Z. Phys.* **49** (1928) 619.
- [44] Eerenstein W, Mathur N. D and Scott J. F, *Nature* **442** (2006) 759.
- [45] Landau L and Lifshitz E, *Course of Theoretical Physics, Electrodynamics of*

- ContinuousMedia*, 2nd edn., Vol. 8, Pergamon (1984).
- [46] Hill N. A, *AIP Conference Proceedings* **535** (2000) 372.
- [47] Cohen R. E and Krakauer H, *Phys. Rev. B* **42** (1990) 6416.
- [48] Hemberger J, Lunkenheimer P, Fichtl R, Krug von Niddal H. A, Tsurkan V and Loidl A, *Nature* **434** (2005) 364.
- [49] Hur N, Park S, Sharma P. A, Ahn S, Guha S and Cheong S-W, *Nature* **429** (2005) 392.
- [50] Scott J. F, *Nature Materials* **6** (2007) 256.
- [51] Ramesh R, *Nature* **461** (2009) 7268.
- [52] Masanobu Hasegawa, Takahiro Asano, Kenji Hashimoto, Gyu Chang Lee, Young Chul Park, Teiko Okazaki and Yasubumi Furuya, *Smart Mater. Struct.* **15** (2006) N124 - N128.
- [53] Vopsaroiu M, Stewart M, Fry T, Cain M and Srinivasan G, *IEEE TRANSACTIONS ON MAGNETICS* **44** (2008) 11.
- [54] Kleeman W and Borisov P, *Multiferroic and Magnetoelectric Materials for Spintronics* Springer, Netherlands (2008).
- [55] Bea H, Gajek M, Bibes M and Barthelemy A, *J. Phys.: Condens. Matter* **20** (2008) 43422.
- [56] Chow Hong Sim, Pan Z. Z and John Wang, *J. Appl. Phys.* **105** (2009) 084113.
- [57] David Michael Rowe, *International Journal of Innovations in Energy Systems and Power*, Vol. 1, no. 1 (2006).
- [58] Melcor, *Thermoelectric Engineering Handbook*. 1 February (2001).
- [59] Ohta H, *Materials Today* **10** (2007) 44.
- [60] Mahan G, Sales B and Sharp J, *Phys. Today* **50** (1997 March) 42.

[61] Boukai A. I, Bunimovich Y, Tahir-Kheli J, Yu J-K, Goddard W. A and Heath J. R, *Nature* **451** (2008) 168.

Chapter 2

Experimental Techniques

This chapter deals with the details of the experimental techniques employed for the synthesis and characterisation of gadolinium based manganite and sodium doped manganite. Brief theory supporting the experimental techniques and necessary schematic diagrams are also provided. Apart from magneto-resistance, magnetisation, dielectric and thermoelectric power studies, theoretical aspects of dielectric spectroscopy and impedance spectroscopy are also included.

2.1 Synthesis Techniques

Gadolinium based manganites are prepared using wet solid state reaction method and sodium doped lanthanum manganites are prepared using citrate gel method.

2.1.1 Wet Solid State Reaction method

Solid state reaction method is used for the preparation of polycrystalline solids from a mixture of materials in the solid form [1]. Solids do not react at room temperature over normal time scales and it is necessary to heat them to much higher temperatures (1000^o C to 1500^o C) in order to facilitate the reaction at an appreciable rate. The thoroughly dried reagents taken in stoichiometric ratio are mixed using an agate mortar. In wet solid state reaction method a liquid medium of concentrated nitric acid is used for mixing. A descriptive account is provided in chapter 3.

2.1.2 Citrate-gel Synthesis

Solution combustion synthesis (SCS) is a versatile, simple and rapid process, which allows effective synthesis of a variety of nano-sized materials [2]. This process involves a self-sustained reaction in homogeneous solution of different oxidizers like metal nitrates and fuels like urea. This process not only

yields nanosize oxide materials but also allows uniform (homogeneous) doping of trace amounts of rare-earth impurity ions in a single step.

In the gel combustion method, the raw materials, which are usually a nitrate compound and a fuel, are dissolved in water. The mixed solution is heated to change the sol to a high viscosity gel. Increasing temperature causes an exothermic combustion process. Both organic materials as a reducing agent and nitrates as an oxidation agent change the gel to a very grey fine and intensively porous substance which after calcination will yield the final product. In gel combustion, an oxidizing agent and a fuel as a reducing agent are used. Control of the oxidant to fuel ratio should create a high heat induced from the reactions. Therefore, in order to use an exothermic reaction, the selection of a suitable ratio of oxidant to fuel is very important. A non-suitable ratio of nitrate to fuel results some unwanted intermediate phases or unreacted raw materials. Generally, the fuel should be reacted slowly and act as a complex maker of cations. Complexes increase the metallic cation solubility and hence prohibit preferred crystallization during evaporation of the primary water. Manganese nitrate, lanthanum oxide and sodium carbonate were used as oxidizers while citric acid was used as fuel. Oxidizers and fuel were dissolved in deionized water and suitable amounts of dilute nitric acid and ethylene glycol were added to it. The solution is heated and when a critical temperature was reached the solution boiled, frothed, turned dark and then ignited and caught fire to give a spongy powder. A descriptive account is provided in chapter 4.

2.2 Structural Characterisation

Structural characterisation of the prepared manganite samples was carried out using X-Ray Diffraction (XRD), Transmission Electron Microscopy (TEM) along with Selected Area Electron Diffraction (SAED), Scanning Electron Microscopy (SEM) and Atomic Absorption Microscopy (AAS).

2.2.1 X-Ray Diffraction Analysis

X-ray diffraction pattern have been widely used in solid state research as a primary characterisation technique for obtaining features like crystal structure, crystallite size, lattice constants and strain.

In XRD a collimated beam of X-ray with a wavelength of 1.5406Å is incident on a specimen and is diffracted by the crystalline planes in the specimen according to the Bragg's law [3]

$$n\lambda = 2d\sin\theta \quad (2.1)$$

where λ is the wavelength of the X-ray, n is an integer, d is the inter planar spacing and θ is angle of diffraction. The intensity of the diffracted x-rays was measured and plotted as a function of diffraction angle 2θ .

Sample identification can be easily done by comparing the experimental pattern to that in the ICDD (International Centre for Diffraction Data) file. Except for single crystalline particles, the randomly oriented crystals in nanoparticles cause broadening of the diffraction patterns. The effect becomes more pronounced, when the crystallite size is of the order of few nanometers. The simplest and most widely used method for estimating crystallite size is from the Full Width at Half Maximum (FWHM) of a diffraction peak by Debye-Scherrer formula [4].

$$D = \frac{0.9\lambda}{\beta \cos\theta} \quad (2.2)$$

where 'D' is the crystallite size, λ is the wavelength of the X-radiation, β is the angular width in radians (FWHM). Rigaku Dmax- C, X-ray Powder Diffractometer was used to obtain the X-ray diffraction pattern of the samples using Cu K α lines.

2.2.2 Transmission Electron Microscopy (TEM)

Transmission Electron Microscopy is a straight forward technique to determine the size and shape of nanostructured materials as well as to obtain structural information. In TEM electrons are accelerated to 100 keV or higher projected on to a thin specimen by means of a condenser lens system, and penetrate in to the sample [5]. TEM uses transmitted and diffracted electrons which generate a two dimensional projection of the sample. The principal contrast in this projection or image is provided by diffracted electrons. In bright field images the transmitted electrons generate bright regions while the diffracted electrons produce dark regions. In dark field image the diffracted electrons preferentially form the image. In TEM, one can switch between imaging the sample and viewing its diffraction pattern by changing the strength of the intermediate lens. The greatest advantage that TEM offers are the high magnification, ranging from 50 to 10^6 and its ability to provide both image and diffraction information from a single sample.

The high magnification or resolution of TEM is given by

$$L = \frac{h}{\sqrt{2mqV}} \quad (2.3)$$

where m and q are the electron mass and charge, h the Planck's constant and V is the potential difference through which the electrons are accelerated.

The schematic of a transmission electron microscope is shown in figure (2.1). From the top down, the TEM consists of an emission source, which may be a tungsten filament, or a lanthanum hexaboride (LaB_6) source. Typically a TEM consists of three stages of lensing. The stages are the condenser lenses, the objective lenses, and the projector lenses. The condenser lenses are responsible for primary beam formation, whilst the objective lenses focus the beam down onto the sample itself. The projector lenses are used to expand the beam onto the phosphor screen or other imaging device, such as film. Imaging systems in a TEM consist of a phosphor screen, which may be made of fine (10-100 μm) particulate zinc

sulphide, for direct observation by the operator. Optionally, an image recording system such as film based or doped YAG screen coupled CCD's.

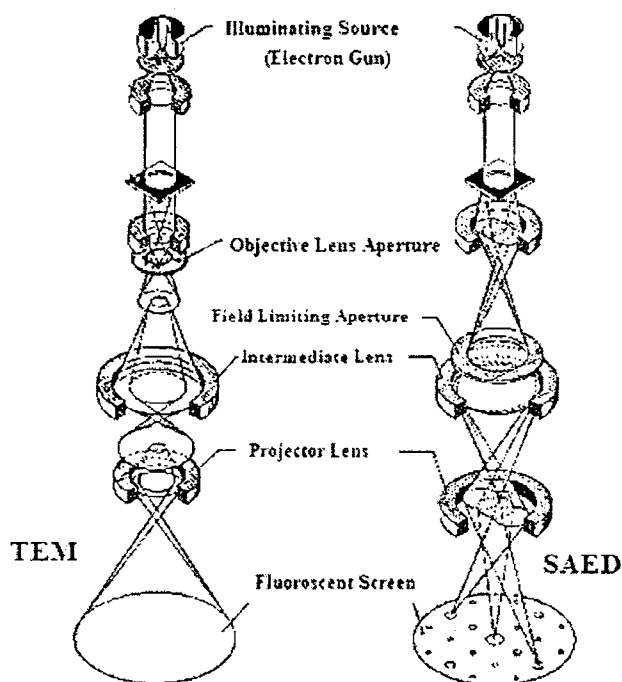


Figure 2.1 Schematic diagram of a Transmission Electron Microscope for imaging and Selected Area Diffraction Pattern

Here JOEL JEM-2200 FS TEM was used for carrying out the electron microscopic studies. Selected Area Electron Diffraction (SAED) pattern obtained along with the TEM images helped in the material characterisation to great extent.

2.2.3 Selected Area Electron Diffraction Pattern (SAED)

Selected area diffraction offers a unique capability to determine the crystal structure of individual nano materials and the crystal structure of the different parts of a sample. A small area of the specimen can be selected from a high

resolution transmission image and its electron diffraction pattern (rings or spots) can be produced on the screen of the microscope by making appropriate arrangement of the lenses of TEM. This is an optional arrangement in HRTEM. The arrangement for taking the diffraction pattern is shown in figure (2.1). The SAED allows the researcher to determine lattice constant of the crystalline material which can help in species identification. Basically diffraction patterns are distinguishable as spot patterns resulting from single crystal diffraction zones or ring patterns are obtained from the randomly oriented crystal aggregates (polycrystallites). For nanocrystallites, the diffraction patterns will be a diffused ring patterns. The 'd' spacing between lattice planes can be estimated using radius r of the diffracted rings from the relation $\lambda L = rd$, if the camera constant λL is known. The estimation of d values enables us to describe the crystal structure of the crystalline specimen [6, 7].

2.2.4 Scanning Electron Microscopy (SEM)

Scanning electron microscopy (SEM) is one of the most widely used techniques used for morphology studies and surface characterisation. It provides images of the morphology and microstructures of the bulk and nanostructured materials and devices. The resolution of SEM approaches a few nanometers and the instrument operates in the range of 10-30,000. SEM image is obtained by scanning an electron beam over the samples surface and detecting the yield of low energy electrons (secondary electrons) and high energy electrons (back scattered) according to the position of the primary beam. The secondary electrons which are responsible for the topological contrast provide mainly information about the surface morphology. The backscattered electrons which are responsible for the atomic number contrast carry information on the samples composition [8]. A new generation of SEM has emerged and is an important tool to characterize nanostructured materials. In this SEM, Field Emission Gun provides the electron beam and the resolution is as high as 1nm.

In the present study, JSM-6335 FESEM Scanning Electron Microscope was employed to analyse the morphology of samples.

2.2.5 Atomic Absorption Spectroscopy (AAS)

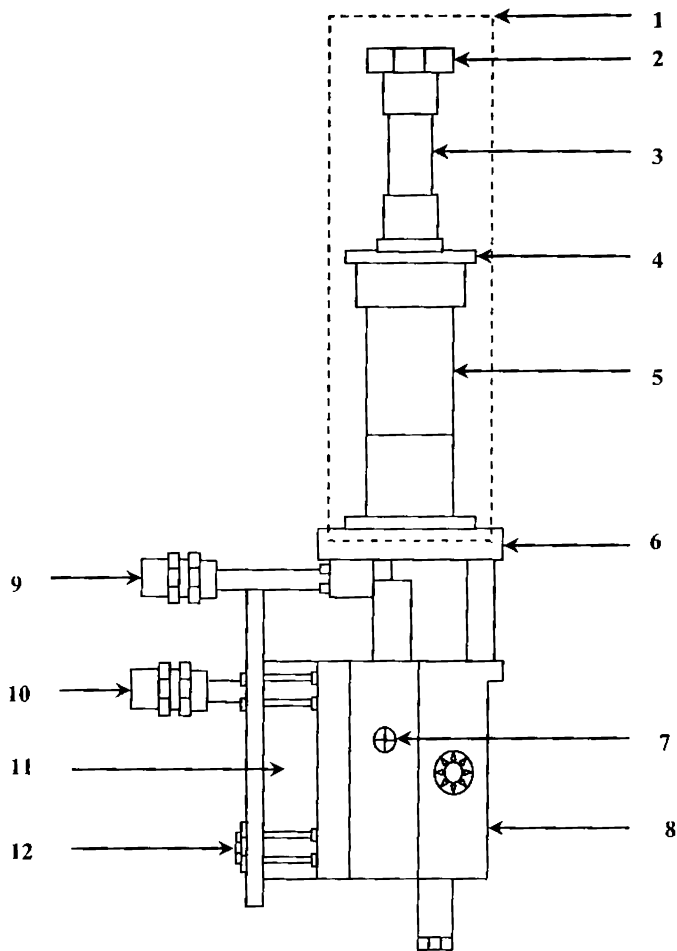
Atomic absorption spectroscopy was employed to determine the percentage of different metal elements in the manganite samples. It is generally used for the determination of the presence of metals in samples. It also measures the concentration of metals in the sample. In the elemental form, metals will absorb ultraviolet light when they are excited with heat. Each metal has a characteristic wavelength that will be absorbed and consequently intensity of incident light changes. From the change in intensity of the light, the absorbance and from the absorbance percentage of metal ions can be calculated.

2.3 DC Conductivity and Magnetoresistance Studies

2.3.1 DC Conductivity Measurements

The low temperature DC conductivity of manganite sample was taken by cooling the sample using CTI-CRYOGENICS Model 22C cryodyne cryocooler. This system uses helium as the refrigerant and is designed to interface with many kinds of apparatus that requires cryogenic temperatures. The pressure maintained in the compressor is 400 PSIG/2758 kPa. The temperature was controlled using Lake Shore Model 321 Autotuning Temperature Controller, which has a stability of $\pm 0.1\text{K}$. The pressure inside the cryocooler was maintained at 10^{-5}mB with the help of INDO VISION Vacuum Pumping System Model VPS-100.

Keithley 236 Source Measuring Unit (SMU) was used to measure the source voltage and simultaneously current was also measured. This was automated using a data acquisition system employing Interactive Characterisation Software (ICS) version 3.4.1 developed by Metrics Technology Inc. (1997).



- | | |
|------------------------------|---------------------------------------|
| 1. Cylinder | 7. Pressure Valve |
| 2. Second Stage Cold Station | 8. Crankcase (Houses Drive Mechanism) |
| 3. Second Stage Cylinder | 9. He Gas Return Connector |
| 4. First Stage Cold Station | 10. He Gas Supply Connector |
| 5. First Stage Cylinder | 11. Drive Motor |
| 6. Top Flange | 12. Electrical Power Connector |

Figure 2.2 Block diagram of D. C. Conductivity measuring system

The block diagram of the DC conductivity measuring set up used is shown in figure 2.2. In this set up the sample is considered as a resistor. A voltage was applied and the corresponding current was noted. Using Ohm's law the resistance was calculated. From the resistance R , the resistivity was found out using the expression,

$$R = \frac{\rho l}{A} \quad (2.4)$$

where ρ is the resistivity, l is the thickness of the pellet and A is the area of cross section of the pellet. Conductivity σ is the reciprocal of resistivity. Thus dc conductivity was calculated.

2.3.2 Magneto Resistance Measurement

The resistivity and magneto-resistance of the samples were measured using Keithley source meter and a sensitive voltmeter. A super conducting magnet was used for the production of large magnetic field of the order of several tesla. A detailed description of the magneto-resistance set up was given below. An insert for resistivity and magneto-resistance measurements is fabricated. It consists of a sample holder made of square OHFC copper block ($12 \times 12 \times 40 \text{ mm}^3$). On the top of each face of the copper block a cigarette paper is fixed with the help of GE varnish to electrically insulate the samples from the sample holder. Four samples can be loaded on each face. At the four corner of the block, copper strips are attached, on which PCB strips has been fixed as electrical terminals. From these terminals four uninsulated copper wires (two each for current and voltage leads) for each sample are taken for electrical contacts. The electrical contacts on samples are made with the help of silver paste or indium solder. For temperature measurement, a calibrated Cernox temperature sensor (model no. CX-1050-SD) is fixed on the sample holder with the help of GE7031 varnish. The sensor has been calibrated with respect to a calibrated Cernox temperature sensor purchased from Lakeshore Cryogenics. A pair-wise twisted manganin wire is wounded around

both the ends of copper block as a heater for homogeneous heating. This copper block is connected to about one meter long SS tube of diameter 10mm. On the SS tube, ten equally spaced copper baffles of thickness 1mm and diameter 36mm were brazed. These baffles act as a radiation shield and also utilize the enthalpy of outgoing He gas for efficient cooling. The copper wires of SWG 44 (0.081 mm diameter) are used as electrical leads from sample and temperature sensor to the room temperature end of the insert. For the sample holder heater, SWG 34 (0.234 mm diameter) copper wire is used. The voltage leads as well as current leads are pair-wise twisted separately, for each sample holder. Since large numbers of copper wire are coming from room temperature to the sample holder, it may prevent to achieve the lowest temperature. Therefore careful thermal anchoring has been done to overcome this problem.

In this insert sixteen samples can be loaded at a time. It can be used for resistivity measurements in the absence of a magnetic field in the temperature range 1.5 K - 300 K, with the general-purpose variable temperature insert. For in-field measurements same resistivity insert is used with the magnet system, which provides a magnetic field up to 100 kOe and temperature variation 1.5 K to 300 K. The samples are fixed on sample holder with the help of GE varnish. Silver paint is used for making electrical contacts. In some cases indium contacts are also used. After making the contact the insert is placed inside the cryostat (VTI or Magnet system) for resistivity and magnetoresistance measurements.

Lakeshore temperature controller (DRC-93CA) is used for measuring and controlling the temperature of the sample holder. For selecting the different samples Keithley Switching System (model 7002) is used. A nanovolt scanner card (model 7168) is used for switching between the voltage leads of different samples and a general-purpose scanner card (model 7056) for switching between the current leads. Keithley source meter (model 2400) is used for sending the current through current leads, and the voltage across the voltage leads is measured

by Keithley sensitive digital voltmeter (model 182). The automation program is written in Quick Basic. A PC (HP486) is used for controlling and automated data collection using IEEE-488 interface. The measurement is started by controlling the temperature of interest using Lakeshore temperature controller. Once the temperature is controlled the scanner selects a particular sample. Then a specified current is passed through the sample and voltage is measured across the voltage leads. After that the current direction is reversed and voltage is measured again. It cancels the off set voltage generated due to thermo emf, which is independent of the current direction. The process is repeated few times to improve the accuracy of the measurement. After that the scanner selects the next sample for measurement and repeats the process. Since one nanovolt scanner card can scan voltage of only eight samples, it is possible to carry out the measurements of a maximum eight samples at a time. Once the measurements of all the samples are completed, the temperature controller sets the next temperature. The process of measurement is repeated after achieving the required temperature stability. The collected data is plotted as resistance versus temperature.

The resistivity (ρ) is determined from the measured resistance (R) from the equation (2.4)

$$\rho = \left(\frac{A}{\ell} \right) \cdot R$$

Where, A is the area perpendicular to current direction and ℓ is the distance between the voltage leads.

The magnetoresistance ($\Delta\rho/\rho$), which is defined as

$$\frac{\Delta\rho}{\rho} = \frac{\rho(H, T) - \rho(0, T)}{\rho(0, T)} \quad (2.5)$$

can be measured in two different modes; (i) Magnetoresistance as a function of temperature at constant magnetic field, which is obtained from the measured resistance as a function of temperature in zero field and in presence of constant magnetic field. (ii) Magnetoresistance as a function of magnetic field at constant temperature can be obtained by measuring the resistance at various magnetic fields at that temperature. If the magnetic field is parallel to the current direction it is known as the longitudinal magnetoresistance and if it is perpendicular to the current direction it is known as the transverse magnetoresistance. The magnetoresistance data presented in this thesis is the longitudinal magnetoresistance.

2.4 Dielectric and Impedance measurements

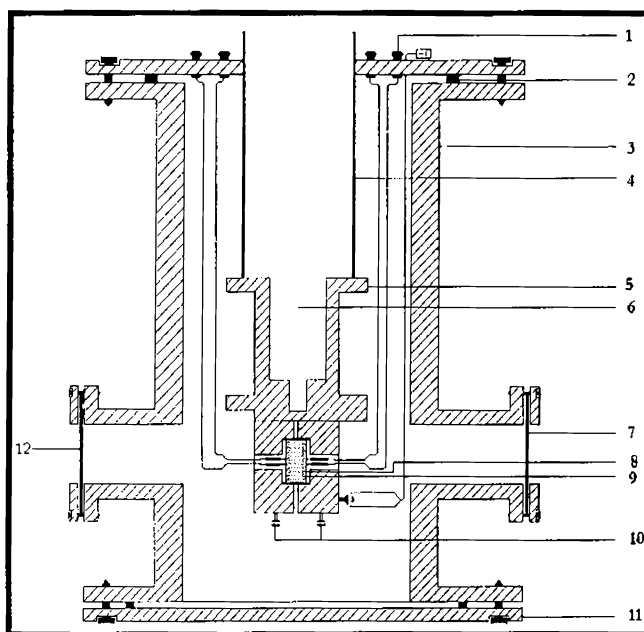
2.4.1 Dielectric Measurements

The samples for dielectric measurement were pressed by applying a pressure of 5 tones to get compact circular pellets with dimensions 12 mm in diameter and approximately 0.5 mm to 2 mm in thickness. The LCR meter is compactable with such dimension of the pellets.

The capacitance, loss factor, dielectric constant and ac conductivity were measured with frequency ranging from 100 kHz to 8 MHz. This was repeated at different temperature from 145 K to 300K in steps of 5K. The sample temperature is controlled by a temperature controller and the temperature on the sample is sensed by an Iron-Constantan (Fe-K) thermocouple on the sample. The schematic design of the cell employed for the electrical measurements is given in figure (2.3).

The cell is made up of mild steel with a cylindrical stem having provisions for fixing various attachments such as electrical connections and vacuum gauges. The cell is connected to a rotary pump to maintain a pressure of 10^{-2} Torr inside the chamber. The inner diameter of the cell is about 18 cm, and has a length of 30 cm. The sample holder is fixed at the bottom of a one-end closed metallic tube.

For the electrical conductivity and dielectric measurements, pellets are mounted on the sample holder which consists of two copper disc electrodes in between which the pelletized samples are loaded. The sample holder can be heated using a temperature-controlled heater. The dielectric permittivity measurements of the samples at different frequencies from 100 kHz to 8MHz were carried out by a Hewlett Packard 4285 A LCR meter which is automated and controlled by a virtual instrumentation package called LabVIEW. The temperature variation studies were also carried out.



- | | |
|------------------|---------------------------|
| 1. BNC | 2. Neoprine O ring |
| 3. M S Chamber | 4. SS Pipe |
| 5. Sample Holder | 6. Liquid Nitrogen Cavity |
| 7. Glass Window | 8. Metal Electrodes |
| 9. Sample | 10. Heating Filament |
| 11. MS Flange | 12. To Vacuum Pump |

Figure 2.3 Schematic diagram of cell for the dielectric and conductivity measurements

The dielectric constant of the sample can be calculated using the equation,

$$\epsilon_r = \frac{Cd}{\epsilon_0 A} \quad (2.6)$$

where d is the thickness of the pellet, C is the capacitance measured by LCR meter, A is the area of sandwiched structure and ϵ_0 is the absolute permittivity of air.

The theory involved for the evaluation of ac conductivity from dielectric constant values may be briefed as follows. Any capacitor when charged under an ac voltage will have a loss current due to ohmic resistance or impedance by heat absorption.

For a parallel plate capacitor of area of cross section A and separation d , the ac conductivity is given by the relation

$$\sigma_{ac} = \frac{J}{E} \quad (2.7)$$

Here J is the current density and E is the field density. But we know that the electric field vector

$$E = \frac{D}{\epsilon} \quad (2.8)$$

where D is the displacement vector of the dipole charges, ϵ is the complex permittivity of the material. Also the electric field intensity (E) for a parallel plate capacitor is the ratio of potential difference between the plates of the capacitor and the inter plate distance.

$$E = \frac{V}{d} \quad (2.9)$$

where V is the potential difference between the plates of the capacitor, d is the inter plate distance.

Since the current density $J = \frac{dq}{dt}$ and q is given by $\frac{Q}{A} = \frac{V\varepsilon}{d}$, where Q is the charge in coulombs due to a potential difference of V volts between two plates of the capacitor.

$$J = \frac{dq}{dt} = \frac{d}{dt} \left(\frac{V\varepsilon}{d} \right) = \frac{\varepsilon}{d} \frac{dV}{dt}$$

$$J = \frac{\varepsilon}{d} \frac{dV}{dt} = \frac{\varepsilon}{d} \cdot Vj\omega \quad (2.10)$$

Substituting for E and J from the equations (2.9) and (2.10) we get

$$\sigma_{ac} = \frac{J}{E} = \varepsilon j\omega \quad (2.11)$$

Considering ε as a complex entity of the form $\varepsilon' \approx (\varepsilon' - j\varepsilon'')$ and neglecting the imaginary term in the conductivity we can write

$$\sigma_{ac} = \omega\varepsilon'' \quad (2.12)$$

But the loss factor or dissipation factor in any dielectric is given by the relation

$$\tan\delta = \frac{\varepsilon''(\omega)}{\varepsilon'(\omega)} \quad (2.13)$$

Hence from the dielectric loss and dielectric constant, ac conductivity of these samples can be evaluated using the relation

$$\sigma_{ac} = 2\pi f \tan\delta \varepsilon_0 \varepsilon_r \quad (2.14)$$

where f is the frequency of the applied field and $\tan\delta$ is the loss factor [9].

The ac electrical conductivity of powder samples was calculated utilizing the dielectric parameters by using the equation (2.14). After obtaining capacitance

and dielectric loss from the instrument, LabVIEW software first calculates the dielectric constant and then evaluates the ac conductivity.

2.4.2 Dielectric spectroscopy (Cole-Cole Plot)

In order to study the dielectric behaviour, it is customary to plot ϵ' , ϵ'' or $\tan\delta$ against frequency. A more convenient method is the Argand diagram or complex locus diagram in which the imaginary part of the complex dielectric constant is plotted against the real part at the same frequency. Kenneth S. Cole and Robert H. Cole applied this method to dielectric and hence it is often called Cole-Cole plot [10 - 13].

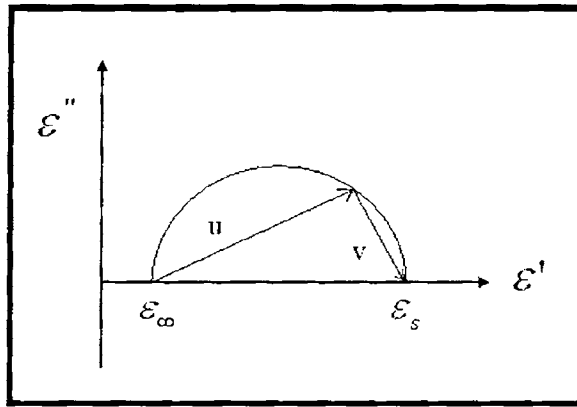


Figure 2.4 Cole-Cole Plot

For a dielectric with single relaxation time, the Cole-Cole plot is a semicircle with its center on the real axis and intercepts at ϵ_0 and ϵ_∞ on this axis.

From the figure, we can write

$$u + v = \epsilon_s - \epsilon_\infty \quad (2.15)$$

where the quantities u , v considered as vectors in the complex plane are perpendicular, their vector sum being the constant real quantity $(\epsilon_s - \epsilon_\infty)$. The right angle included by these vectors is therefore inscribed in a semicircle of diameter

$(\epsilon_s - \epsilon_\infty)$ as shown in the figure (2.4). This semicircle is then the locus of the dielectric constant as ω varies from 0 to ∞ .

But,
$$\epsilon^* - \epsilon_\infty = \frac{(\epsilon_s - \epsilon_\infty)}{(1 + j\omega\tau)} \quad (2.16)$$

and therefore,

$$u + v = (\epsilon^* - \epsilon_\infty)(1 + j\omega\tau) \quad (2.17)$$

Many materials, particularly long chain molecules and polymers shows a broader dispersion curve and lower maximum loss than would be expected from the Debye's relationship. K.S Cole and R.H Cole suggested that in this case the permittivity might follow the empirical relation,

$$\epsilon^* - \epsilon_\infty = \frac{(\epsilon_0 - \epsilon_\infty)}{1 + (j\omega\tau_0)^{1-\alpha}} \quad (2.18)$$

where τ_0 is the average relaxation time and α is the spreading factor ($0 \leq \alpha \leq 1$) of actual relaxation time τ about its mean value τ_0 .

For $\alpha = 0$ the above equation reduces to Debye's equation. The center of the circular arc lies below the real axis and when $\alpha = 0$ the above expressions become consistent with Debye's model. From the expression for ϵ'' , it is clear that at $\omega = 1/\tau$, it becomes maximum and the value is given by

$$\epsilon''_{\max} = \frac{(\epsilon_0 - \epsilon_\infty) \tan[(1-\alpha)\pi/4]}{2} \quad (2.19)$$

From the Cole-Cole plot, the dispersion parameters like static dielectric permittivity, optical dielectric permittivity and spreading factor ' α ' can be evaluated [14].

Using the dielectric values obtained from the LCR meter measurement, the Cole- Cole plots of the samples were drawn and using a non linear least square fitting program (C-language) the different dispersion parameters were evaluated.

2.4.3 Impedance Spectroscopy

Impedance spectroscopy is a powerful method of characterizing many of the electrical properties of materials and their interfaces with electronically conducting electrodes. It may be used to investigate the dynamics of bound or mobile charges in the bulk or interfacial regions of any kind of solid or liquid material; ionic semiconducting, mixed electronic-ionic, and even dielectrics. The common approach is to measure Z directly in the frequency domain by applying an ac voltage and measuring the phase shift and amplitude, or real and imaginary parts of the resulting current at the corresponding frequencies.

The concept of electrical impedance was introduced by Oliver Heaviside in 1880 and was soon after developed in terms of vector diagrams and complex representation by C P Steinmetz. In the case of ideal resistors, the opposition is independent of frequency of the applied voltage. But in real situations the opposition depends on the frequency of the applied voltage and this opposition is called impedance. The impedance of the system $Z(\omega)$, is defined as the ratio of the applied voltage, in the frequency domain, $v(\omega)$ to the measured current $i(\omega)$.

$$Z(\omega) = v(\omega)/i(\omega) \quad (2.20)$$

It is a complex quantity and is given by

$$Z^*(\omega) = Z' + iZ'' \quad (2.21)$$

where Z' is the real component and Z'' is the imaginary component. The real and imaginary components are given by the rectangular coordinates

$$\begin{aligned} Z' &= Z \cos\varphi \\ Z'' &= Z \sin\varphi \end{aligned} \quad (2.22)$$

with the phase angle φ and modulus $|Z|$ given by

$$\varphi = \tan^{-1} \left[\frac{Z''}{Z'} \right] \quad (2.23)$$

and
$$|Z| = \sqrt{(Z')^2 + (Z'')^2} \quad (2.24)$$

The phase angle is measured by comparing the ratio of potential and current wave forms. Impedance data is typically represented in two types of plots namely Nyquist or Argand plot and Bode plot. The Nyquist plot is a graphical portrayal of complex numbers in the Argand plane; where the X-axis represents the real part and the Y-axis represents the imaginary part of the complex number. In the case of plotting impedance data, the positive Y-axis conventionally represents the negative imaginary portion of the impedance and there is a complex impedance point for every frequency at which the impedance was measured, creating a plot with impedance features. The Nyquist plot will give a semicircle or a set of semicircles depending on the different contributions to impedance. The Bode plot consists of two graphs: one with the phase of the admittance (the negative phase of the impedance) on the Y-axis and the logarithmic frequency on the X-axis, the other with the logarithm of the magnitude of the impedance on the Y-axis and the logarithmic frequency on the X-axis.

Equivalent circuits are traditionally used to model AC impedance data [15-17]. An equivalent circuit is an electrical circuit with the same impedance spectrum as the experimental data. The values and arrangement of the circuit elements ideally represent physical properties or phenomena. Changes in the values of circuit elements can help in understanding system response. The complex nonlinear least squares (CNLS) method is one of the most common approaches for modeling impedance data. This is partially due to commercial fitting programs like Z plot and LEVM which use the CNLS method. CNLS is used to fit the real and imaginary parts or the magnitude and phase of experimental impedance or admittance data to an equivalent circuit or a rational function. It is a convenient method for fitting data to functions or circuits with many free parameters. The primary concerns with CNLS are its sensitivity to initial parameters, the correct choice of the number of free parameters, and the possibility of convergence to a local minimum. The choice of minimization algorithm is also an important consideration.

Applications of impedance spectroscopy

It is used in the characterisation of ceramic materials. In polycrystalline solids, transport properties are strongly affected by microstructure, and impedance spectra usually contain features that can be directly related to microstructure. Polycrystalline materials usually have less than theoretical density and disoriented grains. In the simplest case, these effects would lead to purely geometric reductions in the conductivity with respect to the single crystal. In addition, impurities may be present as a secondary phase at the grain boundaries. The grain boundary resistance can be calculated using impedance spectroscopy. It is used in the design of solid state devices like Electrolyte - Insulator - Semiconductor (EIS) Sensor, Solid state batteries, photoelectrochemical solar cells etc. It is used to determine the optimum electrode material and preparation procedures for these devices. It is also used to find the corrosion rate of materials [18].

Using an HP 4192A impedance meter, the real and imaginary impedance of the samples were measured at different frequencies (100 Hz to 6 MHz) in the temperature range 305 K – 345 K. Using the measured real and imaginary values, impedance spectrum were drawn and bulk impedance, bulk capacitance and relaxation time were evaluated.

2.5 Magnetic Characterisation

Magnetic characterisation of the manganite samples has been carried out using vibrating sample magnetometer (model EG & G Par 4500).

2.5.1 Vibrating Sample Magnetometer (VSM)

A vibrating sample magnetometer (VSM) operates on Faraday's Law of induction, which tells us that a changing magnetic field will produce an electric field. This electric field can be measured and provides us information about the changing magnetic field. A VSM is used to measure the magnetic properties of

magnetic materials. Using VSM the hysteresis loop parameters namely saturation magnetisation (M_s), coercive field (H_c), remanence (M_r) and squareness ratio (M_r/M_s) can be derived. The schematic of a vibrating sample magnetometer is given in the figure 2.5.

In a VSM, the sample to be studied is placed in a constant magnetic field. If the sample is magnetic, this constant magnetic field will magnetize the sample by aligning the magnetic domains or the individual magnetic spins, with the field. The stronger the constant field, the larger the magnetisation. The magnetic dipole moment of the sample will create a magnetic field around the sample, sometimes called the magnetic stray field. As the sample is moved up and down, this magnetic stray field change as a function of time and can be sensed by a set of pick up coils. A transducer converts a sinusoidal ac drive signal provided by a circuit located in the console into a sinusoidal vertical vibration of the sample rod and the sample is thus made to undergo a sinusoidal motion in a uniform magnetic field. Coils mounted on the pole pieces of the magnet pick up the signal resulting from the sample motion.

The alternating magnetic field will cause an electric field in the pick up coil as according to Faradays law of induction, the current will be proportional to the magnetisation of the sample. The greater the magnetisation, the greater is the induced current. The induction current is amplified by a trans-impedance amplifier and a lock-in amplifier. The various components are interfaced via a computer. Controlling and monitoring software, the system can tell how much the sample is magnetized and how magnetisation depends on the strength of the constant magnetic field. For particular field strength, the corresponding signal received from the probe is translated into a value of magnetic moment of the sample. When the constant field varies over a given range, a plot of magnetisation versus magnetic field strength is generated.

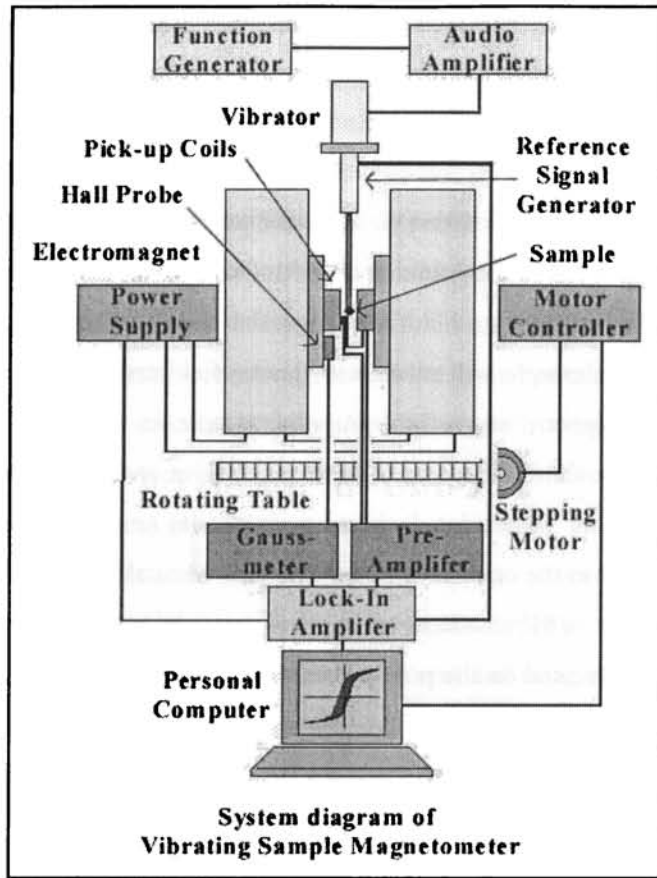


Figure 2.5 Schematic diagram of Vibrating Sample Magnetometer

The dipole moment is induced in the sample when it is placed in a uniform magnetic field M . Then the amount of magnetic flux linked to the coil placed in the vicinity of this magnetic field is given by

$$\phi = \mu_0 n \alpha M \quad (2.25)$$

where ' μ_0 ' is the permeability of free space, ' n ' the number of turns per unit length of coil and α represents the geometric moment decided by position of moment with respect to coil as well as shape of coil.

Anharmonic oscillator of the type,

$$Z = Z_0 + A \exp(j\omega t) \quad (2.26)$$

induces an emf in the stationary detection coil. The induced emf is given by

$$V = -\frac{d\phi}{dt} = -j\omega\mu_0 nMA \left(\frac{\partial\alpha}{\partial z}\right) e^{j\omega t} \quad (2.27)$$

If amplitude of vibration (A), frequency ω and $\frac{\partial\alpha}{\partial z}$ are constant over the

sample zone then induced voltage is proportional to the magnetic moment of the sample. A cryogenic setup attached to the sample permits low temperature measurements. This is the basic idea behind VSM [19-21].

2.5.2 Field Cooled and Zero Field Cooled Measurements

Zero Field Cooled (ZFC) measurements provide a means of investigating various magnetic interactions. First a sample is cooled to liquid helium temperatures under zero applied magnetic fields. Then small uniform external field is applied and the net magnetisation is measured while heating the sample at a constant rate. For small magnetic particles, this curve has a characteristic shape. As the particle cools in a zero applied magnetic field, they will tend to magnetise along the preferred crystal directions in the lattice, thus minimizing the magneto-crystalline energy. Since the orientation of each crystallite varies, the net moment of the system will be zero. Even when a small external field is applied the moments will remain locked into the preferred crystal directions, as seen in the low temperature portion of the ZFC curve. As the temperature increases more thermal energy is available to disturb the system. Therefore more moments will align with the external field direction in order to minimize the Zeeman energy term. In other words, thermal vibration is providing the activation energy required for the Zeeman interaction. Eventually the net moment of the system reaches a maximum where the greatest population of moments has aligned with the external field. The peak temperature is called blocking temperature T_B which depends on

particle volume. As temperature rises above T_B , thermal vibrations become strong enough to overcome the Zeeman interaction and thus randomize the moments [22].

Field cooled measurements proceed in a similar manner to ZFC except that the constant external field is applied while cooling and heating. The net moment is usually measured while heating. However, the FC curve will diverge from the ZFC curve at a point near the blocking temperature. This divergence occurs because the spins from each particle will tend to align with the easy crystalline axis that is closest to the applied field direction and remain frozen in that direction at low temperature. Thermal Remnant Magnetisation (TRM) curves are obtained by cooling field to the measurement start temperature. The field is then removed and the magnetisation is recorded as a function of temperature while the sample is heated. It is important to note that ZFC, FC and TRM are non equilibrium measurements [23]. Care must be taken to ensure the same heating rate during the measurements in order to compare the measurements of different samples.

In the present investigation, FC-ZFC modes of the VSM were employed for the measurements. In the ZFC mode, the sample was cooled in the absence of a field and the magnetisation was measured during warming, by applying a nominal field of 50 Oe, 100 Oe and 200 Oe. In the FC mode, the sample was cooled in presence of a field and the magnetisation was measured during warming, under the same field values as mentioned in the ZFC mode.

2.6 Thermoelectric power measurements

The Seebeck coefficient (thermoelectric power) of the manganite samples was measured by differential method. In this method, one end of the sample is heated to have a small temperature gradient ΔT across the sample. The thermo - emf ΔV is measured across the sample against a reference (refn) material by making a refn-sample-refn thermocouple. Then thermoelectric power (S) of the

sample is calculated as $S_{\text{sample}} = S_{\text{refn}} - S_{\text{measured}}$, where S_{measured} is $\Delta V/\Delta T$. The precision and accuracy of the thermoelectric power rely on how precise and accurate the ΔV and ΔT are. Proper electrical contact between the sample and the refn is needed to measure voltages precisely. Hence the wires of refn are spot welded to the samples. One end of the sample is clamped to the cold head. A sensor and a heater are mounted on the other end of the sample. Simplifications have been introduced by several means for an easy and faster sample mounting such as sandwich method [24, 25]. Very low temperature is obtained by using a cooling power system 4 K close cycle refrigerator. Using a controller of the type DRC – 93C from Lakeshore Cryotronics, temperature difference is controlled so as to produce constant thermo electric voltage by the thermocouple. The accuracy of the control is better than $1\mu\text{V}$. This corresponds to 45 mK at 300 K and to 100 mK below 10 K for chromel – AuFe (0.07%). All the wirings running from the room temperature are anchored and terminated at a flexible printed circuit board (PCB) mounted on the cold finger. Wires from the setup are soldered on the PCB at respective places. The length and diameter of the wires are optimised in order to minimise excess heat leak. Wires of diameter less than $120\ \mu\text{m}$ with a minimum of 10 cm length are used. The emf developed across the thermocouple is measured precisely using a Keithley nano voltmeter and a scanner system.

References

- [1] Anthony R. West, *Solid State Chemistry and its applications*, Wiley and Sons, New York (1984).
- [2] Aruna T. S and Mukasyan A. S, *Current Opinion in Solid State and Materials Science* **12** (2008) 44.
- [3] Charles Kittel, *Introduction to Solid State Physics*, John Wiley and Sons, New York (1997).
- [4] Cullity B. D, *Elements of X-ray diffraction*, Philippines, Addison-Wesley Publishing Company, Inc., 2nd Edition. California (1978).

- [5] Watt M, *The Principles and Practice of Electron Microscopy*, 2nd Edition, Cambridge University Press, Cambridge (1997).
- [6] Schamp C. T, Jesser W. A, *Ultramicroscopy* **103** (2005) 165.
- [7] Lawrence E Murr, *Electron and Ion Microscopy and Microanalysis, Principles and Applications*, Mc.Graw Hill Inc., New York, 1982.
- [8] Linda C. Sawyer and David T. Grubb, *Polymer Microscopy*, 2nd Edition. Chapman and Hall, London (1987).
- [9] Dormann J. L and Fiorani D, *J. Magn. Magn. Mater.* **140-144** (1995) 415.
- [10] Debye P, *Polar Molecules*, Dover, New York (1929).
- [11] Cole K.S and Cole R.H, *J. Chem. Phys.* **9** (1941) 34.
- [12] Veera V. Daniel, *Dielectric Relaxation*, Academic, London (1967).
- [13] Hill N.E, Vaughan W. E, Price A. H and Mansel Davies, *Dielectric properties and Molecular Behaviour*, Van Nostrand Reinhold, London (1969).
- [14] Sagar S, Saravanan S, Suresh Kumar S, Venkatachalam S and Anantharaman M. R, *J. Phys. D:Appl. Phys.* **39** (2006) 1678.
- [15] Sluyters-Rehbach M, *Pure & Applied Chemistry* **66** (1994) 1831.
- [16] Macdonald J. R, *Impedance Spectroscopy*, John Wiley and Sons, New York (1987).
- [17] Franceschetti, Donald R, and J. Macdonald J. R, *Journal of Electroanalytical Chemistry* **82** (1977) 271.
- [18] Barsoukov E and Macdonald J. R, *Impedance spectroscopy – Theory, Experiment and Applications*, Wiley – Interscience , New Jersey (2005).
- [19] Simon Foner, *Rev. Sci. Instrum.* **30** (1959) 548.
- [20] Joseph A. Pesch, *Rev. Sci. Instrum.* **54** (1983) 480.
- [21] Krishnan R. V and Banerjee A, *Rev. Sci. Instrum.* **70** (1999) 85.
- [22] Denardin J. C, Brandl A. L, Knobel M, Panissod P, Pakhomov A. B, Liu H and Zhang X. X, *Phys. Rev. B* **65** (2002) 064422.
- [23] Aparna Roy, Srinivas V, Ram S and De Toro J. A, *J. Appl. Phys.* **100** (2006)

094307.

[24] Samuel E. I, Seshu Bai V, Sivakumar K. M and Ganesan V, *Phys. Rev. B* **59** (1999) 7178.

[25] Sivakumar K. M, Singh R. K, Gaur N. K and Ganesan V, Proceedings of the 21st International Conference on Thermoelectrics , ICT'02 (2002) 337.

Chapter 3

Investigation on the Magnetoelectric Transport Properties of Gadolinium Based Manganites

3.1 Introduction

Manganites and Cobaltites belong to the perovskite class of materials. They exhibit interesting magnetic, electrical and structural properties. These class of materials have been in the forefront of material research for three decades or so. Among them, manganites occupy a special position because of its application potential as catalysts, as electrode materials and in various other applications like bolometer etc. [1 - 4]. Since the discovery of CMR in manganites research on these class of materials is on the rise. They exhibit simultaneous phase transitions namely from ferromagnetic to paramagnetic and metal to insulator. They also display electronic and structural peculiarities including orbital and charge ordering, formation of local moments and Jahn Teller distortions [5, 6]. Such richness combined with their relatively simple structure make them ideal for investigating the general principles that govern these properties.

Charge ordering has a prominent role in the transport properties of manganites. Charge ordered state exists for a wide doping range for low bandwidth manganites. Metal to insulator (M-I) transition is observed in the case of Lanthanum (high and intermediate bandwidth) manganites at near room temperatures. However manganites doped with smaller rare earth ions like Gd, Pr (low bandwidth manganites) exhibited metal insulator transition only at very low temperatures [3, 7]. At the same time when the M-I transition is attained for low average radius A-site cation perovskites, higher magnetoresistance ratio is obtained. This makes rare earth based manganites very attractive for further investigation. Relatively, fewer studies are reported on perovskites based on heavy

rare earths. This is because it was presumed that smaller radius cation in the A site does not result in M-I transition at near room temperature. Reports on heavy rare earth doped manganite are scarce in literature. Compositions $x=0.3$ to 0.7 exhibit charge ordering and hence was chosen for magnetoresistance study.

The evaluation of conducting properties in the paramagnetic regime will help probe the mechanism of conduction in these compounds. The conduction mechanism in the paramagnetic phase is a matter of controversy as different schools of thought propose different models for conduction. For example, data on certain compounds were fitted with purely activated law by R. M. Kusters et al., G. C. Xiong et al. and M. F. Hundley et al. [8 -10]. While some authors proposed small polaron hopping conduction mechanism (SPH) over an extended temperature ranges [11-15]. At the same time N. F. Mott and E. A. Davies used the Variable Range Hopping mechanism (VRH) for the whole temperature range [16, 17]. The electrical conductivity studies in the low temperature regime will enable to propose a plausible mechanism for conduction in manganites. This chapter deals with the structural, dc conductivity, magnetisation and magnetoresistance studies of $Gd_{1-x}Sr_xMnO_3$ ($x=0.3$, $x=0.4$ and $x=0.5$), which was prepared by wet solid state reaction method.

3.2 Sample preparation and structural characterization

$Gd_{1-x}Sr_xMnO_3$ ($x=0.3$, $x=0.4$ and $x=0.5$) samples are prepared using wet solid state reaction method. Stoichiometric amounts of Gd_2O_3 , $SrCO_3$ and MnO_2 were mixed in concentrated nitric acid. The solution was heated, boiling off the excess nitric acid. This precursor was calcinated in air at $900^\circ C$ overnight. The remaining black powder was pressed into pellets and sintered at $1200^\circ C$ in air for 3 days [7, 18]. The sample was analyzed by means of X-Ray Powder Diffractometer (Rigaku Dmax - C) using Cu-K α radiation ($\lambda = 1.5414 \text{ \AA}$). The X-ray diffraction pattern of the samples is shown in figure 3.1. From the XRD pattern it is clear that the sample $Gd_{0.5}Sr_{0.5}MnO_3$ is single phasic with an

orthorhombically distorted perovskite structure. The scanning electron microscopy studies were carried out using a field emission scanning electron microscope JSM 6335 FESEM at 50 kV. The SEM pictures of GSMO sample are shown as figures 3.2(a) to 3.2(c). The SEM images indicate that the size of particles is in the micron regime. From atomic absorption spectroscopy (AAS) and energy dispersive spectroscopy (EDS), the stoichiometry of the elements in the sample was evaluated and is in good agreement with theoretical values.

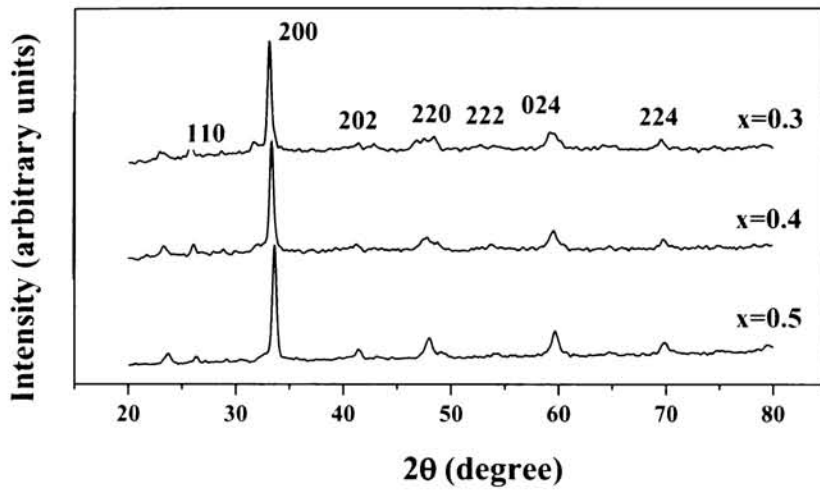


Figure 3.1 X ray diffraction pattern of $Gd_{1-x}Sr_xMnO_3$ ($x=0.3$, $x=0.4$ and $x=0.5$)

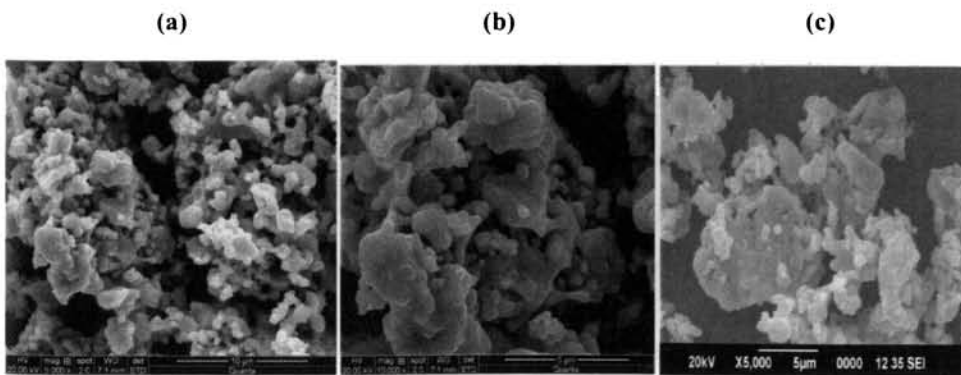


Figure 3.2 SEM micrograph of $Gd_{1-x}Sr_xMnO_3$ [(a) $x=0.3$, (b) $x=0.4$ and (c) $x=0.5$]

3.3 D. C Conductivity and Magnetisation Studies of GSMO samples

3.3.1 D. C Conductivity studies

The low temperature dc conductivity measurements of the GSMO samples were carried out by using source measuring unit (Keithley 236) and by cooling the sample using CTI-CRYOGENICS Model 22C cryodyne cryocooler, in a temperature range of 20K – 300K. This system uses helium as the refrigerant and can be interfaced with many instruments that require cryogenic temperatures. The pressure maintained in the compressor is 400 PSIG/2758 kPa. The temperature was controlled using Lake Shore Model 321 auto tuning temperature controller, which has a stability of ± 0.1 K. The pressure inside the cryo cooler was maintained at 10^{-5} mB with the help of INDO VISION vacuum Pumping System Model VPS-100. The dc conductivity system is fully automated by using proprietary software called ICS.

The temperature variation of resistivity for the GSMO samples is depicted in figure 3.3. From the figure it is clear that all the three compositions show insulating nature in the measured temperature range. But careful observation reveals a slope change near 40 K, which is an indication of metal insulator transition. The behaviour is common to low band width manganites, and a very high magnetic field is needed to make a metal insulator transition [7]. The variation of resistivity with composition is in accordance with double exchange (DE) mechanism. According to DE mechanism the hopping amplitude is maximum when the value of Mn^{4+}/Mn^{3+} ratio is 0.5. The hopping amplitude is optimum for the doping $x = 1/3$. As amount of strontium doping increases, more Mn^{4+} ions are produced and hence the Mn^{4+}/Mn^{3+} ratio recedes away from the optimum 0.5 value and consequently resistivity value decreases.

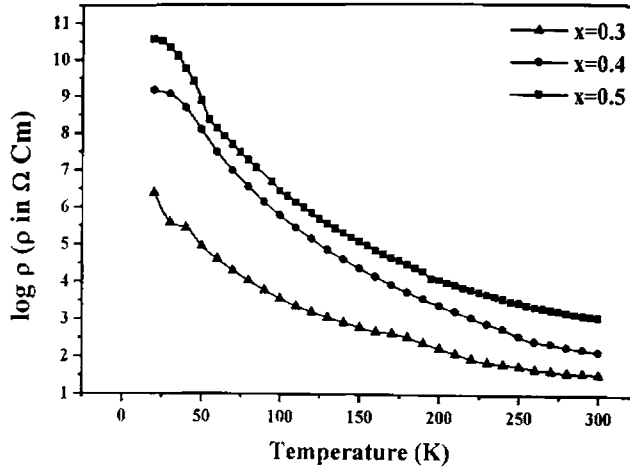


Figure 3.3 Temperature variation of resistivity with temperature of $Gd_{1-x}Sr_xMnO_3$ ($x=0.3$, $x=0.4$ and $x=0.5$)

The exact conduction mechanism in the paramagnetic phase of the GSMO samples can be ascertained by analyzing the resistivity data with equations of different conduction mechanisms. In paramagnetic insulating regime, mainly three types of mechanism have been found to be ruling the conduction process in these compounds. They are (1) thermal activation or band gap model, (2) variable range hopping model (VRH) and (3) small polaron hopping model (SPH). Band gap model is widely employed in most of the semiconductors and insulators [8 - 10]. There is an energy gap between conduction band and valence band. If the thermal energy is sufficient to overcome the band gap the electron becomes free to conduct. The expression for resistivity can be written in the following form

$$\rho = \rho_0 \exp(E_A / k_B T) \quad (3.1)$$

where T is the absolute temperature, ρ_0 is the value of resistivity at infinite temperature, E_A is the activation energy and k_B is the Boltzmann's constant. From equation (3.1) it is clear that the resistivity data should exhibit Arrhenius temperature dependence (i.e. straight line behaviour between $\log \rho$ and $1/T$). The variation of $\log \rho$ with reciprocal of temperature for the three GSMO samples in

the temperature range 50K – 300K (the resistivity data below 50K is avoided to make sure that the region is purely paramagnetic) is given in figure 3.4.

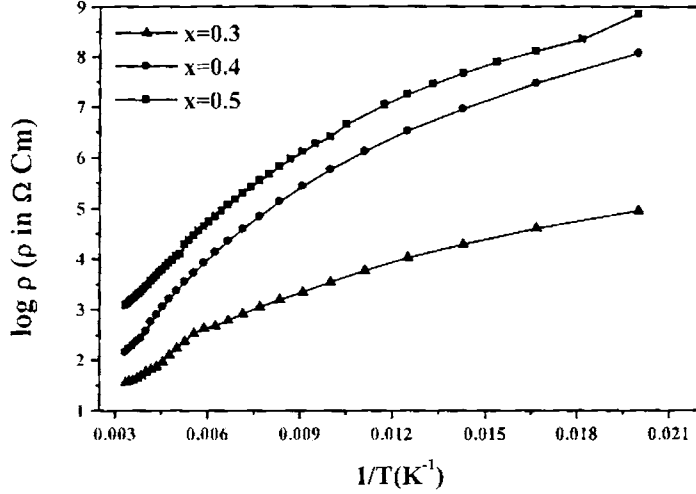


Figure 3.4 Temperature variation of resistivity with reciprocal temperature of $Gd_{1-x}Sr_xMnO_3$ ($x=0.3$, $x=0.4$ and $x=0.5$)

However from figure 3.4, it is clear that all the variations are non linear and hence we conclude that the band gap model is insufficient to explain the conduction process in these class of material. The second possibility is small polaron hopping model (SPH) [11-15]. In the case of small polarons (deeply trapped electrons), the thermal energy is not sufficient to overcome the deep potential well and to hop out of its site. Then the hopping is possible by a multiphonon assisted process [19]. That is, the electron is activated to an intermediate state first, which is still a localized state with higher energy. Then the thermal energy acquired from the second phonon is sufficient for hoping out from the intermediate state to its nearest neighbour. The expression for resistivity is

$$\rho = AT \exp(E_A/k_B T) \quad (3.2)$$

where T is absolute temperature and E_A is activation energy and A is a constant. The value of A is given by

$$A = \frac{k_B}{\nu_{ph} N e^2 R^2 c (1-c) \exp(2\alpha R)} \quad (3.3)$$

where N is the number of ion sites per unit volume, R average inter site spacing, c is the fraction of sites occupied by polaron, α is the electron wave function decay constant, ν_{ph} is optical phonon frequency and k_B is the Boltzmann's constant. Further, in order to check whether the conduction process obeys SPH a graph is plotted with $\log(\rho/T)$ on the Y-axis and $1/T$ on the X-axis (figure 3.5). The graph is linear at the high temperature side but there is deviation from linearity at the low temperature side. So it can be concluded that SPH model alone can not account for the conduction process.

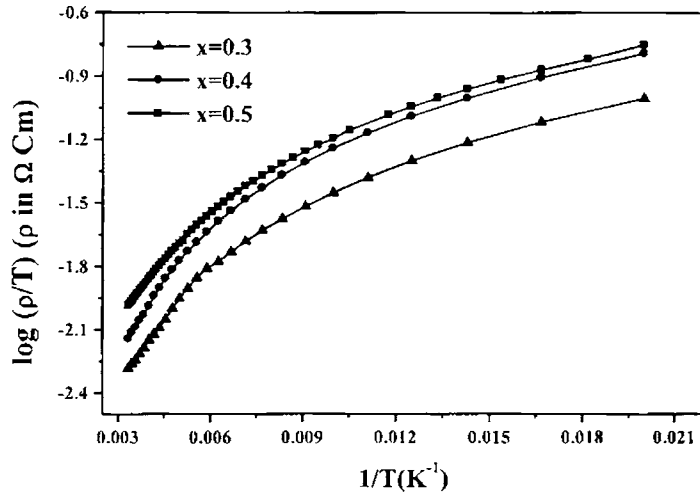
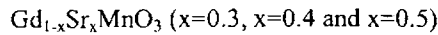


Figure 3.5 Temperature variation of $\log(\rho/T)$ with reciprocal temperature of



Now the next alternative is to check whether the VRH model can be applied to account for the observed conduction process. According to the variable range hopping (VRH) model [20-25] if the electron is not deeply trapped (that is a large polaron) it can hop from one site to another with phonon assistance. At low

temperature the thermal energy is not sufficient to allow electrons to hop to their nearest neighbours, but the possibility to hop further to find a site with a smaller potential difference exists. Since the hopping range is variable, it is called variable range hopping. In three dimensional VRH model, resistivity can be expressed as

$$\rho = \rho_0 \exp(T_0 / T)^{1/4} \quad (3.4)$$

Here the straight line behaviour is between $\log \rho$ and $T^{-1/4}$. The constant T_0 is given by

$$T_0 = \frac{18\alpha^3}{k_B N(E_F)} \quad (3.5)$$

where α is the electron wave function decay constant, $N(E_F)$ density of states at Fermi level and k_B is Boltzmann's constant. VRH theory was developed to explain electron transport in doped semiconductors. There is a competition between the potential difference and electron hopping distance [16, 17]. That is reflected in the expression for hopping rate to a site at a distance R , with higher energy ΔE than the origin.

$$\gamma = \gamma_0 \exp(-2\alpha R - \Delta E / k_B T) \quad (3.6)$$

For this VRH model the graph plotted between $\log \rho$ and $T^{-1/4}$ should be a straight line. From figure 3.6, it is clear that there is a linear behaviour in the temperature range 50K – 170K. Thus for a wide temperature range the conduction mechanism in the paramagnetic phase of the material obeys VRH. Above 170K the conduction is SPH assisted. This could be verified by plotting a graph between $\log (\rho/T)$ and $1/T$, above 170K [figure 3.7(a)] and $\log \rho$ vs $T^{-1/4}$ in the temperature range 40K – 170K [figure 3.7(b)]. From the figure it is clear that the two variations are straight lines. Sayani Bhattacharya et al. reported the same

behaviour for manganite $\text{La}_{1-x}\text{Ca}_x\text{Na}_y\text{MnO}_3$ [26] and Mollah et al. reported the same for manganite $\text{Pr}_{0.65}\text{Ca}_{0.35-x}\text{Sr}_x\text{MnO}_3$ [27].

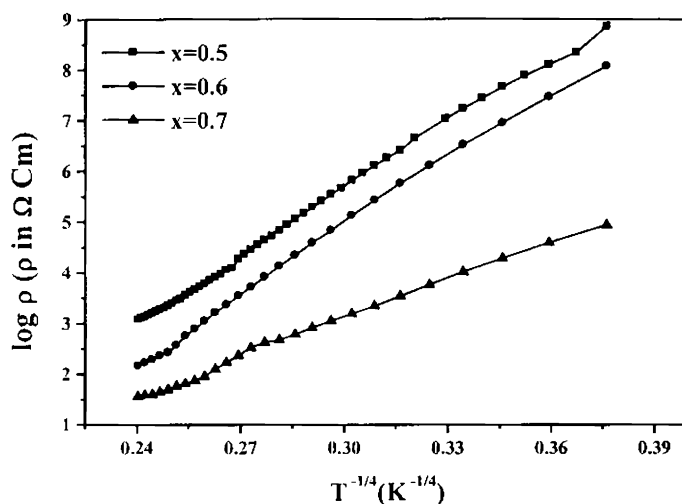


Figure 3.6 Variation of $\log(\rho)$ with $T^{-1/4}$ of $\text{Gd}_{1-x}\text{Sr}_x\text{MnO}_3$ ($x=0.3$, $x=0.4$ and $x=0.5$)

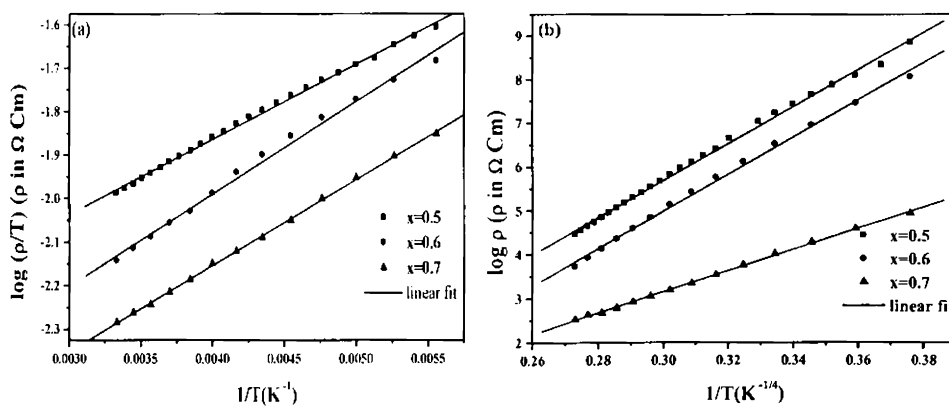


Figure 3.7 (a) Variation of $\log(\rho/T)$ with reciprocal temperature (b) Variation of $\log(\rho)$ with $T^{-1/4}$ of $\text{Gd}_{1-x}\text{Sr}_x\text{MnO}_3$ ($x=0.3$, $x=0.4$ and $x=0.5$)

3.3.2 Magnetisation studies

In order to understand the metal insulator transition in manganites in the scenario of double exchange mechanism the magnetisation studies of the samples are necessary. The magnetisation studies of the GSMO samples were carried out using vibration sample magnetometer (model EG & G Par 4500) in the temperature range 10K – 300K. The magnetisation curves FC and ZFC for $Gd_{0.5}Sr_{0.5}MnO_3$ at two different magnetic fields [(a) 50 Oe and (b) 200 Oe] are presented in figure 3.8.

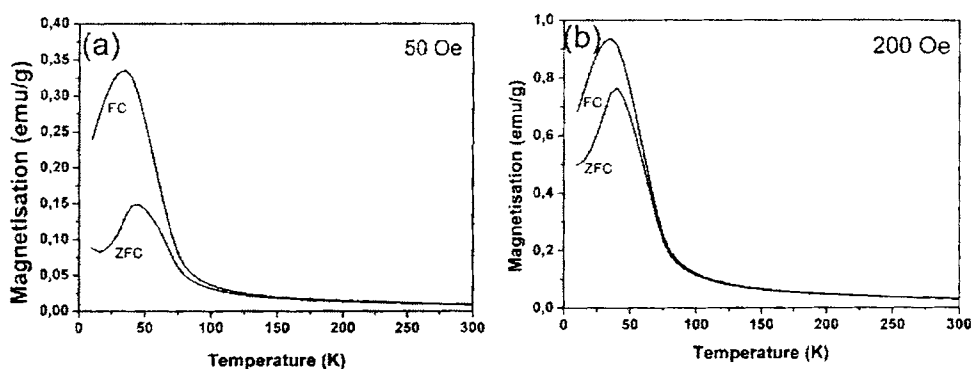


Figure 3.8 Temperature variations of magnetisation of $Gd_{0.5}Sr_{0.5}MnO_3$ at (a) 50 Oe
 $Gd_{0.5}Sr_{0.5}MnO_3$ at different temperatures (b) 200 Oe.

As temperature decreases from room temperature the magnetisation increases showing a transition from paramagnetic to ferromagnetic. But at very low temperatures the sample shows an irreversible thermomagnetisation process. Under a magnetic field of 50 Oe the splitting between ZFC and FC magnetisation is observed at 125 K and when the field is increased to 200 Oe, the splitting becomes narrower and the splitting temperature (T_{ir}) shifts to 70 K. This splitting is one of the characteristics of spin glass like behaviour and the shift in the splitting temperature with different magnetic fields is a consequence of the balance between the competing magnetic and thermal energies. These results suggest that this compound is in a spin glass like state at temperatures lower than

T_{irr} . This spin glass like behaviour was already reported in $Gd_{0.5}Sr_{0.5}MnO_3$ by Garcia-Landa *et al.* [7].

Figure 3.9 shows the field dependence of magnetisation up to 3 T of $Gd_{0.5}Sr_{0.5}MnO_3$ at different temperatures. It is found that at temperatures lower than T_{irr} (at 10 K and 40 K); the low field region of magnetisation becomes a nonlinear function of field and also displays hysteresis. This feature is also characteristic of a magnetic ordering and is consistent with that of the results of Terai *et al.* [28] in $Gd_{0.5}Sr_{0.5}MnO_3$. From temperature dependent magnetisation curves (figure 3.10) for the other two compositions ($Gd_{0.6}Sr_{0.4}MnO_3$ and $Gd_{0.7}Sr_{0.3}MnO_3$) it is evident that a paramagnetic to spin glass like transition occurs for $Gd_{1-x}Sr_xMnO_3$ ($x=0.3$, $x=0.4$ and $x=0.5$) at low temperatures. The magnetic transition at low temperature causes metal insulator transition via double exchange mechanism.

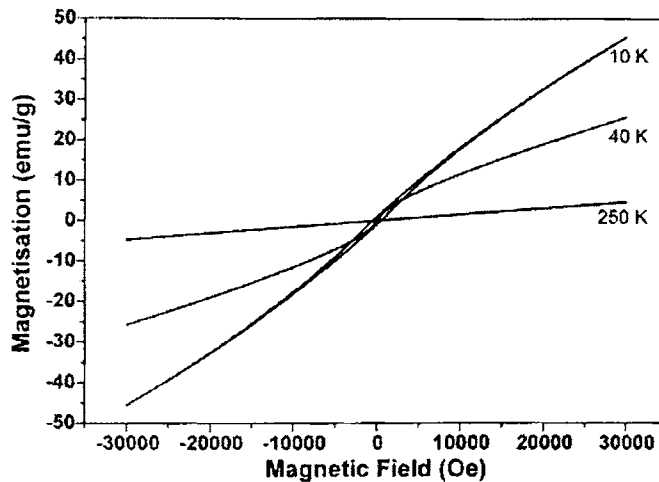


Figure 3.9 Hysteresis curves of $Gd_{0.5}Sr_{0.5}MnO_3$ at different temperatures

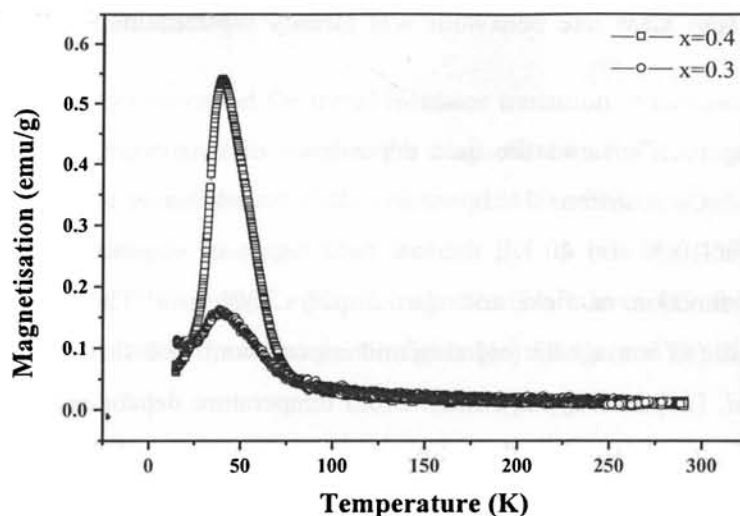


Figure 3.10 Temperature variation of magnetisation of $Gd_{1-x}Sr_xMnO_3$ ($x=0.3$ and $x=0.4$)

3.4 MR studies of GSMO

Magneto-resistance studies for the samples $Gd_{1-x}Sr_xMnO_3$ ($x=0.3$, $x=0.4$ and $x=0.5$) were done by taking resistivity measurements with a standard four probe technique, using Kiethley source meter and sensitive voltmeter. A detailed description of the MR experimental set up was given in chapter 2. The resistivity measurements were carried out in zero magnetic field and in applied fields of 1T, 5T and 8 T. The resistivity variations with applied field are shown in the figure 3.11. The external field causes a reduction of the resistivity in the entire temperature range for all the compositions indicating the colossal magnetoresistance (CMR) property of the manganite samples. The metal insulator (M-I) transition is obtained with the application of high magnetic field (8T) for the sample $Gd_{0.7}Sr_{0.3}MnO_3$. For the other two compositions the M-I transition could not be obtained even for 8T field. This is because of their increased resistivity at low temperatures ($>10^6 \Omega \text{ Cm}$) is out of the range of the measuring MR set up and therefore undergone cutoff at low temperatures. The comparative reduction in resistivity for the sample $Gd_{0.7}Sr_{0.3}MnO_3$ is due to the closeness of Mn^{4+}/Mn^{3+}

ratio to the optimum value for double exchange mechanism. Because of the reduced resistivity, a metal insulator transition (MIT) by the application of 8T field could be observed in the case of $Gd_{0.7}Sr_{0.3}MnO_3$. Thus charge ordered manganites show MIT only with the application of very high magnetic field.

MR of the GSMO samples was calculated using the equation (1.1). The MR measurements of all the GSMO samples had been undertaken in the temperature range 80K-300 K and the variation of MR with temperature is shown in the figure 3.12.

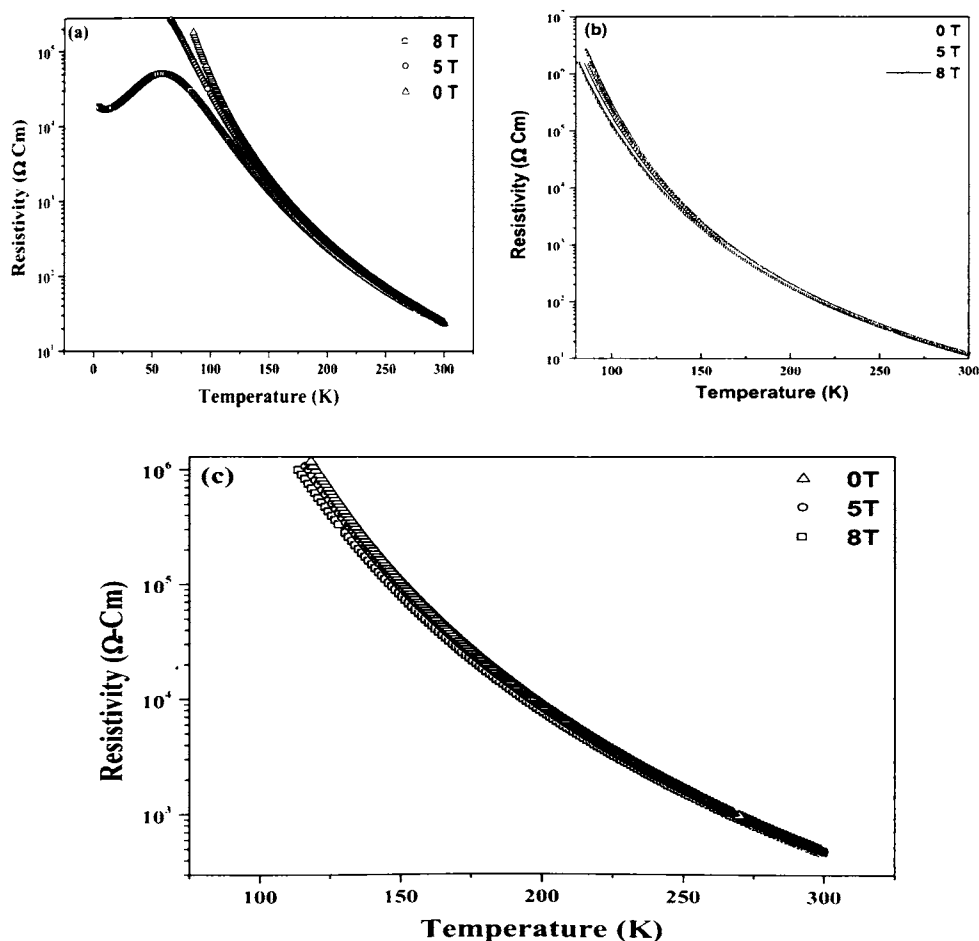


Figure 3.11 Temperature variation of resistivity with temperature under different applied magnetic fields for the sample $Gd_{1-x}Sr_xMnO_3$ [(a) $x=0.3$, (b) $x=0.4$ and (c) $x=0.5$]

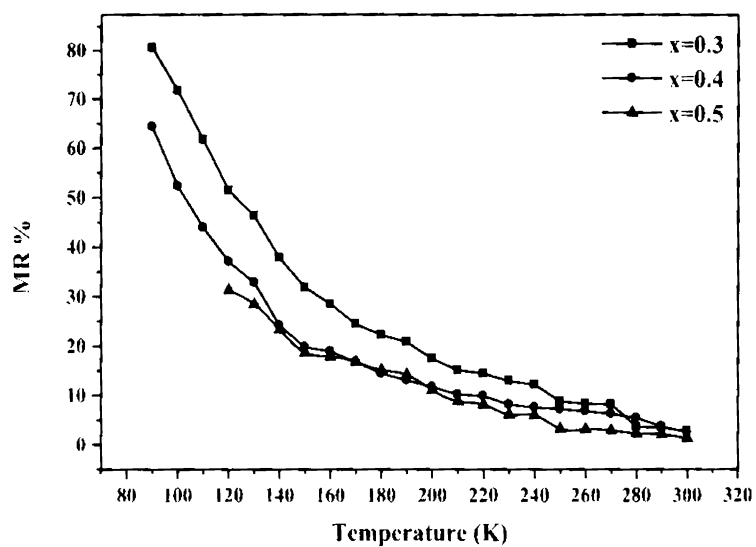


Figure 3.12 Variation of MR with temperature for the samples $Gd_{1-x}Sr_xMnO_3$ [$x=0.3$, $x=0.4$ and $x=0.5$]

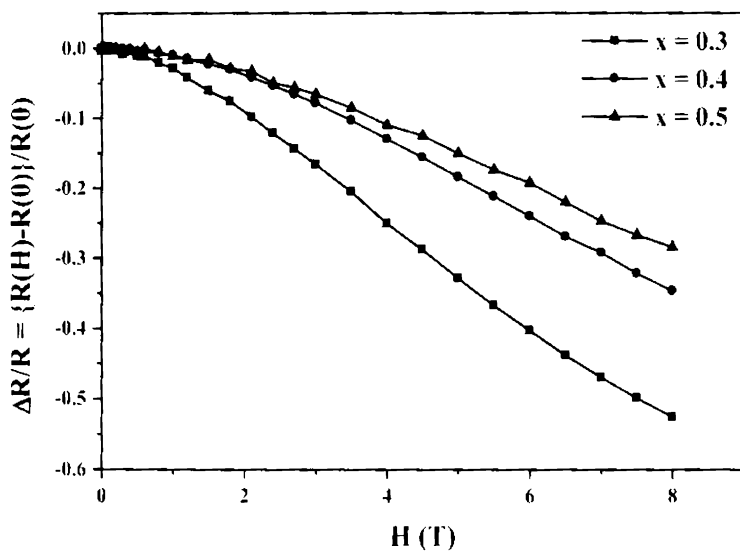


Figure 3.13 Variation of MR with applied magnetic field (zero to 8 T) for the samples $Gd_{1-x}Sr_xMnO_3$ [$x=0.3$, $x=0.4$ and $x=0.5$]

From the figure it is clear that all the samples show a linear increase of MR% with decrease in temperature. The observance of MR% peak near the transition temperature was prohibited by the limitation of the measuring device beyond $10^6 \Omega \text{ Cm}$. The figure 3.13 shows the variation of MR with applied magnetic field. With applied field the MR% increases for all the compositions, due to the large suppression of magnetic fluctuation caused by the high magnetic field. The MR% is more in the case of GSMO with $x=0.3$. This is due to the closeness of $\text{Mn}^{4+}/\text{Mn}^{3+}$ ratio to the optimum value for double exchange mechanism.

3.5 Conclusion

GSMO samples $\text{Gd}_{1-x}\text{Sr}_x\text{MnO}_3$ [$x=0.3$, $x=0.4$ and $x=0.5$] were prepared using wet solid state reaction method. The particles were found to have orthorhombically distorted perovskite structure. In the absence of magnetic field no metal insulator transition is exhibited by all the GSMO samples, which is a common feature in the case of low bandwidth manganites. But a slope change near 40 K is an indication of metal insulator transition associated with magnetic transition. The resistivity value increases with Sr doping. This can be explained by double exchange mechanism. The temperature variation of magnetisation indicates that there is a transition from paramagnetic state to magnetically ordered state like spin glass state near 40K. The coincidence of two transition temperatures near 40 K is an indication of hopping due to double exchange mechanism in low band width manganites. The conduction mechanism in the paramagnetic phase of the sample is variable range hopping (VRH) at low temperature followed by small polaron hopping (SPH) at high temperature. Magneto resistance studies reveal that the low bandwidth manganite exhibits colossal magnetoresistance property. The MR percentage increases with increase of applied field and decrease of temperature.

References

- [1] Pedersen L. A and Libby W. F, *Science* **176** (1972) 1355.
- [2] Venkatesan T, Rajeswari M, Dong Z. W, Ogale S. B, and Ramesh R, *Philos. Trans. roy. Soc. A* **356** (1998) 1661.
- [3] Coey J.M.D and Viret M, *Advances in Physics* **48** (1999) 167-293.
- [4] Goyal A, Rajeswari M, Shreekala R, Lofland R, Bhagat S. M, Boettcher T, Kwon C, Ramesh R and Venkatesan T, *Appl. Phys. Lett.* **71** (1997) 2535.
- [5] Pollert E, Krupicka S and Kuzmicova E, *J.Phys.Chem.Solid* **43** (1982) 1137.
- [6] Zhao G. M, Conder K, Keller H and Muller K. A, *Nature* **381** (1996) 676.
- [7] Garcia-Landa B, De Teresa J. M. D, Ibarra M. R, Ritter C, Drost R and Lees M. R, *J. Appl. Phys.* **83** (1998) 7664.
- [8] Kusters R. M, Singleton J, Keen D. A, Mc Greevy R and Hayes W, *Physica B* **155** (1989) 362.
- [9] Xiong G. C, Bhagat S. M, Dominguez M, Ju H. L, Greene R. L, Venkatesan T, Byers J. M and Rubinstein M, *Solid St. Commun.* **97** (1996) 599.
- [10] Hundley M.F, Hawley M, Heffner R. H, Jia Q. X, Neumeier J. J, Tesmer J, Thomson J. D and Wu X. D, *Appl. Phys. Lett.* **67** (1995) 860.
- [11] Holstein T, *Ann. of Phys.* **8** (1959)325.
- [12] Mollah S, Khan D. K, Arshad M, Ravi Kumar and Das A, *Journal of Physics and Chemistry of Solids* **69** (2008) 1023.
- [13] Chen X. J, Zhang C. L, Almasan C. C, Gardner J. S and Sarrao J. L, *Phys. Rev. B* **67** (2003) 094426.

- [14] Yeh N. -C, Fu C. -C, Wei J. Y. T, Vasquez R. P, Huynh J, Maurer S. M, Beach G and Beam D. A, *J. Appl. Phys.* **81** (1997) 5499.
- [15] Jakob G, Westerburg W, Martin F, Adrian H, *Phys. Rev. B* **58** (1988) 14966.
- [16] Mott N. F *Metal-Insulator Transitions*, 2nd edn. Taylor and Francis, London (1990).
- [17] Mott N. F and Davies E. A, *Electronic Processes in Noncrystalline Materials*, Clarendon Press, Oxford (1971).
- [18] Asamitsu A, Moritomo Y, Tomioka Y, Arima T, Tokura Y *Nature* **373** (1995) 407.
- [19] Young Sun, Xiaojun Xu and Yuheng Zhang, *J.Phys.Condens. Matter* **12** (2000)10475.
- [20] Viret M, Ranno L, Coey J. M. D, *Phys. Rev. B* **55** (1997) 8067.
- [21] Ewe L. S, Hamadneh I, Salama H, Hamid N. A, Halim S. A and Abd-Shukor R, *Applied Physics A: Material Science and Processing* **95** (2008) 457.
- [22] DeTeresa J. M, Ibarra M. R, Blasco J, Garcia J, Marquina C, Algrabel P, Arnold Z, Kamenev K, Ritter C and von Helmholt R, *Phys. Rev. B* **54** (1996)1187.
- [23] Keshri S and Dayal V, *Pramana* **70** (2008) 697.
- [24] de Teresa J. M, Ibarra M. R, Algrabel P. A, Ritter C, Marquina C, Blasco J, Garcia J, del Moral A and Arnold Z, *Nature* **386** (1997) 256.
- [25] Jaime M, Salamon M. B, Pettit K, Rubinstein M, Treece R. E, Horowitz J. S and Chrisey. B, *Appl. Phys. Lett.* **68** (1996) 1576.
- [26] Sayani Bhattacharya, Aritra Banerjee, Pal S, Chatterjee P, Mukherjee R. K and Chaudhuri B. K, *J.Phys.Condens. Matter* **14** (2002)10221.

- [27] Mollah S, Huang H. L, Yang H. D, Sudipta Pal, Taran S and Chaudhuri B. K,
J. Magn.Magn.Mater. **284** (2004) 383.
- [28] Terai T, Sasaki T, Kakeshita T, Fukuda T, and Saburi T, *Phys. Rev. B* **61**
(2000) 3488.

Chapter 4

Studies on the Magnetoelectric Transport Properties of Sodium Doped Lanthanum Manganites

4.1 Introduction

Manganites are technologically important materials because of their colossal magneto-resistance property [1]. High value of magneto resistance produced by applying small magnetic field in or near room temperature makes them valuable in applications. From a fundamental point of view the interplay of various factors that influence the electrical transport properties assume significance. A variety of parameters like charge ordering, orbital coupling, magnetic ordering and lattice degrees of freedom have profound influence on the electrical and magnetic properties of these materials [2, 3].

The large colossal magnetoresistance (CMR) was first reported in hole-doped manganese oxide perovskites. Other compounds such as double perovskites, manganese oxide pyrochlores and europium hexaborides, among others, also exhibit the same striking property of manganites. In these compounds, a Mn^{3+}/Mn^{4+} double exchange interaction reduces the transfer energy of the Mn 3d holes through a ferromagnetic alignment of neighbouring Mn spins resulting in a CMR near the Curie temperature (T_c). However, further investigations revealed that the double exchange alone cannot quantitatively account for the observed CMR effect, and the strong electron-phonon interaction arising out of Jahn-Teller splitting may also have to be taken into account [2, 3]. The strong Jahn-Teller effect due to Mn^{3+} leads to the formation of polarons. This strongly influences the transport properties. Other parameters that influence the magneto-resistance properties of manganites are chemical composition, radius of A site cation, amount of hole doping (x) and random disorder of the A site. The magnetic

phases and electronic properties of these manganites vary with the doping level (x). Upon increasing x , the concentration of Mn^{4+} increases, giving rise to a mixture of Mn^{3+} and Mn^{4+} which forms ferromagnetism for doping levels lying in the range 0.2 to 0.4, as a result of double-exchange interaction between Mn^{3+} and Mn^{4+} ions [1].

Usually alkaline earth metals are doped in manganites to obtain mixed valency in those compounds which is a necessary condition for hopping by double exchange mechanism. The optimum value of Mn^{4+}/Mn^{3+} ratio for double exchange mechanism is 0.5, which can be obtained by doping of alkaline earth metal by 1/3. But low doping of alkali metal can produce optimum value of Mn^{4+}/Mn^{3+} ratio due to difference in oxidation state. Each alkali metal ion can produce Mn^{5+} ion and an electron from Mn^{3+} goes to Mn^{5+} , change it into Mn^{4+} and itself changes to Mn^{4+} ion. Thus alkali metal doping (x) can produce $2x$ number of Mn^{4+} and reduce x number of Mn^{3+} and the optimum value can be obtained by amount of doping $x=1/6$. Among alkali metals sodium has similar ionic radius of lanthanum and hence Na doping will produce only little lattice distortion. The charge ordering has a prominent role in the magneto-resistance property of manganites. For alkaline earth metals, composition $x=0.5$ produces charge ordering. But in the case of alkali metal only $x=0.25$ doping can produce charge ordered state. From the magneto resistance point of view, the doping values $x<0.25$ are important. The dc conductivity and magnetisation studies of the manganites can reveal the exact mechanism behind the transport properties in the ferromagnetic and paramagnetic phases. This chapter deals with the evaluation of dc conductivity, magnetisation and magneto-resistance properties of intermediate bandwidth sodium doped lanthanum manganite.

4.2 Sample preparation and structural characterization of LNMO samples

$La_{1-x}Na_xMnO_3$ ($x = 0.05, 0.1, 0.15, 0.2$ and 0.25) samples were prepared using citrate gel method. Stoichiometric mixtures of La_2O_3 , Na_2CO_3 and

$\text{Mn}(\text{NO}_3)_2$ were dissolved in dilute nitric acid and suitable amounts of ethylene glycol and citric acid were added. Then the mixture was slowly heated for several hours until a gel was formed. It was heated at 80°C and the resulting black powder was pressed into pellets and sintered at 1100°C for 12 hours [4]. X-ray powder diffraction was carried out using Cu K_α radiation. The XRD pattern of all compositions of LNMO sample is shown in figure 4.1(a). Indexed XRD pattern of $\text{La}_{0.75}\text{Na}_{0.25}\text{MnO}_3$ is depicted in figure 4.1(b).

The X-ray powder diffraction pattern (figure 4.1) shows that the sample is homogeneous and single phasic with rhombohedrally distorted perovskite structure [5]. From atomic absorption spectroscopy (AAS) and Energy Dispersive Spectroscopy (EDS), the stoichiometry of the elements in the sample was evaluated and those values are in good agreement with theoretical values. For different compositions of the LNMO, the particle size estimated by employing Debye – Scherrer equation is lying in the range 20 nm - 40 nm. The transmission electron micrographs (TEM) of the samples ($x = 0.15$ and 0.25) are shown in figures 4.2 and 4.4 respectively. Using TEM image of the sample $\text{La}_{0.75}\text{Na}_{0.25}\text{MnO}_3$, sizes of the particles were manually determined. Particles larger than the size of 50 nm are virtually absent and most of the particles are lying in the range of 10 nm to 30 nm. The particle size distribution of $\text{La}_{0.75}\text{Na}_{0.25}\text{MnO}_3$ is depicted figure 4.5. The average particle size was determined by using a Gaussian fit to the distribution histogram and was found to be 24 nm. This value is in good agreement with the size determined from the XRD analysis. The Selected Area Electron Diffraction (SAED) pattern of the particles of $\text{La}_{0.85}\text{Na}_{0.15}\text{MnO}_3$ shows well formed uniform circular rings (figure 4.3) which indicates the nano crystalline nature of the compound with perovskite structure. The SAED planes were identified and it indicates formation of crystal structure in agreement with those obtained from XRD pattern. The scanning electron microscopy studies were carried out using a Field emission scanning electron microscope (FESEM) JSM 6335 FESEM at 50 kV. The SEM micrographs for the other three compositions

($x=0.95, 0.9$ and 0.8) are shown as figures 4.6(a) to 4.6(c). From the micrographs it is clear that the particles are in the nano regime, even though the sizes of the particles are slightly larger than the TEM picture for the other two compositions, with near perfect spherical shape.

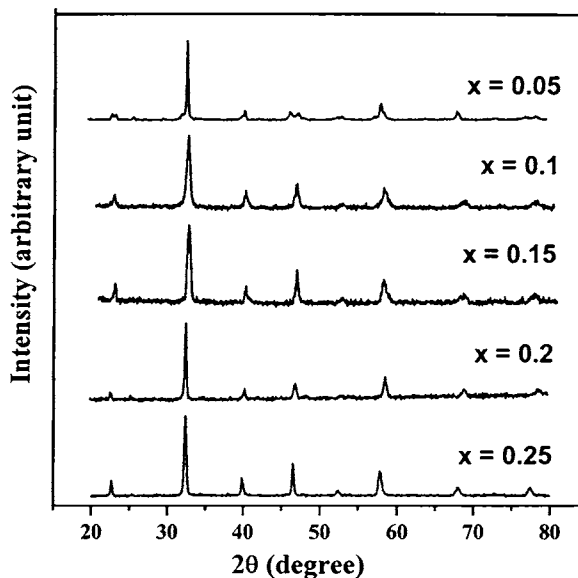


Figure 4.1 (a) X-ray diffraction pattern of $\text{La}_{1-x}\text{Na}_x\text{MnO}_3$

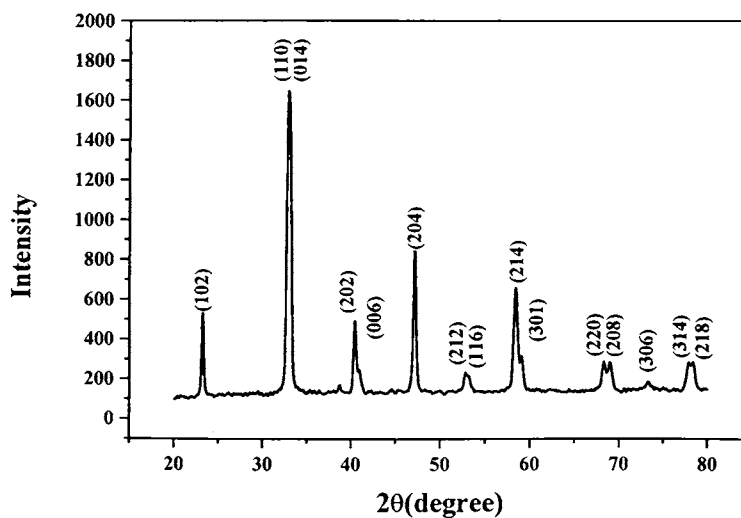


Figure 4.1 (b) XRD pattern of $\text{La}_{0.75}\text{Na}_{0.25}\text{MnO}_3$

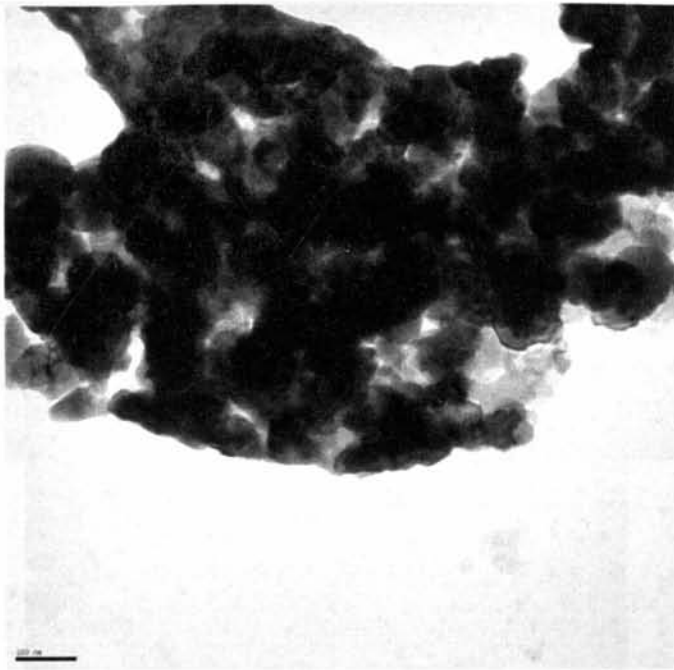


Figure 4.2 Transmission Electron Micrograph of $\text{La}_{0.85}\text{Na}_{0.15}\text{MnO}_3$

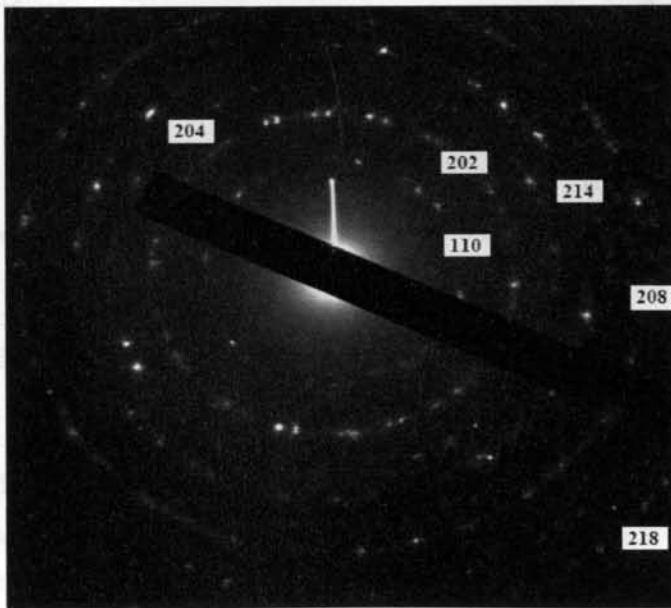


Figure 4.3 SAED pattern of sample $\text{La}_{0.85}\text{Na}_{0.15}\text{MnO}_3$.

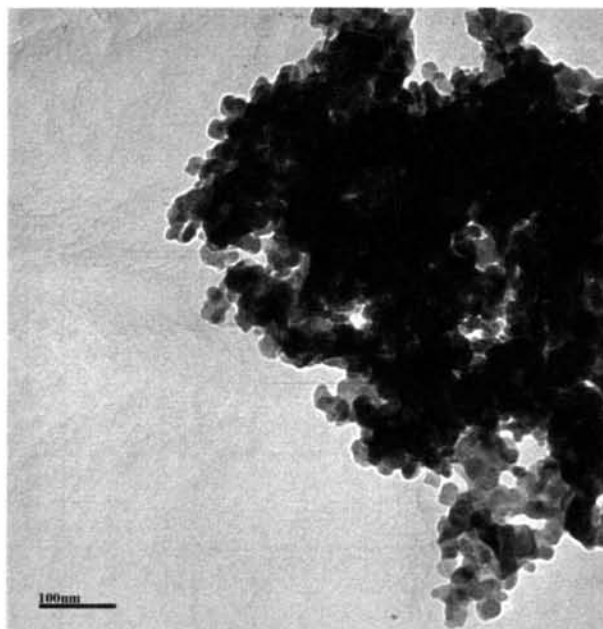


Figure 4.4 Transmission Electron Micrograph of $\text{La}_{0.75}\text{Na}_{0.25}\text{MnO}_3$

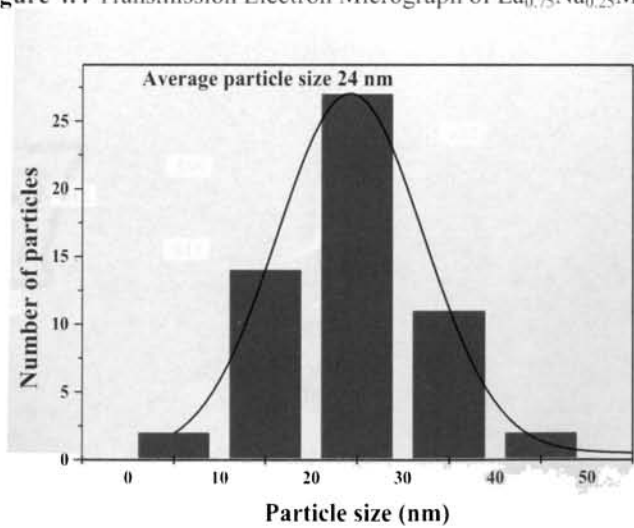


Figure 4.5 Particle size distribution of $\text{La}_{0.75}\text{Na}_{0.25}\text{MnO}_3$

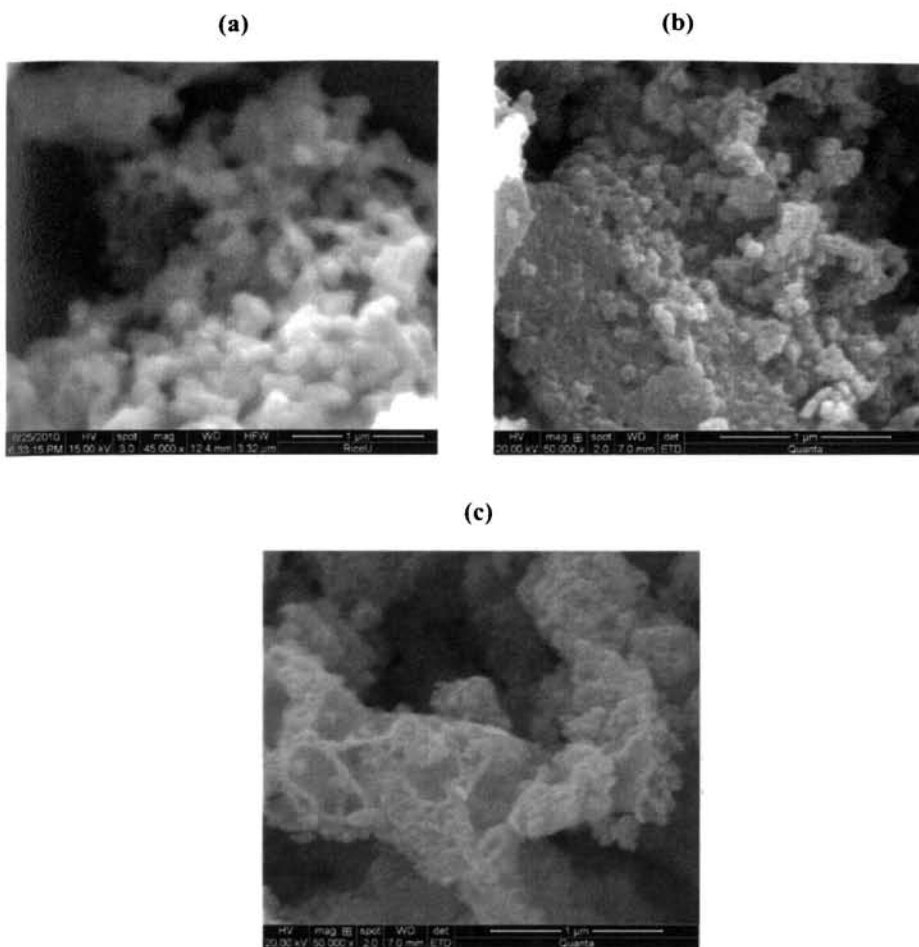


Figure 4.6 SEM images of $\text{La}_{1-x}\text{Na}_x\text{MnO}_3$ [(a) $x=0.05$, (b) $x=0.1$ and (c) $x=0.2$]

4.3 D. C Conductivity and Magnetisation Studies of LNMO sample

4.3.1 D. C Conductivity studies

D. C Conductivity studies of LNMO sample were carried out using standard four probe technique. A detailed description of resistivity measurement set up was given in chapter 2. The figure 4.7 shows a plot of the temperature dependence of the resistivity of the $\text{La}_{1-x}\text{Na}_x\text{MnO}_3$ samples ($x=0.05, 0.1, 0.15, 0.2$ and 0.25) taken in zero magnetic field. The resistivity curves were obtained by slowly increasing

the temperature from 1.5 K to 300 K. For composition $x = 0.05$, around 206 K the sample exhibits a transition from a metallic-like state (where the resistivity shows a positive temperature coefficient) to an insulator-like state (where the resistivity decreases with temperature). The resistivity shows a maximum at that transition temperature (T_{M-I}). The metal insulator transition temperatures were found to be 260 K, 300 K, 280 K and 70 K for the other compositions corresponding to $x = 0.1$, $x = 0.15$, $x = 0.2$ and $x = 0.25$ respectively. The metal insulator transition can be understood by considering the double exchange interaction in manganites, which is favored by the ferromagnetic to paramagnetic transition (which is explained in detail in the section 4.3.2). After an initial increase, the values of T_{M-I} decreases with increasing doping concentration. The observed initial increase can be explained by considering the fact that for every addition of Na^- ions, double the number of Mn^{4+} gets created and contributed to the hopping process. Thus even for a small amount of Na dopant concentration, enough number of holes are created in the e_g band and will contribute to conductivity thereby increasing T_{M-I} . T_{M-I} is maximum for the composition $x=0.15$ which can be attributed to the closeness of $\text{Mn}^{4+}/\text{Mn}^{3+}$ ratio (0.428) to the optimum value, 0.5 as in the case of $\text{La}_{2-x}\text{Ca}_x\text{MnO}_3$. Beyond the composition $x=0.15$ the increased $\text{Mn}^{4+}/\text{Mn}^{3+}$ ratio weakens double exchange mechanism and enhances super exchange, resulting into the decrease of T_{M-I} values. The very low value of T_{M-I} for the composition $x = 0.25$ is due to the charge ordering mechanism [6]. For this composition, $\text{Mn}^{4+}/\text{Mn}^{3+}$ ratio is 1 and hence forms a charge ordered state which causes a broad metal insulator transition near 70 K.

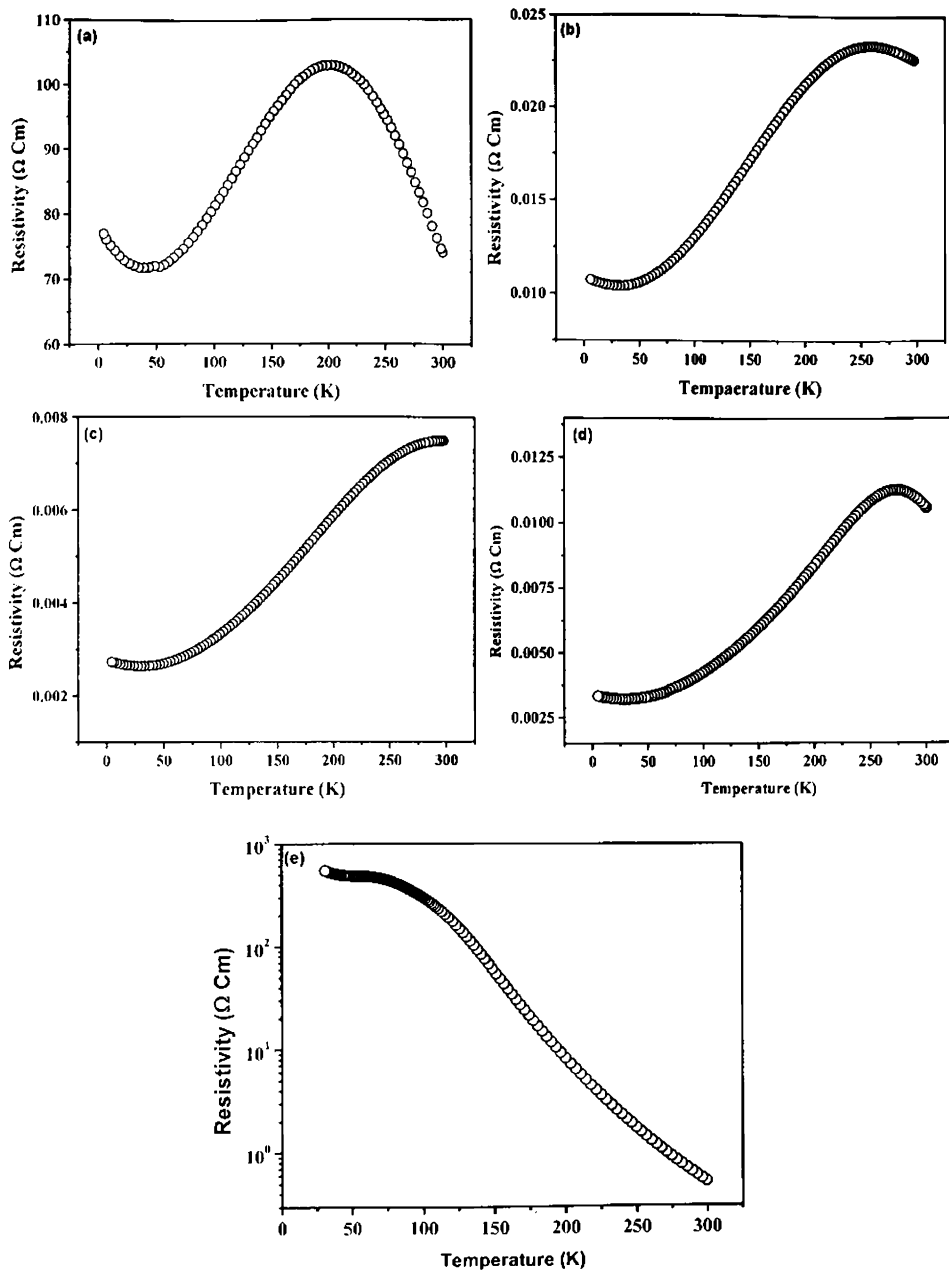


Figure 4.7 Variation of resistivity with temperature at for the samples $\text{La}_{1-x}\text{Na}_x\text{MnO}_3$ [(a) $x=0.05$, (b) $x=0.1$, (c) $x=0.15$, (d) $x=0.2$ and (e) $x=0.25$]

4.3.2 Magnetisation studies

The magnetisation studies of LNMO sample were carried out using vibration sample magnetometer (model EG & G Par 4500), in the temperature range 300K – 400K for compositions $x=0.05$ to $x=0.2$ and 20K to 300K for charge ordered composition $x=0.25$. The temperature variations of magnetisation for the LNMO samples are shown in figure 4.8.

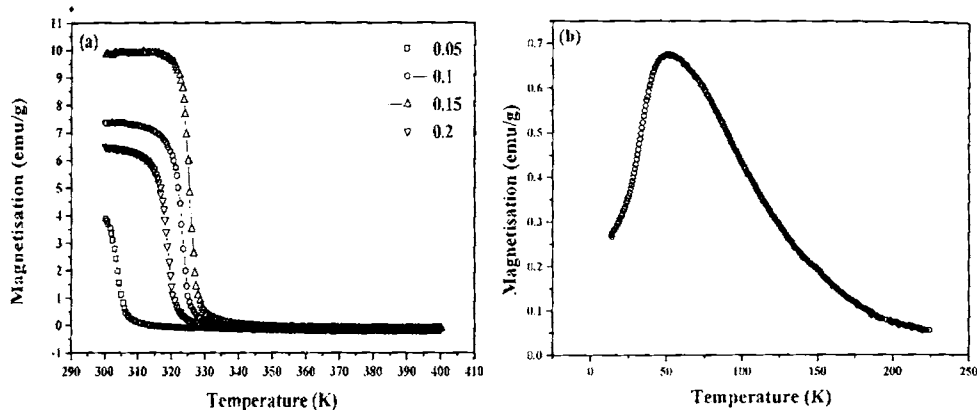


Figure 4.8 Temperature Variation of magnetisation for the samples (a) $\text{La}_{1-x}\text{Na}_x\text{MnO}_3$ [(a) $x=0.05, 0.1, 0.15,$ and 0.2] and (b) $x=0.25$

From the figure 4.8, it is clear that all the samples except $x=0.25$ show a paramagnetic to ferromagnetic transition with decrease of temperature. For the charge ordered composition $x = 0.25$, there is a transition from paramagnetic state to spin glass like state or near 60K. The variations of the Curie temperature (T_C) and metal insulator transition temperature (T_{M-I}) with composition are shown in figure 4.9. As doping of Na increases from 0.05, both T_C and T_{M-I} increase, attain maxima at composition $x = 0.15$ and then decrease. From the observed similarity in the variation of T_C and T_{M-I} with composition, we can conclude that double exchange is the mechanism responsible for the observed variation of T_C with Na doping. Each Na doping produces two Mn^{4+} ions and hence as Na doping increases, the $\text{Mn}^{4+}/\text{Mn}^{3+}$ ratio increases which favours ferromagnetism and double exchange interaction. The optimum value of the ratio for maximum double exchange interaction is very near to $x = 0.15$ and hence T_C and T_{M-I} attain

maximum value at Na doping $x = 0.15$. As doping level increased beyond that value the resulting Mn^{4+}/Mn^{3+} ratio favors super exchange interaction and as a result T_C and T_{M-I} get decreased. From figure 4.8 it is seen that the two critical temperatures (T_C and T_{M-I}) do not coincide. T_C is found to be greater than T_{M-I} and the difference is due to the grain size effect [7, 8]. Within the grains there are ferromagnetic clusters (consisting of both Mn^{4+} and Mn^{3+}) with Mn^{3+} regions in between the grains. In the Mn^{3+} region the interaction is antiferromagnetic super exchange. Thus the total resistivity is due to the sum of contributions from ferromagnetic clusters and the antiferromagnetic regions. As grain size get decreased the former contribution become less predominant and hence metal insulator transition takes place at a lower temperature compared to T_C .

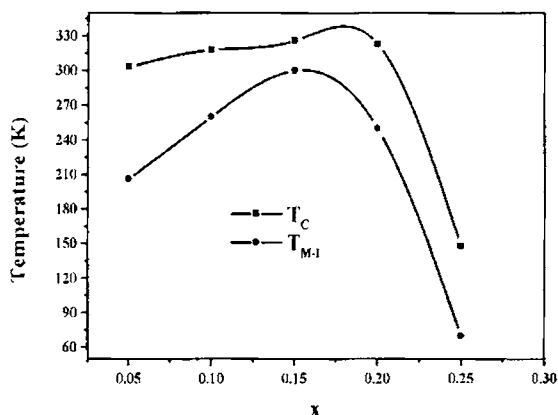


Figure 4.9 Variation of T_C and T_{M-I} with Na doping

4.3.3 Conduction mechanism in paramagnetic region

In the paramagnetic regime mainly three types of mechanism have been found to be ruling the conduction process in manganites. They are thermal activation or band gap model, variable range hopping model (VRH) and small polaron hopping model (SPH). In order to find which mechanism is responsible for the conduction in the paramagnetic phase of the manganites, different graphs using the different equations are to be plotted, above the metal insulator transition temperature. Band gap model is widely employed in most of the semiconductors

and insulators. If the thermal energy is sufficient to overcome the energy gap (band gap) the electron becomes free to conduct. For the band gap model [9-11], the equation for resistivity is given by

$$\rho = \rho_0 \exp(E_A/k_B T) \quad (4.1)$$

where T is the absolute temperature, ρ_0 is the value of resistivity at infinite temperature, E_A is the activation energy and k_B is the Boltzmann's constant.

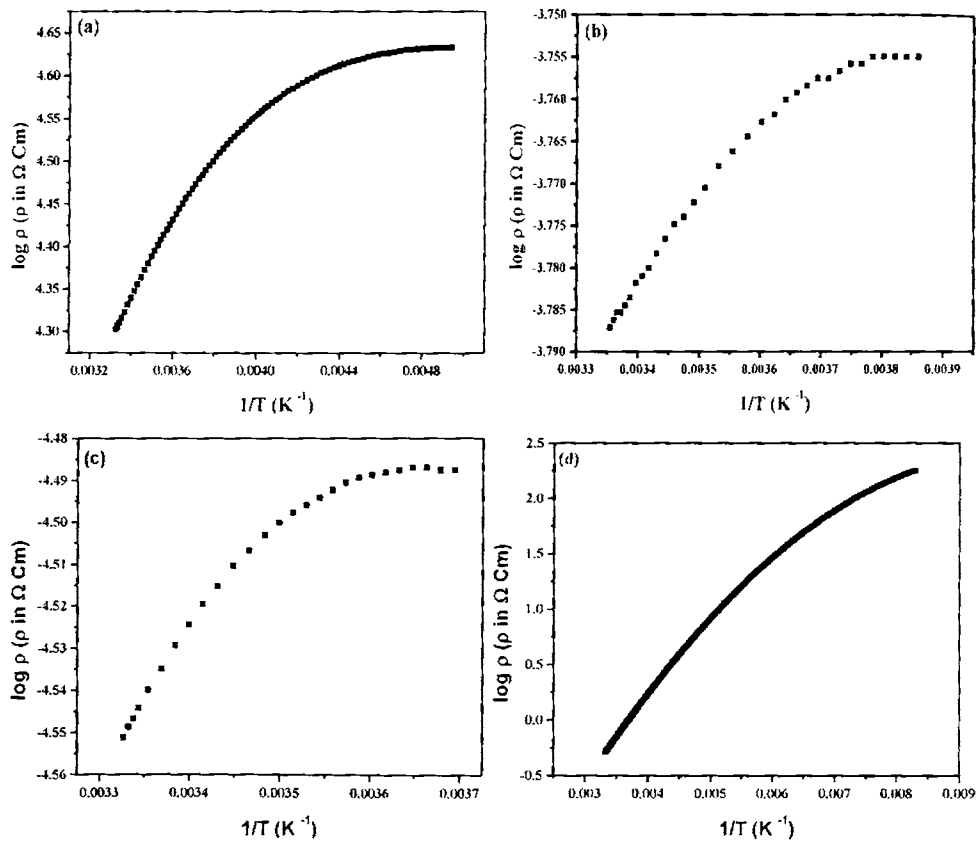


Figure 4.10 Variation of log ρ with reciprocal of temperature for the samples

$\text{La}_{1-x}\text{Na}_x\text{MnO}_3$ [(a) $x=0.05$, (b) $x=0.1$, (c) $x=0.2$ and (d) $x=0.25$]

The logarithmic variations of resistivity with reciprocal of temperature for all the LNMO samples are shown in the figure 4.10. From the figure it is clear that the linear relation exists only for the high temperature region and hence we can exclude the band gap model.

Then we can consider the nearest neighbour small polaron hopping (SPH) mechanism [12-16]. In the case of small polarons (deeply trapped electrons), the thermal energy is not sufficient to overcome the deep potential well and to hop out of its site. Then multi phonon assisted hopping is the only possibility [17]. According to SPH model, the expression for resistivity is

$$\rho = AT \exp(E_A / k_B T) \quad (4.2)$$

where T is absolute temperature and E_A is activation energy and A is a constant. Hence in the case of material obeying SPH model, the graph between (ρ/T) and $1/T$ should be a straight line.

The variation of reciprocal of temperature with of $\log(\rho/T)$ for all the LNMO (except $x = 0.15$, which shows metal insulator transition near room temperature) samples is depicted in the figure 4.11. For the compositions ($x = 0.05, 0.1$ and 0.2), the graphs are straight lines and for the composition $x = 0.25$, there is deviation from the straight line behaviour, especially at the low temperature region. So it can be concluded that SPH model alone can account for the conduction process in the case of Na doped manganites except for the composition $x=0.25$, which is a charge ordered state.

Now we have to check whether the VRH model can be applied to account for the observed conduction process. According to the variable range hopping (VRH) model [18-25] if the electron is not deeply trapped, it can hop from one site to another with phonon assistance. At low temperature the thermal energy is not enough to allow electrons to hop to their nearest neighbours, but is possible to hop

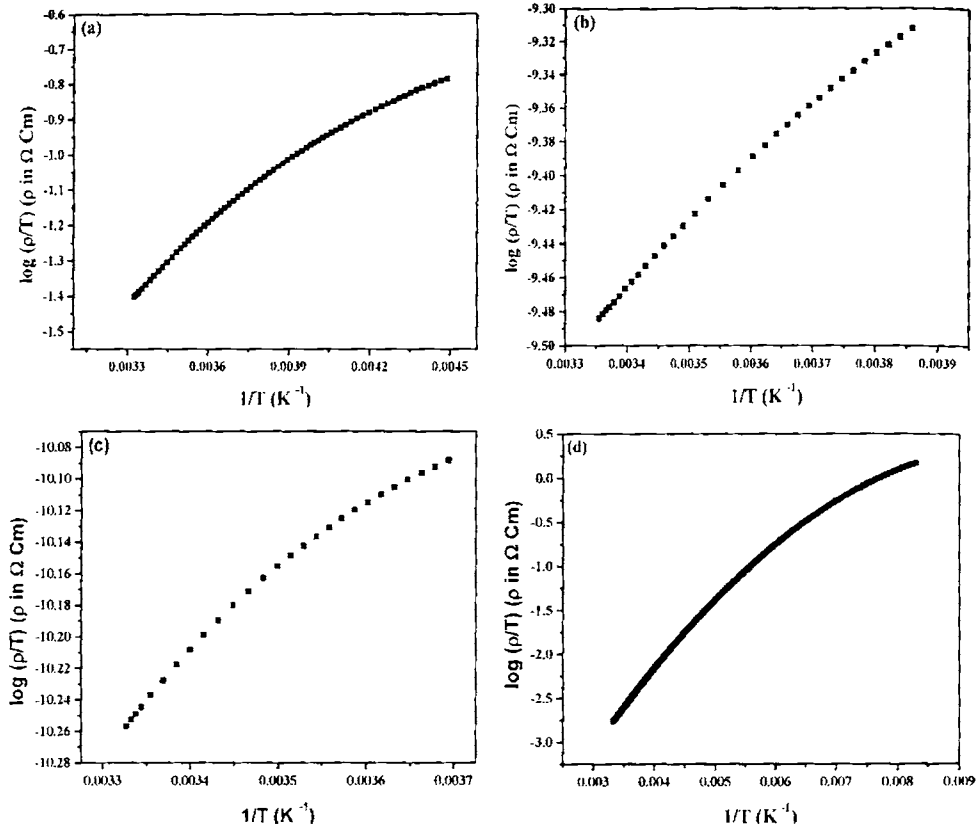


Figure 4.11 Variation of $\log(\rho/T)$ with reciprocal of temperature for the samples

$\text{La}_{1-x}\text{Na}_x\text{MnO}_3$ [(a) $x=0.05$, (b) $x=0.1$, (c) $x=0.2$ and (d) $x=0.25$]

further to find a site with a smaller potential difference. Since the hopping range is variable, it is called variable range hopping. According to VRH model the resistivity is given by

$$\rho = \rho_0 \exp(T_0/T)^{1/4} \quad (4.3)$$

where T_0 is a constant. The figure 4.12 depicts the $T^{-1/4}$ variation of logarithmic resistivity for all the LNMO samples in the insulating region. From the figure we can see that linear behaviour is exhibited by the composition $x \approx 0.25$, which is the

charge ordered state. Thus the conclusion is that in the charge ordered state the resistivity data follows the variable range hopping conduction. This is in agreement with earlier reports [26-29].

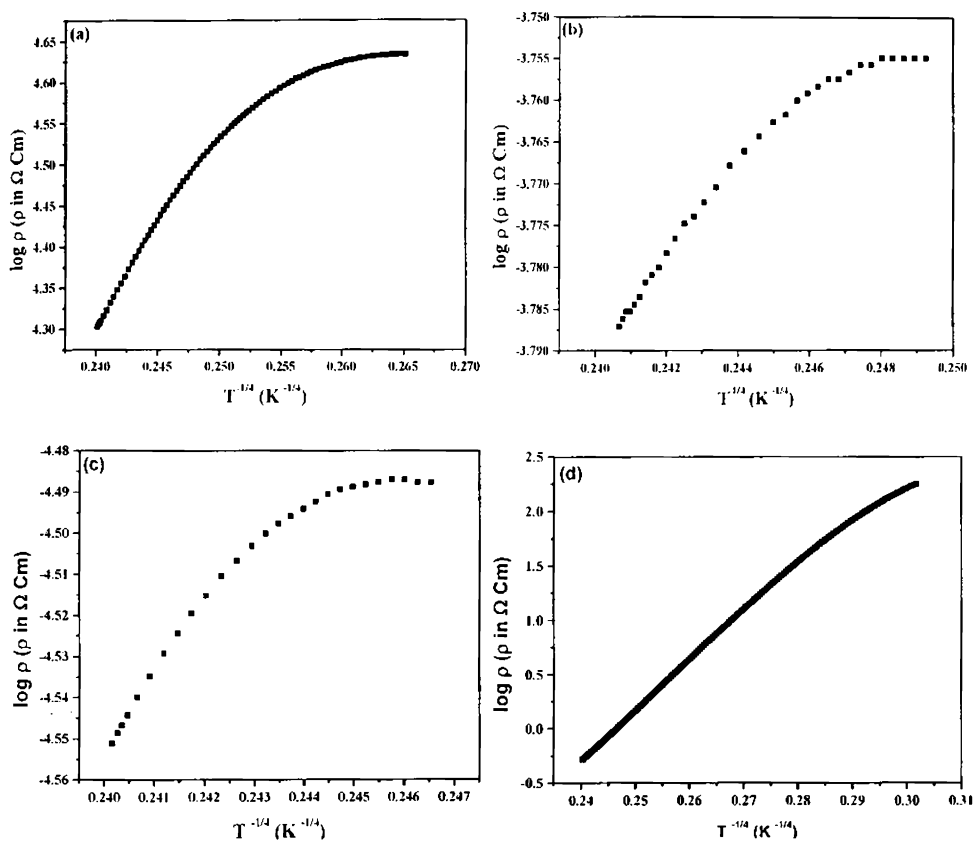


Figure 4.12 Variation of $\log \rho$ with $T^{-1/4}$ for the samples $\text{La}_{1-x}\text{Na}_x\text{MnO}_3$ [(a) $x=0.05$, (b) $x=0.1$, (c) $x=0.2$ and (d) $x=0.25$]

4.3.4 Conduction mechanism in ferromagnetic region

In general the low temperature resistivity data of manganite samples were analyzed using a polynomial expansion in temperature T as given in equation (4.4).

$$\rho = \rho_0 + \rho_2 T^2 + \rho_{4.5} T^{4.5} \quad (4.4)$$

Since resistivity is essentially constant for temperatures less than 10K for all samples, the resistivity data both with and without an applied field require a temperature independent resistivity term (ρ_0). This temperature independent term in the resistivity can be ascribed to scattering processes such as impurity, defect, grain boundary and domain wall scattering. This limiting resistivity is largely independent of A-site atoms. The second term ($\rho_2 T^2$) is due to electron- electron scattering and the last term ($\rho_{4.5} T^{4.5}$) is due to the electron – magnon scattering in the double exchange theory [30]. But we could not perfectly fit the resistivity data in the ferromagnetic region with the equation (4.4) in the case of the LNMO samples ($x=0.05, 0.1, 0.15$ and 0.2). Kalyana Lakshmi et al. introduced a $T^{1/2}$ term in the resistivity equation in the ferromagnetic phase of Na doped manganite and successfully obtained a perfect fitting [6]. By introducing a $T^{1/2}$ term in equation (4.4) the resistivity data exhibit a perfect fit with the equation. The equation is

$$\rho = \rho_0 + \rho_{1/2} T^{1/2} + \rho_2 T^2 + \rho_{4.5} T^{4.5} \quad (4.5)$$

Figure 4.13 represents the resistivity data fitting in the case of LNMO sample. The fitting parameters are given in the table 1. The additional term ($\rho_{1/2} T^{1/2}$) is due to the weak localization effect as a result of interference of complementary waves and enhanced electron – electron interaction [31, 32]. The fitting parameters decreases with increase in Na concentration except for the composition $x = 0.2$. The decrease of fitting parameters is in accordance with the variation of resistivity with composition.

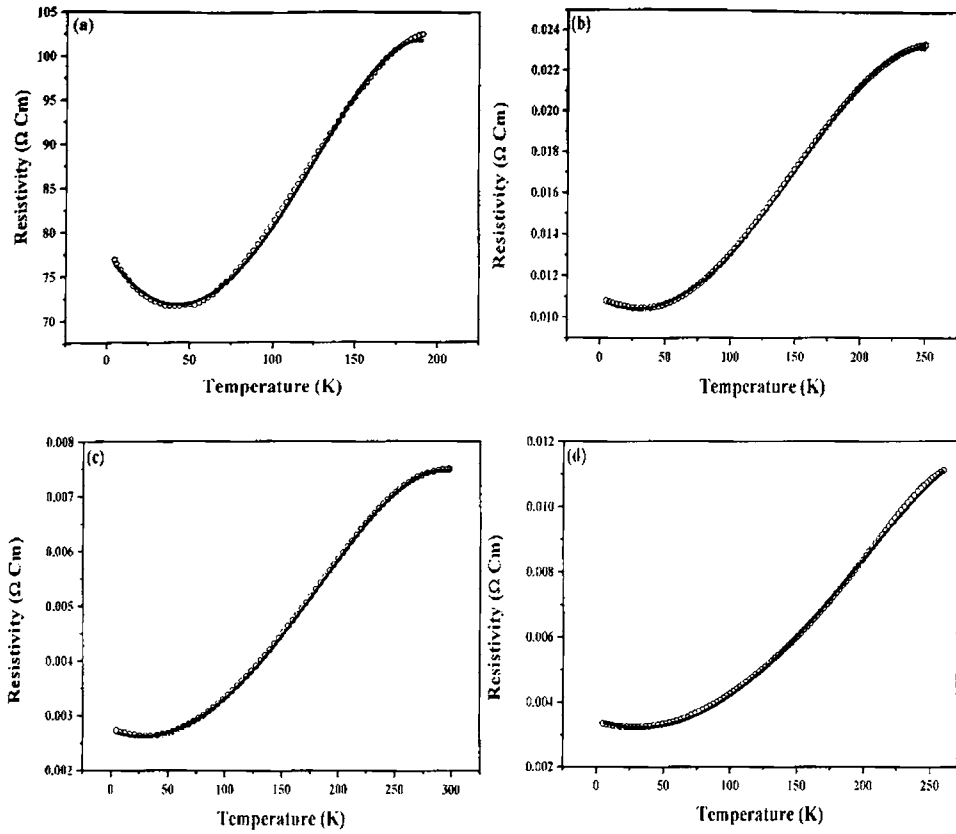


Figure 4.13 Variation of resistivity with temperature in the ferromagnetic region for the samples $\text{La}_{1-x}\text{Na}_x\text{MnO}_3$ [(a) $x=0.05$, (b) $x=0.1$, (c) $x=0.15$ and (d) $x=0.2$]. The solid line represents the fitting with equation (8)

x	ρ_0 ($\Omega \text{ Cm}$)	$\rho_{0.5}$ ($\Omega \text{ CmK}^{-1/2}$)	ρ_2 ($\Omega \text{ CmK}^{-2}$)	$\rho_{4.5}$ ($\Omega \text{ CmK}^{-9/2}$)
0.05	77.53142	-0.54343	0.00323	-2.2705E-9
0.1	0.0108	-0.00006	5.3434E-7	-2.2134E-13
0.15	0.00272	-0.00001	1.3617E-7	-3.8086E-14
0.2	0.00345	-0.00003	2.2557E-7	-5.1711E-14

Table 1. Fitting parameters in the temperature variation of $\text{La}_{1-x}\text{Na}_x\text{MnO}_3$ [(a) $x=0.05$, (b) $x=0.1$, (c) $x=0.15$ and (d) $x=0.2$] according to the equation (8)

4.4 Magneto-Resistance (MR) studies of LNMO

MR studies for the samples $\text{La}_{1-x}\text{Na}_x\text{MnO}_3$ ($x = 0.05, 0.1, 0.15, 0.2$ and 0.25) were carried out by taking resistivity in zero magnetic field and in applied fields of 1T, 5T and 8 T, using a standard four probe technique in the temperature range 1.5K – 300K. The resistivity variations are shown in the figure 4.14. The external field causes a reduction in the resistivity in the entire temperature range for all the compositions indicating the colossal magnetoresistance (CMR) property of the manganite samples. The MR measurements of all the samples have been undertaken and the variation of MR with temperature (using magnetic field of 8T) is shown in the figure 4.15. From the figure it is clear that all the samples show a linear increase of MR percentage with decrease in temperature. This behaviour can be explained on the basis of two different mechanisms; one intrinsic and another extrinsic [6]. For micron size manganites the MR percentage is very large near metal insulator transition temperature. Such a behaviour can be ascribed to the intrinsic magneto-resistance (the CMR effect). It is due to the suppression of magnetic fluctuation caused by external magnetic field. This takes place within the volume of the grains and hence called intrinsic. Below the metal insulator transition temperature the magneto-resistance vanishes in the case of a single crystalline material [33]. For polycrystalline samples there is a reduction in MR below the transition temperature. But in our LNMO samples MR increases with decrease of temperature. This contribution is arising from the spin assisted tunneling across the grain boundaries in the material. This is the extrinsic magnetoresistance which is much pronounced in the case of nano sized manganites [6]. This observed grain boundary magneto-resistance is due to the fact that nano size (~ 20 nm) of our LNMO sample. The extrinsic magnetoresistance becomes dominant below the Curie temperature and increases with decrease of temperature.

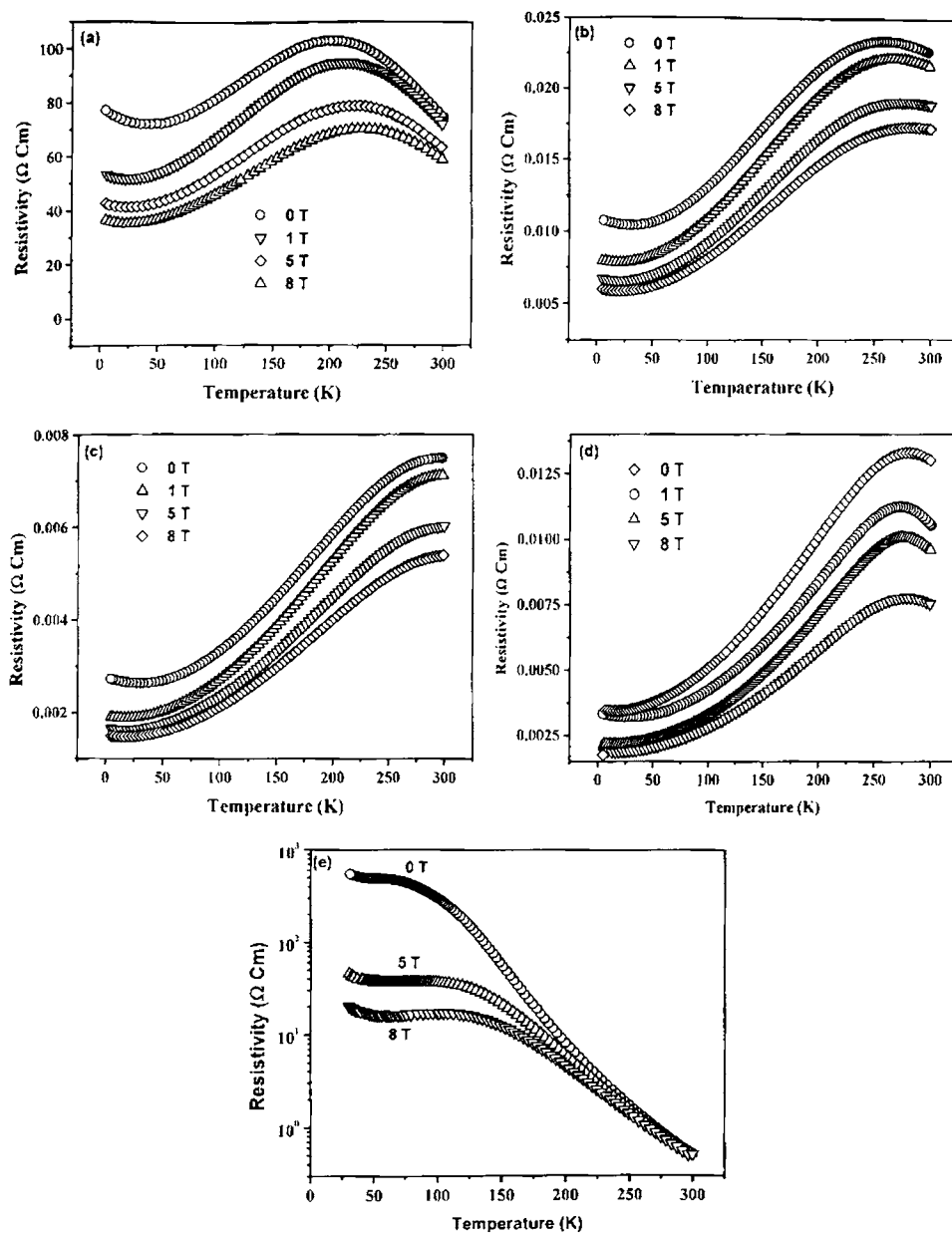


Figure 4.14 Variation of resistivity with temperature at different magnetic fields for the samples $\text{La}_{1-x}\text{Na}_x\text{MnO}_3$ [(a) $x=0.05$, (b) $x=0.1$, (c) $x=0.15$, (d) $x=0.2$ and (e) $x=0.25$]

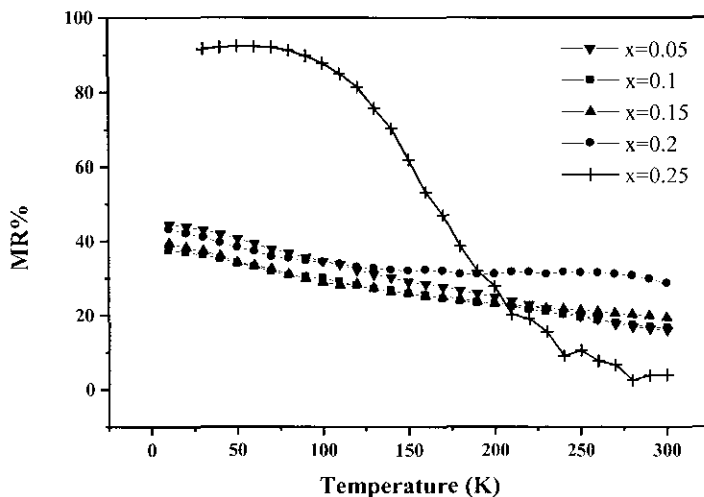


Figure 4.15 Variation of percentage of MR with temperature for the samples

$\text{La}_{1-x}\text{Na}_x\text{MnO}_3$ [$x=0.05$, $x=0.1$, $x=0.15$, $x=0.2$ and $x=0.25$] using a magnetic field of 8T

From figure 4.15 it is clear that all the LNMO samples except composition $x=0.25$ show MR percentage between 15% and 50%. But the composition $x=0.25$ shows a very good value of MR about 93% at around 70K. Below that temperature the value remains constant for a wide temperature range. This observed fact points towards the role of charge ordering in the case of colossal magneto-resistance. The figure 4.16 shows the variations of MR with applied magnetic field at different temperatures. With applied field, MR increases for all the compositions, due to the large suppression of magnetic fluctuation caused by the high magnetic field. In all the graphs there is a kink near 0.2T (H_{cr}) especially in the case of low temperatures. Above and below that critical temperature the variation of MR is a linear function of applied magnetic field. This indicates the coexistence of ferromagnetism with another phase which is weakly conducting or dielectric [34]. Above H_{cr} ferromagnetism contributes to magnetoresistance and below H_{cr} spin polarized tunneling or spin dependent scattering in the weakly conducting phase contributes to MR. Therefore the value of low field magnetoresistance (LFMR) can be easily obtained by extrapolating

the linear portion of the graph above H_{cr} to the MR axis. The value of LFMР thus obtained for the LNMO samples was around 25% for the temperature 5K.

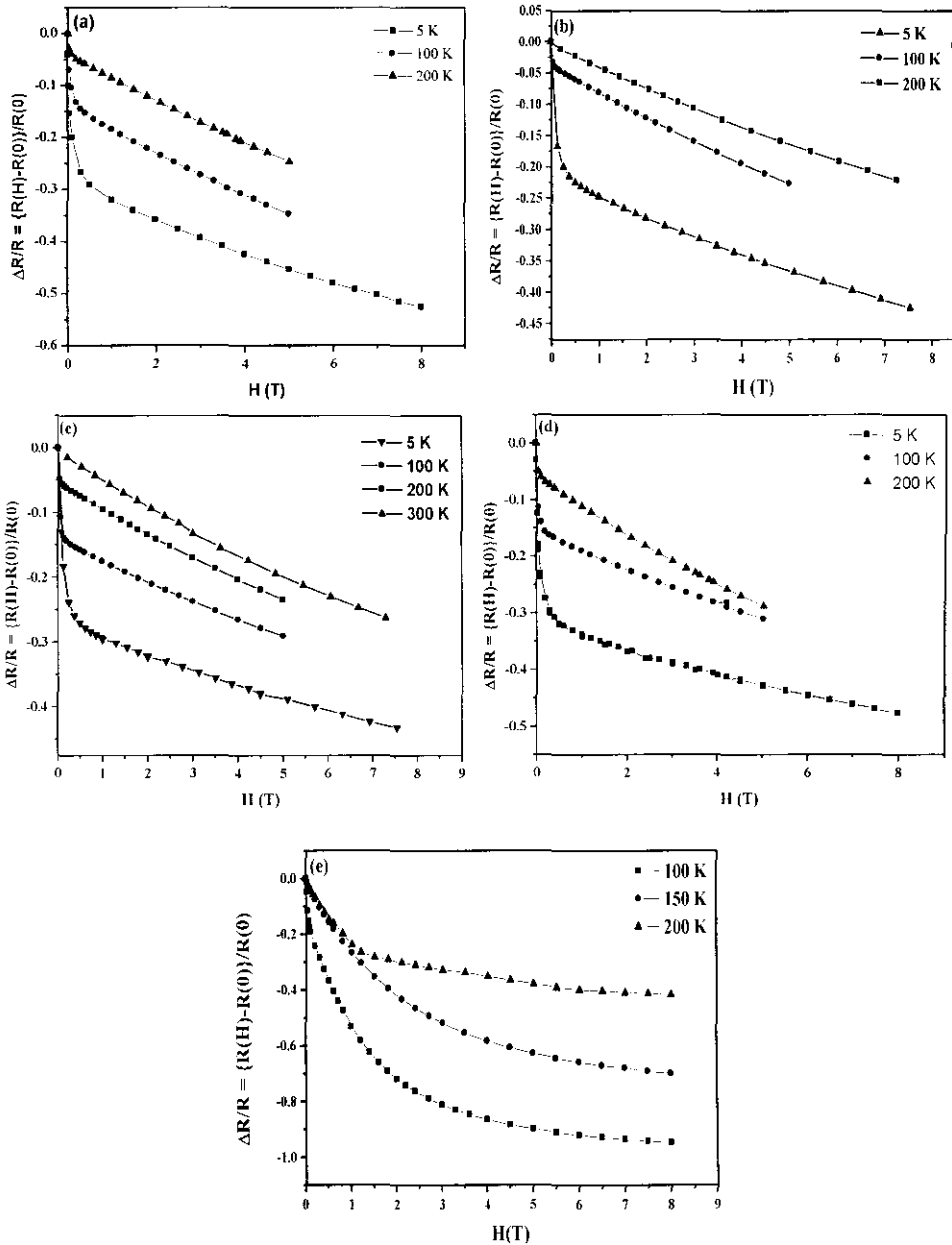


Figure 4.16 Variation of MR with applied magnetic field (zero to 8 T) for the samples

$\text{La}_{1-x}\text{Na}_x\text{MnO}_3$ [(a) $x=0.05$, (b) $x=0.1$, (c) $x=0.15$, (d) $x=0.2$ and (e) $x=0.25$]

4.5 Conclusion

Nanocrystalline LNMO samples ($\text{La}_{1-x}\text{Na}_x\text{MnO}_3$ [$x=0.05$, $x=0.1$, $x=0.15$, $x=0.2$ and $x=0.25$]) were prepared using citrate gel method. The samples were found to have rhombohedrally distorted perovskite structure with particle size around 25 nm. All members of the LNMO series exhibit metal insulator transition. The transition temperature strongly depends on the amount of sodium doping. Due to the enhancement of antiferromagnetic interaction, charge ordering reduces the transition temperature. Magnetisation studies reveal that corresponding to the metal insulator transition, there is ferromagnetic to paramagnetic transition indicating the role of double exchange interaction. The transition temperatures (T_c and T_{M-I}) did not coincide because of grain size effect. D C conductivity studies in the paramagnetic region reveals that SPH is responsible for conduction mechanism except in the charge ordered state, where VRH is more applicable. The dc conductivity fitting in the ferromagnetic region shows an additional $T^{-1/2}$ term, which may be due to weak localization of electron. MR studies reveal that charge ordered LNMO sample has maximum value of MR (93% at 70 K). Linear increase of MR with temperature indicates the spin assisted tunneling magneto-resistance which has a pronounced role in nano sized manganites. The spin assisted tunneling mechanism or spin dependent scattering cause the high value of low field magnetoresistance (LFMR) in the low temperature regime.

References

- [1] Coey J.M.D and Viret M, *Advances in Physics* **48** (1999) 167-293.
- [2] Pollert E, Krupicka S and Kuzmicova E, *J.Phys.Chem.Solid* **43** (1982) 1137.
- [3] Zhao G. M, Conder K, Keller H and Muller K. A, *Nature* **381** (1996) 676.
- [4] El'ad N. Caspi, Maxim Avdeev, Simine Short, and James D. Jorgensen, *Phys. Rev. B* **69** (2004), 104402.

- [5] Rao G. H, Sun J. R, Barner R. K, and Hamad N, *J. Phys.: Condens. Matter* **11** (1999), 1524.
- [6] Kalyana Lakshmi Y, Venkataiah G and Venugopal Reddy P, *J. Appl. Phys.* **106** (2009) 023707.
- [7] Mahendiran R, Mahesh R, Raychaurhuri A K and Rao C N, *Solid State Commun.* **99** (1996) 149.
- [8] Abdelmoula N, Cheikh-Rouhou A and Reversat L, *J. Phys.: Condens. Matter* **13** (2001) 449–458.
- [9] Kusters R. M, Singleton J, Keen D. A, Mc Greevy R and Hayes W, *Physica B* **155** (1989) 362.
- [10] Xiong G. C, Bhagat S. M, Dominguez M, Ju H. L, Greene R. L, Venkatesan T, Byers J. M and Rubinstein M, *Solid St. Commun.* **97** (1996) 599.
- [11] Hundley M.F, Hawley M, Heffner R. H, Jia Q. X, Neumeier J. J, Tesmer J, Thomson J. D and Wu X. D, *Appl. Phys. Lett.* **67** (1995) 860.
- [12] Holstein T, *Ann. of Phys.* **8** (1959) 325.
- [13] Snyder G. J, Hiskes R, DiCarolis S, Beasley M. R and Geballe T. H, *Phys. Rev. B* **53** (1996) 14434.
- [14] Yeh N. C, Vasquez R, Beam D, Fu C. C, Huynh H and Beach G, *J. Phys.: Condens. Matter* **9** (1996) 3713.
- [15] Yeh N. -C, Fu C. -C, Wei J. Y. T, Vasquez R. P, Huynh J, Maurer S. M, Beach G and Beam D. A, *J. Appl. Phys.* **81** (1997) 5499.
- [16] Jakob G, Westerburg W, Martin F and Adrian H, *Phys. Rev. B* **58** (1988) 14966.
- [17] Young Sun, Xiaojun Xu and Yuheng Zhang, *J.Phys.Condens. Matter* **12** (2000) 10475.

- [18] Viret M, Ranno L and Coey J. M. D, *Phys. Rev. B* **55** (1997) 8067.
- [19] von Helmholt R, Haupt L, Bärner K and Sondermann U, *Solid St. Commun.* **82** (1992) 693.
- [20] DeTeresa J. M, Ibarra M. R, Blasco J, Garcia J, Marquina C, Algrabel P, Arnold Z, Kamenev K, Ritter C and von Helmholt R, *Phys. Rev. B* **54** (1996) 1187.
- [21] Coey J. M. D, Viret M, Ranno L and Ounadjela K, *Phys. Rev. Lett.* **75** (1995) 3910.
- [22] de Teresa J. M, Ibarra M. R, Algrabel P. A, Ritter C, Marquina C, Blasco J, Garcia J, del Moral A and Arnold Z, *Nature* **386** (1997) 256.
- [23] Jaime M, Salamon M. B, Pettit K, Rubinstein M, Treece R. E, Horowitz J. S and Chrisey. B, *Appl. Phys. Lett.* **68** (1996) 1576.
- [24] Mott N. F, *Metal-Insulator Transitions*, 2nd edn. Taylor and Francis, London (1990).
- [25] Mott N. F and Davies E. A, *Electronic Processes in Noncrystalline Materials*, Oxford (1971).
- [26] Zhou H. D, Li G, Feng S. J, Liu. Y, Qian. T, Fan X. J and Li X. G, *Solid State Commun.* **122** (2002) 507.
- [27] Zhao S. G, Jin K. X and Chen C. L, *J. Appl. Phys.* **101** (2007) 083701.
- [28] Yi Liu, Hui Kong, Jin-rui Su and Chang-fei Zhu, *Chinese Jr. Of Chemical Physics* **19** (2006) 6.
- [29] Chaudhuri S and Budhani R. C, *Phys. Rev. B* **74** (2006) 054420
- [30] Dinesh Varshney and Kaurav N, *Journal of Low Temperature Physics* **141**(2005) 165.
- [31] Lee P. A and Ramakrishnan T. V, *Rev. Mod. Phys.* **57** (1985) 287.

- [32] Michalopoulou A, Syskakis E and Papastaikoudis C, *J. Phys.: Condens. Matter* **13** (2001) 11615.
- [33] Khazeni K, Jia Y. X, Vincent H Crespi, Lee L, Zettl A and Marvin L Cohen, *J. Phys. Cond. Matter* **8** (1996) 7723.
- [34] Tovstolytkin A. I, Tsmots' V. M, Pan'kiv L. I, Litovchenko P. G and Pan'kiv I. S, *Low Temperature Physics* **36** (2010) 220.

Chapter 5

On the Multiferroic Behaviour of Gadolinium Based Manganites

5.1 Introduction

Ferroelectric and magnetic materials are a time-honored subject of study and have led to some of the most important technological advances [1-4]. Magnetism and ferroelectricity are involved with local spins and off-center structural distortions, respectively. These two seemingly unrelated phenomena can coexist in certain unusual materials, called "multiferroics". Multiferroics, sometimes called "magnetoelectrics", possess two or more switchable states such as polarisation, magnetisation or strain. Multiferroics are of particular interest recently both to understand the fundamental aspects of the novel mechanism that gives rise to this magnetic-ferroelectric coupling, as well as because of the intriguing possibility of using these coupled order parameters in novel device applications. The understanding of the physics of multiferroics will be crucial to design smarter multiferroic materials and control their functionality for practical applications, such as electric-field-controlled ferromagnetic resonance devices, actuators, transducers, and storage devices with either magnetically modulated piezoelectricity or electrically modulated piezomagnetism. The multiferroic nature of manganites $\text{Pr}_{0.6}\text{Ca}_{0.4}\text{MnO}_3$, $\text{Nd}_{0.5}\text{Ca}_{0.5}\text{MnO}_3$ and $\text{Pr}_{0.7}\text{Ca}_{0.3}\text{MnO}_3$ is recently reported and the effect is explained by using the mixing of site centered or bond centered charge ordering mechanisms [5-7]. There is a possibility of obtaining the ferroelectric behaviour for the Gd doped (comparable ionic radius with Pr and Nd) manganite. This chapter deals with the dielectric studies of Gd based manganites along with the a.c conductivity and capacitance-voltage (CV) studies.

5.2 Dielectric permittivity studies of GSMO

The dielectric permittivity studies on the Gd based manganite sample were carried out by using a dielectric cell and an HP 4285 LCR meter in the frequency range 100 kHz- 8 MHz from 145K to 300K. High frequencies are used in the measurement to avoid strong contact contribution at the sample electrode interface, which dominate at low frequencies. The dielectric cell was standardized by using Teflon. The fabrication details of the dielectric cell are cited elsewhere [8]. In the dielectric cell, a capacitor is created by placing the pellet in between two copper discs of the same diameter of the pellet. The temperature was recorded with a Cryocan temperature controller with platinum resistance (PT-100) temperature sensor. The dielectric permittivity is calculated using the following relation from the capacitance data obtained from the LCR meter.

$$\epsilon_r = Cd / \epsilon_0 A \quad (5.1)$$

where C is the capacitance of the sample, A is the surface area of the sample, ϵ_0 is the permittivity of free space. The acquisition of data was automated by interfacing HP 4285A with a computer using a virtual instrumentation package LabVIEW. The variation of dielectric permittivity with frequency at different temperatures for the GSMO sample is given in figure 5.1.

The dielectric permittivity decreases with increase of frequency in the case of all compositions of GSMO sample. The dielectric spectra reveal a quasi-Debye relaxation, which can be explained satisfactorily with the help of a two-or tri layer Maxwell-Wagner capacitor [9]. Considering the compositional dependence on permittivity from figure 5.1, it is clear that there is an increase of dielectric constant with Sr concentration. It is due to the increase of hopping polarisation with increase of Sr doping. The temperature variation of dielectric constant at different frequencies is shown in figure 5.2.

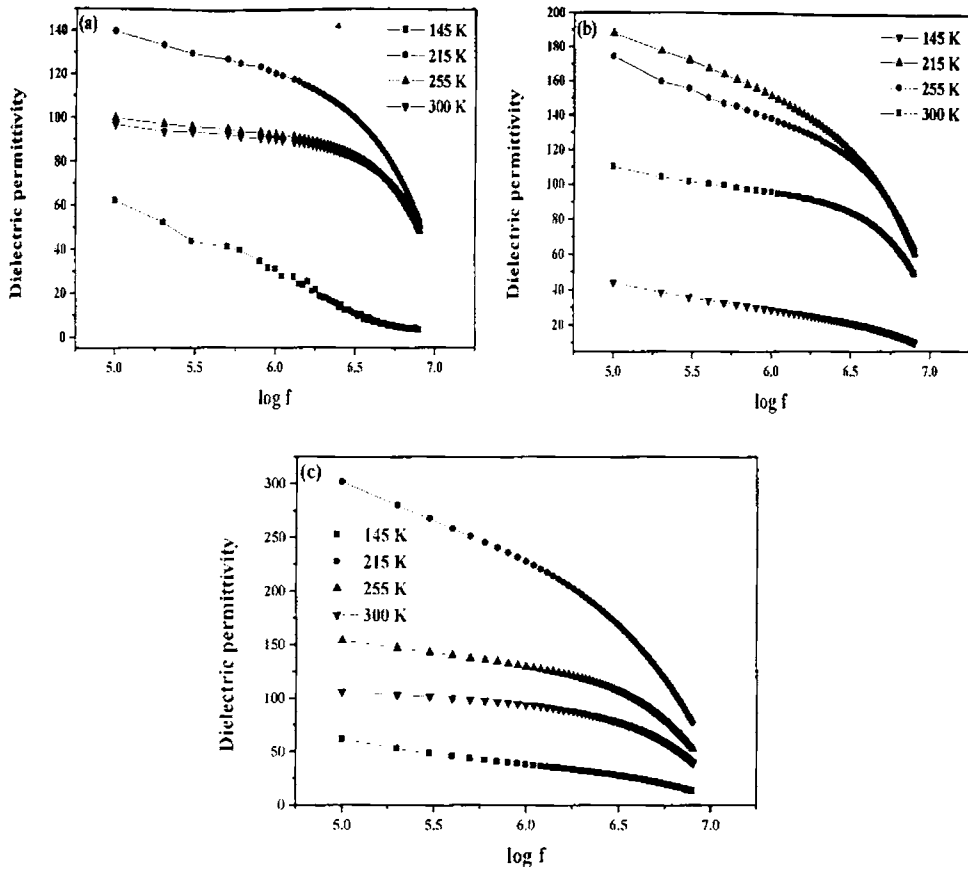


Figure 5.1 Frequency variation of dielectric permittivity for GSMO sample $Gd_{1-x}Sr_xMnO_3$ [(a) $x=0.3$, (b) $x=0.4$ and (c) $x=0.5$] at selected temperatures.

From the figure it is clear that as temperature increases dielectric constant also increases, attains a maximum value and then decreases. The dielectric peak is very close to T_{CO} , which is an evidence of the link between electronic state and increase of dielectric response [9]. The anomaly in dielectric constant at the charge ordering temperature was earlier observed in Pr-Ca manganites [10, 11]. The peak height at the transition temperature was observed to decrease with increase in frequency and the dielectric constant peak get shifted to higher temperature with increase in frequency, which is indicative of the relaxational behaviour of the

material [12]. The word relaxor is used because there is only broad peak instead of sharp peak as in the case of conventional ferroelectric materials.

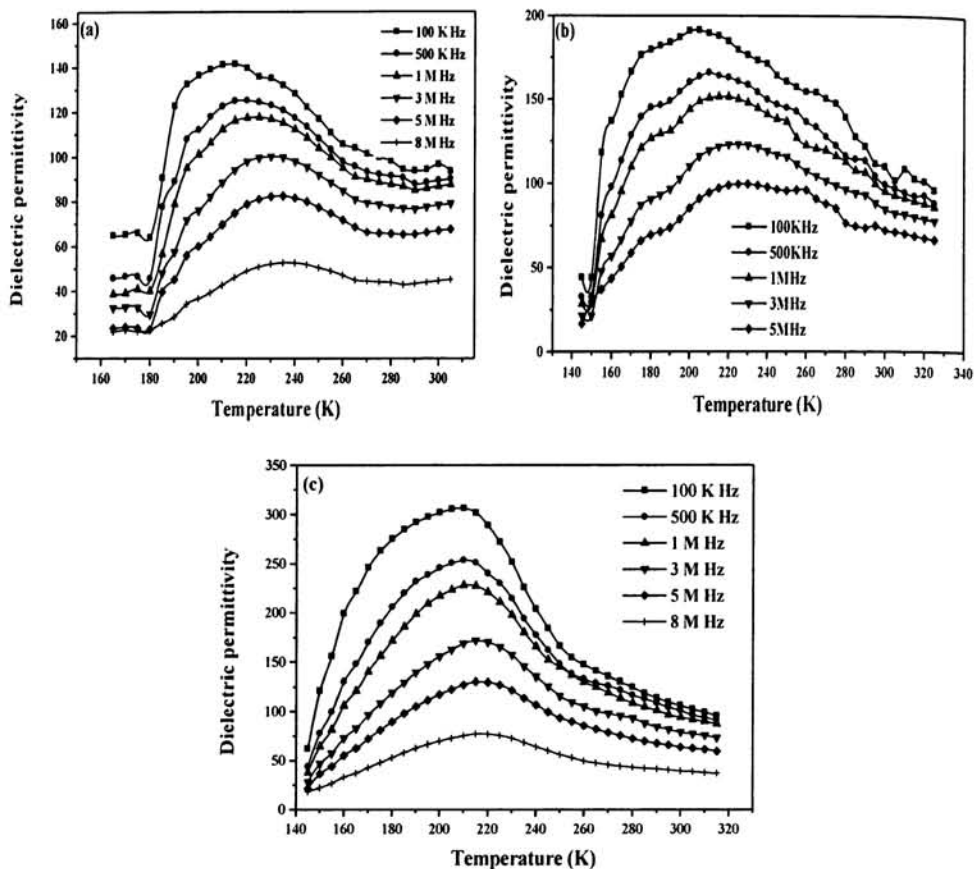


Figure 5.2 The variation of dielectric permittivity with temperature for the samples $Gd_{1-x}Sr_xMnO_3$ [(a) $x=0.3$, (b) $x=0.4$ and (c) $x=0.5$] at selected temperatures.

In the case of manganites the ferroelectric nature can be explained by using intermediate charge ordering state. Charge ordering is usually considered as an ordering of transition metal ions with different valencies (e.g. Mn^{3+}/Mn^{4+} in manganites and Fe^{2+}/Fe^{3+} in ferrites). This charge ordering state is called Site-centered Charge Ordering (SCO). Recently another type of charge ordering is discovered and is called Bond-centered Charge Ordering (BCO). This state is

actually an oxygen centered charge ordering state as oxygen ions are located on the TM-TM bonds in the typical perovskite crystal structure. With in such a dimer spins are aligned ferromagnetically due to Zener double exchange mechanism. It is referred to as Zener polaron state. In SCO Mn ions have unequal valencies but in BCO they have the same valency. The superposition of these two states results into a ferroelectric intermediate state. The CE structure (SCO) has a center of inversion symmetry and consequently there are no electric dipole moments present in the ground state. This is also the case in the pure Zener polaron structure (BCO) as both the Mn ions in each dimer are equivalent. But the intermediate state has a magnetic structure in which the inversion symmetry is lost and the dimer attains a dipole moment. Thus there is a net polarisation which leads to a ferro-electric ground state [6, 13]. The three states are depicted in figure 5.3.

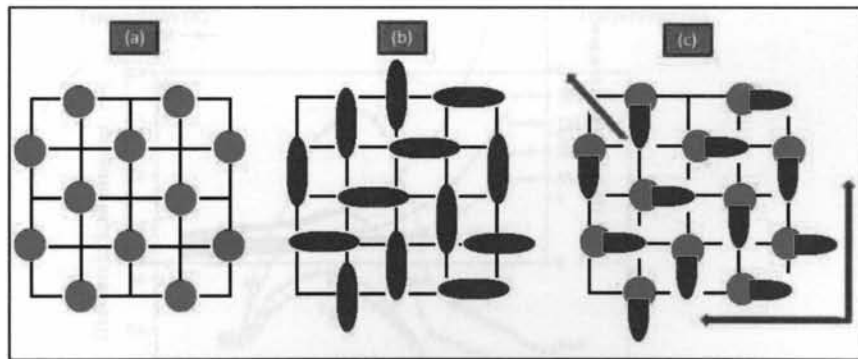


Figure 5.3 (a) Site centered Charge Order (SCO) (b) Bond centered Charge Order (BCO) or Zener Polaron state (c) Intermediate ferroelectric state

The frequency variation of dielectric loss tangent for the GSMO sample is depicted in the figure 5.4 and the variation of dielectric loss tangent with temperature is shown in figure 5.5. As frequency increases dielectric loss tangent decreases. The high frequency decrease of dielectric loss tangent can be explained

by considering the RC equivalent circuit of a lossy dielectric material. In the parallel combination of resistor and capacitor, the decrease of capacitive reactance

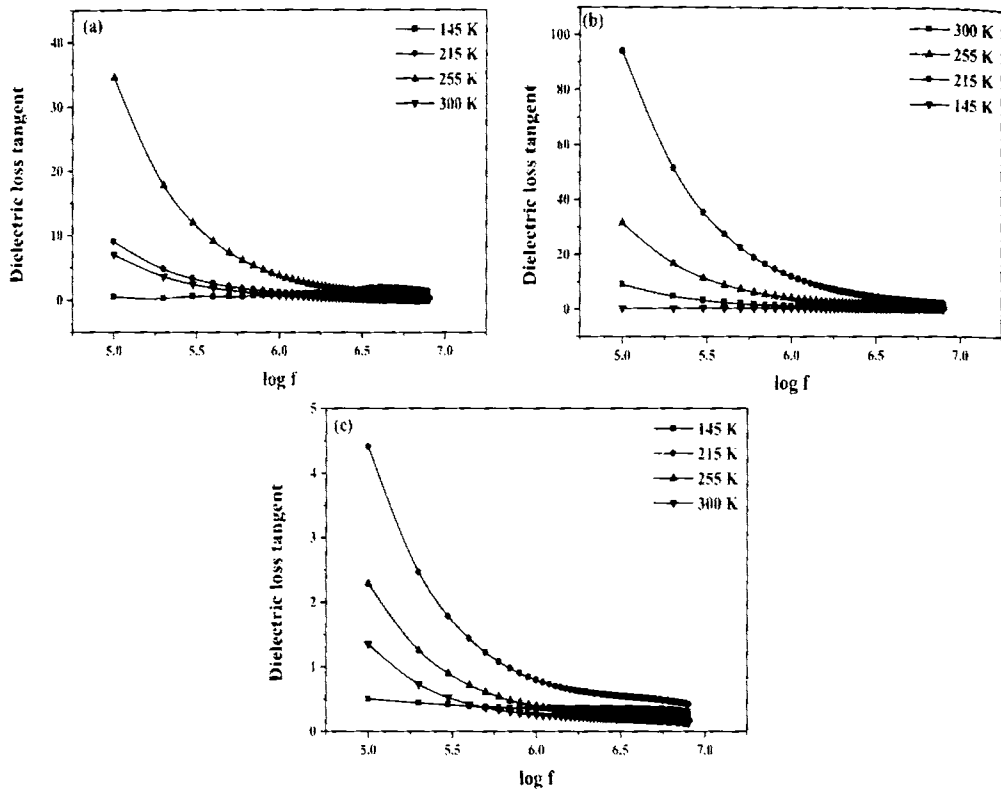


Figure 5.4 Frequency variation of dielectric loss tangent for GSMO sample $Gd_{1-x}Sr_xMnO_3$ [(a) $x=0.3$, (b) $x=0.4$ and (c) $x=0.5$] at selected temperatures.

at high frequency causes a decrease of charge flow across the resistor, which in turn reduces the energy dissipation across the resistor. The temperature variation of dielectric loss tangent has the same behaviour as that of the dielectric permittivity except the shifting of the peak temperature towards 255K and 260K for $Gd_{0.6}Sr_{0.4}MnO_3$ and $Gd_{0.7}Sr_{0.3}MnO_3$ respectively. This shift of dielectric loss peak is due to the fact that it usually appears at certain temperature where the dielectric constant varies quickly [14]. The quick decrease of dielectric

permittivity at 220K for $Gd_{0.5}Sr_{0.5}MnO_3$ resulted into the occurrence of dielectric loss peak at the same temperature. But in the case of $Gd_{0.6}Sr_{0.4}MnO_3$ and $Gd_{0.7}Sr_{0.3}MnO_3$ dielectric permittivity peak is very broad and a quick decrease occurs at comparatively higher temperatures.

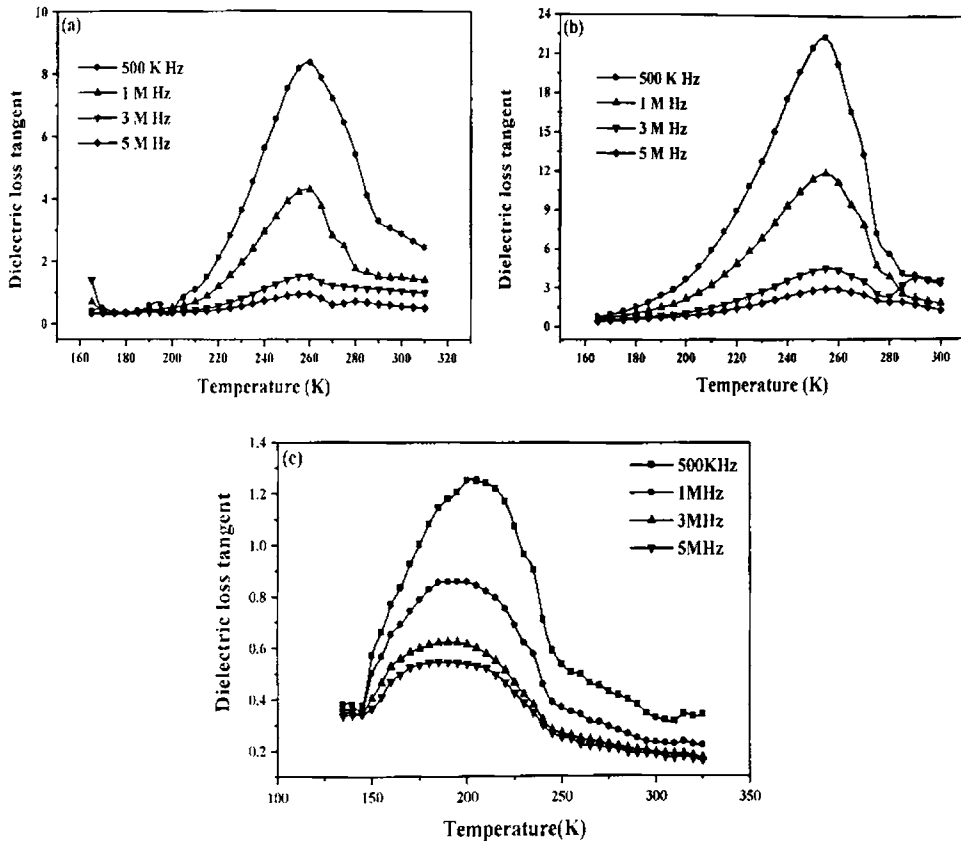


Figure 5.5 Temperature variation of dielectric loss tangent for GSMO sample $Gd_{1-x}Sr_xMnO_3$ [(a) $x=0.3$, (b) $x=0.4$ and (c) $x=0.5$] at selected frequencies.

The dielectric loss of the material was measured by using the equation

$$\epsilon'' = \epsilon' \tan \delta \quad (5.2)$$

where $\tan\delta$ is the dielectric loss tangent. The frequency and temperature variations of dielectric loss (imaginary permittivity) for the GSMO samples are shown in figure 5.6 and figure 5.7. The sample exhibits the same behaviour as in the case of loss tangent.

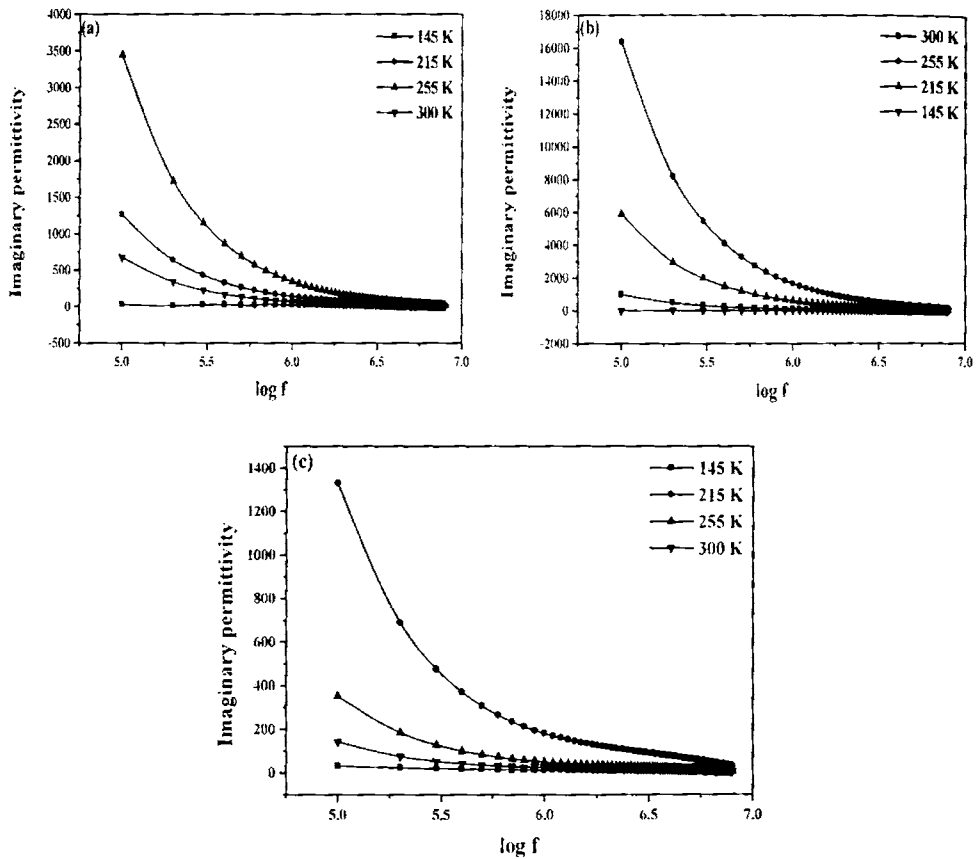


Figure 5.6 Frequency variation of dielectric loss for GSMO sample $\text{Gd}_{1-x}\text{Sr}_x\text{MnO}_3$ [(a) $x=0.3$, (b) $x=0.4$ and (c) $x=0.5$] at selected temperatures.

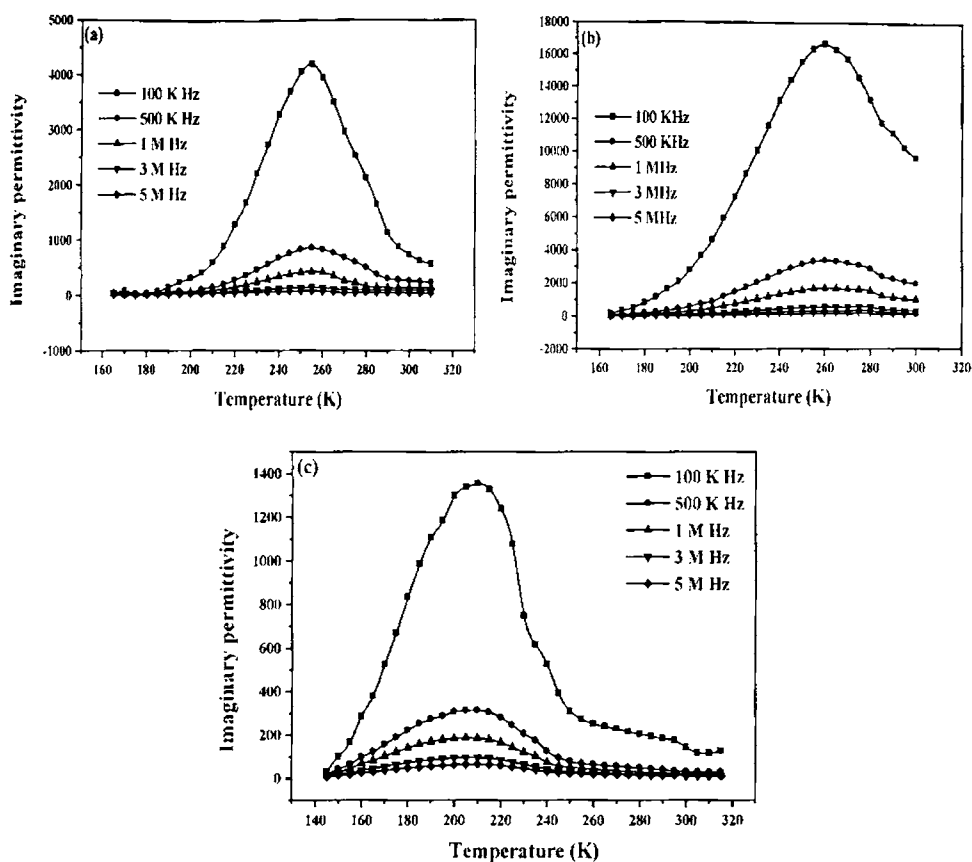


Figure 5.7 Temperature variation of dielectric loss for GSMO sample $\text{Gd}_{1-x}\text{Sr}_x\text{MnO}_3$ [(a) $x=0.3$, (b) $x=0.4$ and (c) $x=0.5$] at selected frequencies.

5.3 Capacitance Voltage (CV) measurements in GSMO

In order to confirm the ferroelectric property of GSMO sample, the capacitance versus voltage (CV) measurements were carried out using an HP 4192 A impedance analyser. The sample in the form of pellet was placed in between two copper plates in the dielectric cell and the capacitance values were measured by varying bias voltage from -8 V to +8 V in a step of 1V. The variation of capacitance with applied bias voltage at room temperature is presented in figure 5.8. The butterfly nature of the figure is an indication of ferroelectricity in GSMO

sample [15]. The change in capacitance with applied bias voltage is pronounced in the case of $Gd_{0.5}Sr_{0.5}MnO_3$ which confirms the role of charge ordering in the multiferroic behaviour of the manganite sample.

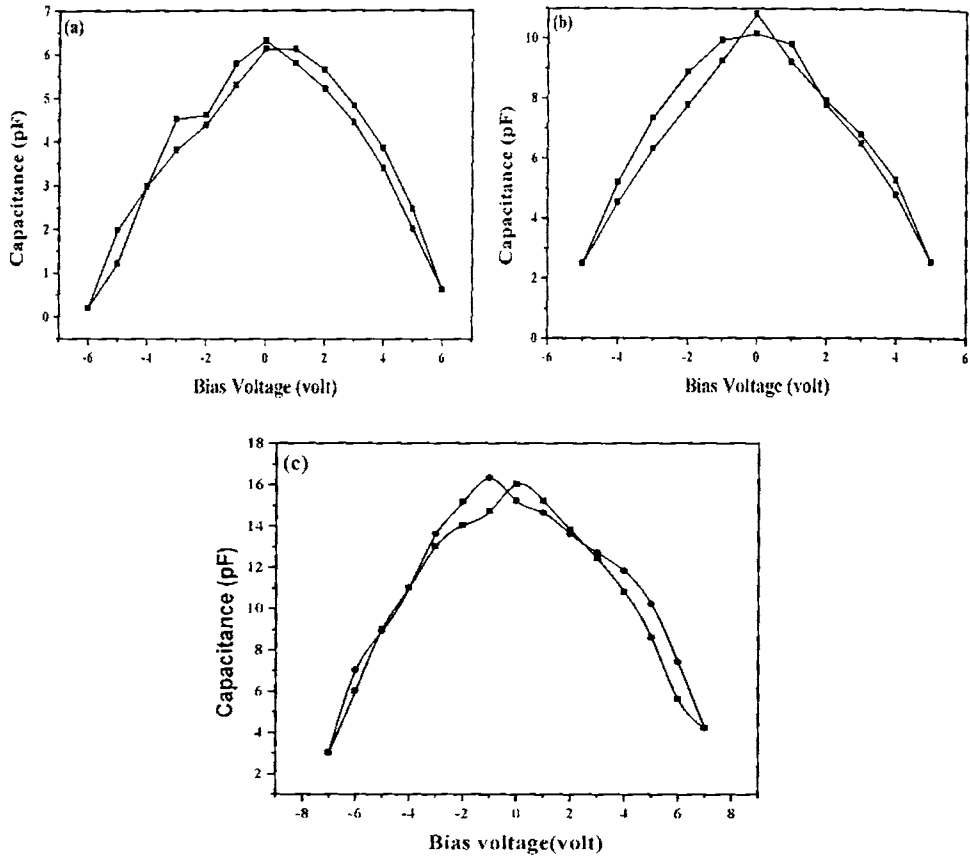


Figure 5.8 Variation of capacitance with bias voltage for GSMO sample $Gd_{1-x}Sr_xMnO_3$ [(a) $x=0.3$, (b) $x=0.4$ and (c) $x=0.5$] at frequency 1MHz.

5.4 A. C conductivity studies in GSMO

Ac conductivity values of GSMO samples were obtained from the dielectric permittivity (ϵ') and dielectric loss tangent ($\tan \delta$) using the equation

$$\sigma_{ac} = 2\pi f \epsilon_0 \epsilon' \tan \delta \quad (5.3)$$

where f is the frequency of ac applied field and ϵ_0 is permittivity of free space.

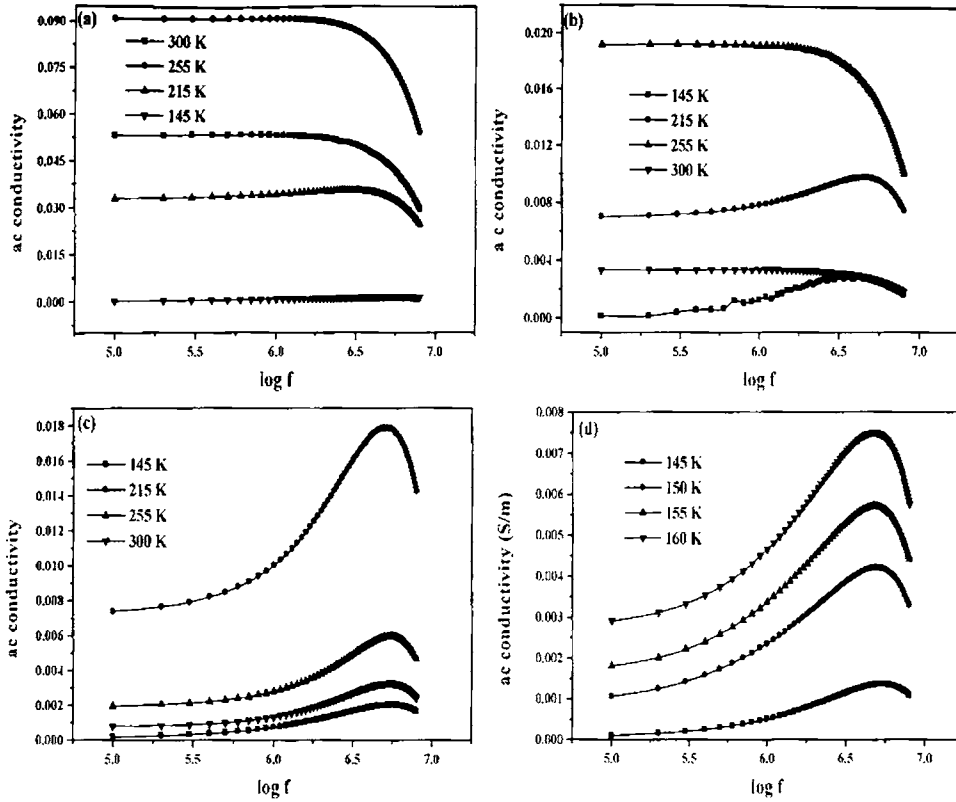


Figure 5.9 Frequency variation of ac conductivity for GSMO sample $\text{Gd}_{1-x}\text{Sr}_x\text{MnO}_3$ [(a) $x=0.3$, (b) $x=0.4$ and (c) $x=0.5$] at selected temperatures. (d) frequency variation of ac conductivity in the temperature range (145K-160K) for the GSMO sample $x=0.3$.

The variation of the ac conductivity with frequency at different temperatures for the samples $\text{Gd}_{1-x}\text{Sr}_x\text{MnO}_3$ ($x=0.3$, $x=0.4$ and $x=0.5$) is plotted in a semi log plot (figure 5.9). In the case of GSMO with $x=0.3$ and $x=0.4$, at lower frequencies, there is a small increase in ac conductivity for temperatures lower than the relaxor ferroelectric transition temperature and above that particular temperature the ac conductivity is frequency independent. But for higher frequencies the ac conductivity decreases with increase of frequency. For $x=0.3$, the appearance of frequency independent behaviour at low temperatures in the diagram is due to the large Y-axis scale value which can be confirmed from figure 5.9 (d). But for

GSMO with $x=0.5$, as frequency increases the ac conductivity increases, attains a maximum and then decreases. The increase in ac conductivity is due to the hopping mechanism of bound charges back and forth between well defined bound states [16]. But at higher frequencies the hopping of charge carriers could not follow the applied field, resulting in the decrease of ac conductivity. From figure 5.9 it is clear that the ac conductivity value decreases with increase of Sr doping. This behaviour may be due to the increase in number of Mn^{4+} ion sites at the expense of Mn^{3+} site with increase of Sr doping. As a result the available Mn^{3+} - Mn^{4+} pairs for hopping decreases and hence the ac conductivity due to the jumping between bound states decreases.

In general ac conductivity power law is given by

$$\sigma = \sigma(0) + A\omega^n \quad (5.4)$$

where $\sigma(0)$ is the frequency independent contribution from dc conductivity, A is constant, ω is angular frequency of the applied field and n is the power law exponent [17,18]. From the equation it is clear that the variation of $\log \sigma$ with $\log \omega$ is a straight line and the slope of the straight line graph is the power law exponent 'n'. The log-log plot of ac conductivity with angular frequency of the applied electric field in the low frequency region (where ac conductivity increases with frequency) for all the three GSMO compositions are presented in figure 5.10.

All the plots are straight lines and the slopes of the straight lines are calculated using linear fitting. The power law exponents thus obtained are plotted against temperature and the variation is presented in figure 5.11. The different mechanisms for ac conduction are overlapping large polaron tunneling (OLPT) and correlated barrier hopping (CBH) [19]. The OLPT model predicts a minimum value of 'n' followed by an increase. A decrease of n with increase of temperature is according to the correlated barrier hopping (CBH). For the compositions $x=0.3$

and $x=0.4$, as temperature increases the power law exponent ‘n’ decreases and at around 210 K it becomes almost constant.

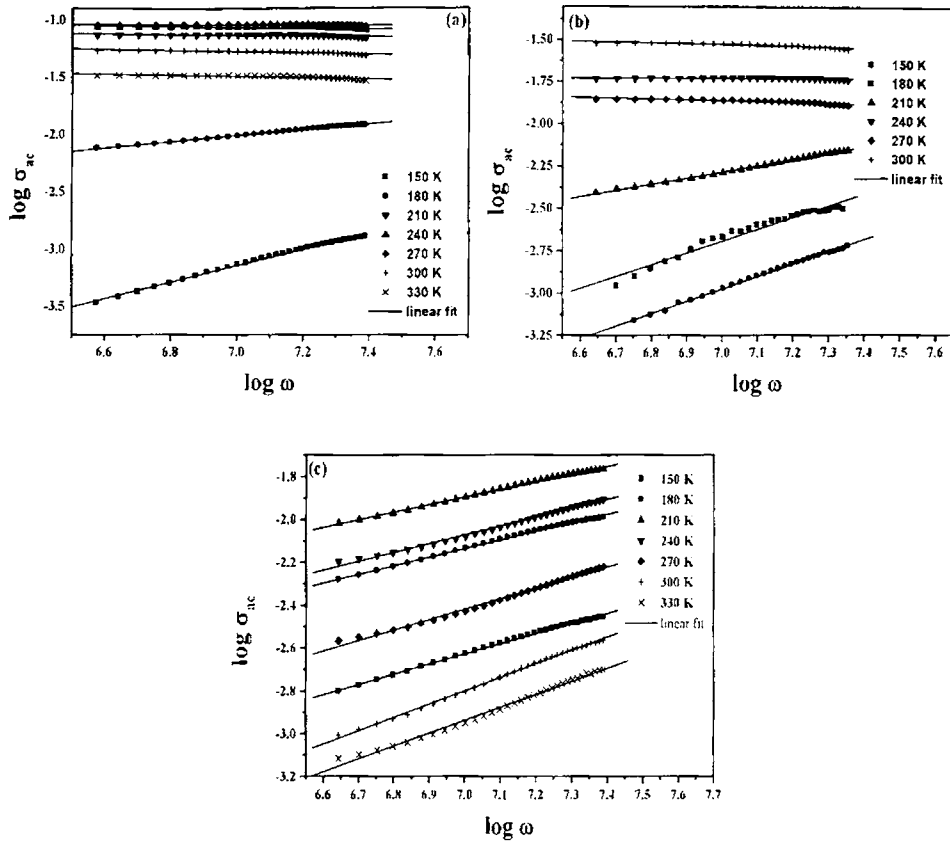


Figure 5.10 Log log plot of frequency variation of ac conductivity for GSMO sample

$Gd_{1-x}Sr_xMnO_3$ [(a) $x=0.3$, (b) $x=0.4$ and (c) $x=0.5$] at selected temperatures.

Thus for the above mentioned compositions the ac conduction mechanism is CBH below the ferroelectric transition temperature. Above the transition temperature the steady value of n indicates the frequency independent nature of ac conductivity. The frequency dependence of conductivity is a characteristic of hopping conduction. The decrease of n value with temperature indicates that as temperature increases hopping conduction decreases. Deepam Maurya et al. reported a similar behaviour in the case of ferroelectric Na doped potassium

titanate ceramics [20]. The temperature variation of power law exponent of the composition $x=0.5$ has different behaviour. With increase in temperature, the power law exponent 'n' decreases, attains a minimum and then increases. Therefore the possible ac conductivity mechanism is overlapping large polaron. This is due to the fact that large concentration of Sr can reduce the number of $Mn^{3+}-Mn^{4+}$ pairs and consequently hopping gets reduced. In such case the spatial extend of polaron covers several inter atomic distances resulting into formation of overlapping large polaron [21].

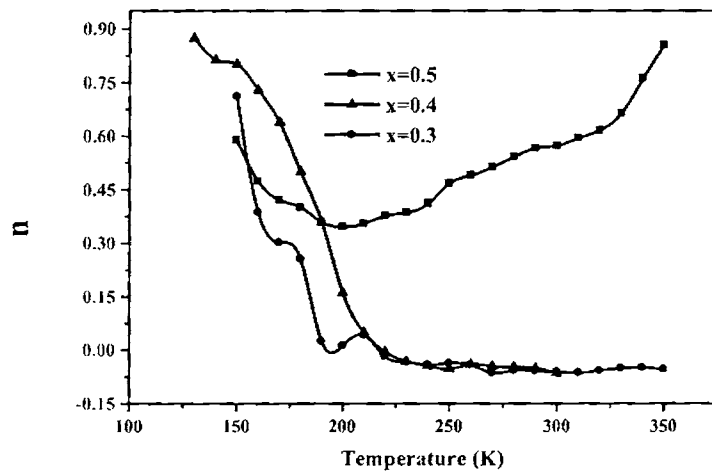


Figure 5.11 Temperature variation of power exponent of ac conductivity for GSMO sample $Gd_{1-x}Sr_xMnO_3$ ($x=0.3, 0.4$ and $x=0.5$)

5.5 Conclusion

The frequency and temperature dependence of the dielectric parameters of the Sr doped Gadolinium manganites were studied. The frequency dispersion of the dielectric parameters was explained using a two-or tri layer Maxwell-Wagner capacitor. The temperature variation of dielectric permittivity shows a broad peak near the charge ordering temperature. This dielectric anomaly is due to the relaxational behaviour of the GSMO sample. The ferroelectric behaviour is explained by inversion symmetry loss in the intermediate charge ordering state

between site centered charge ordering (SCO) and bond centered charge ordering (BCO). The ferroelectric behaviour of the GSMO samples was verified by capacitance voltage measurement, where butterfly curves appear. The increase in ac conductivity is attributed to the hopping mechanism of bound charges back and forth between well defined bound states. The decrease of ac conductivity value with Sr doping may be due to the increase in number of Mn^{4+} ion sites at the expense of Mn^{3+} sites with increase of Sr doping, which results in shortage of Mn^{3+} - Mn^{4+} pairs. The frequency dependent term of ac conductivity was analyzed using power law and the power law exponents (n) were evaluated. Based on the variation of n with temperature, appropriate conduction mechanisms were proposed for different compositions.

References

- [1] Spaldin N. A, *Physics world* April, **20** (2004).
- [2] Hill N. A and Filippetti A, *J. Mag. Mag. Mater.* **976** (2002) 242.
- [3] Hill N. A, *J. Phys. Chem. B* **104** (2000) 6694.
- [4] Kimura T, Goto T, Shintani H, Ishizaka K, Arima T and Tokura Y, *Nature* **426** (2003) 55.
- [5] Claudy Rayan Serrao, Sundaresan A and Rao C. N. R, *J. Phys.: Condens. Matter* **19** (2007) 496217.
- [6] Dmitry V. Efremov, Jeroen van den Brink and Daniel I. Khomskii, *Nature materials* **3** (2004) 853.
- [7] Biskup N, de Andres A and Martínez J. L, *Phys. Rev. B* **72** (2005) 024115.
- [8] Mohammed E. M, Anantharaman M. R, *J. Instrum. Soc. India* **32**(3) (2002) 165.
- [9] Rivas J, Rivas-Murias B, Fondado A, Mira J and Senarís-Rodríguez M. A, *Appl. Phys. Lett.* **85** (2004) 6226.

- [10] Jardon C, Rivadulla F, Hueso L. E, Fondado A, Lopez-Quintela M. A, Rivas J, Zysler R, Causa M. T and Sanchez R. D, *J.Magn.Magn.Mater.* **196** (1999) 475.
- [11] Merccone S, Wahl A, Pautrat A, Pollet M and Simon C, *Phys.Rev.B* **69** (2004)174433.
- [12] Goodman G, Buchanan R. C, and Reynolds III T. G, *Ceramic materials for electronics; Processing, properties, and applications*, Marcel Dekker Inc., New York (1991).
- [13] Botta P. M, Mira J, Fondado A and Rivas J, *Materials Letters* **61** (2007) 2992.
- [14] Wang Wei, Wang Xiao-Juan, Zhu Jun, Mao Xiang-Yu and Chen Xiao-Bing, *Chinese Physics Letters* **26** (2009) 047701.
- [15] Claudy Rayan Serrao, Asish K. Kundu, Krupanidhi S. B, Umesh V. Waghmare and Rao C. N. R, *Phys. Rev. B* **72** (2005) 220101.
- [16] Devan R. S, Kolekar Y. D and Chougule B. K, *J. Phys.: Condens. Matter* **18** (2006) 9809.
- [17] Aloka Ghosh, Bhattacharya S, Bhattacharya D. P and Ghosh A, *J. Phys.: Condens. Matter* **20** (2008) 035203.
- [18] Elimat Z. M, *J. Phys. D: Appl. Phys.* **39** (2006) 2824.
- [19] Aswini Ghosh, *Phys. Rev. B* **42** (1990) 1388.
- [20] Deepam Maurya, Jitendra Kumar and Shripal, *J. Appl. Phys.* **100** (2006) 034103.
- [21] Veena Gopalan E, Malini K. A, Sagar S, Sakthi Kumar D, Yasuhiko Yoshida, Al-Omari I. A and Anantharaman M. R, *J. Phys. D: Appl. Phys.* **42** (2009) 165005.

Chapter 6

Dielectric and Impedance Spectroscopic Studies of Sodium Doped Lanthanum Manganites

6.1 Introduction

Manganites attracted the attention of the scientific community because of multiferroic property exhibited by Ca doped rare earth manganites. Charge ordering plays a crucial role in deciding the ferroelectric property exhibited by compounds. Large band width manganites with divalent alkaline earth cation show charge ordering (equal amounts of Mn^{3+} and Mn^{4+} ions) at doping level $x = 0.5$ and in the case of intermediate band width manganite with Na doping, for every amount of Na, twice the amount of Mn^{3+} will be converted to Mn^{4+} and hence even a small amount of Na doping results in a large number of charge carriers and consequently charge ordering takes place at $x = 0.25$. So manganites doped with Na are prospective ferroelectric materials.

Most of the ferroelectrics exhibit dielectric relaxation and in some cases they display more than one relaxation. The study of those relaxation shed light into the different polarisation mechanisms contributing to total polarisation of the material. Dispersion parameters of the dielectric material are important from the physics point of view. But evaluation of dispersion parameters is not straight forward and often involves indirect methods. The Cole – Cole plot analysis is one such method to evaluate the dielectric parameters. In the case of nano sized compounds predominant contribution to dielectric permittivity is from space charge polarisation arising from grain boundary. Therefore the dielectric spectroscopic studies of nano sized Na doped manganites assume significance in the context of multiferroicity resulting from charge ordering.

6.2 Dielectric studies of LNMO

Dielectric permittivity measurements were conducted on LNMO samples $\text{La}_{1-x}\text{Na}_x\text{MnO}_3$ ($x=0.05, 0.1, 0.15$ and 0.2) using an HP 4285 A impedance analyzer and a homemade dielectric cell under a vacuum of 10^{-3} mbar and temperatures varying from 95 K to 300 K. The fabrication details of the dielectric cell are cited elsewhere [1]. Nano sized particles of LNMO samples were pressed into pellets of size 12 mm in diameter and approximately 2 mm in thickness. These pellets were sintered at temperature 1100° C for 12 hours to achieve maximum compactness. In the dielectric cell, a capacitor is created by placing the pellet in between two copper discs of the same diameter of the pellet and the capacitance and dielectric loss tangent were measured using the impedance analyser in the frequency range of 100 kHz to 8MHz. The temperature was recorded with a Cryocan temperature controller with platinum resistance (PT-100) temperature sensor. The dielectric permittivity of the material was calculated from the measured values of capacitance using the relation

$$\epsilon' = \frac{C \cdot d}{\epsilon_0 A} \quad (6.1)$$

where ϵ' is the dielectric permittivity of the sample (real part), C is the capacitance of the capacitor formed by inserting the sample between two metal plates, d is the thickness of the sample, A is the area of the sample and ϵ_0 is the permittivity of free space. The dielectric loss of the material was measured by using the equation

$$\epsilon'' = \epsilon' \tan \delta \quad (6.2)$$

where $\tan \delta$ is the dielectric loss tangent.

The dielectric permittivity is a measure of the ability of a material to polarize under the application of an electric field. In nano sized manganites the main contribution of polarisation is from space charge polarisation which is the

sum of interfacial polarisation at the grain boundaries and hopping polarisation [2]. The variation of dielectric permittivity with frequency at selected temperatures for the samples $\text{La}_{1-x}\text{Na}_x\text{MnO}_3$ ($x=0.05, 0.1, 0.15$ and 0.2) is presented in figure 6.1, as a semi log plot in which logarithm of frequency is along the x-axis and dielectric permittivity is along the y-axis.

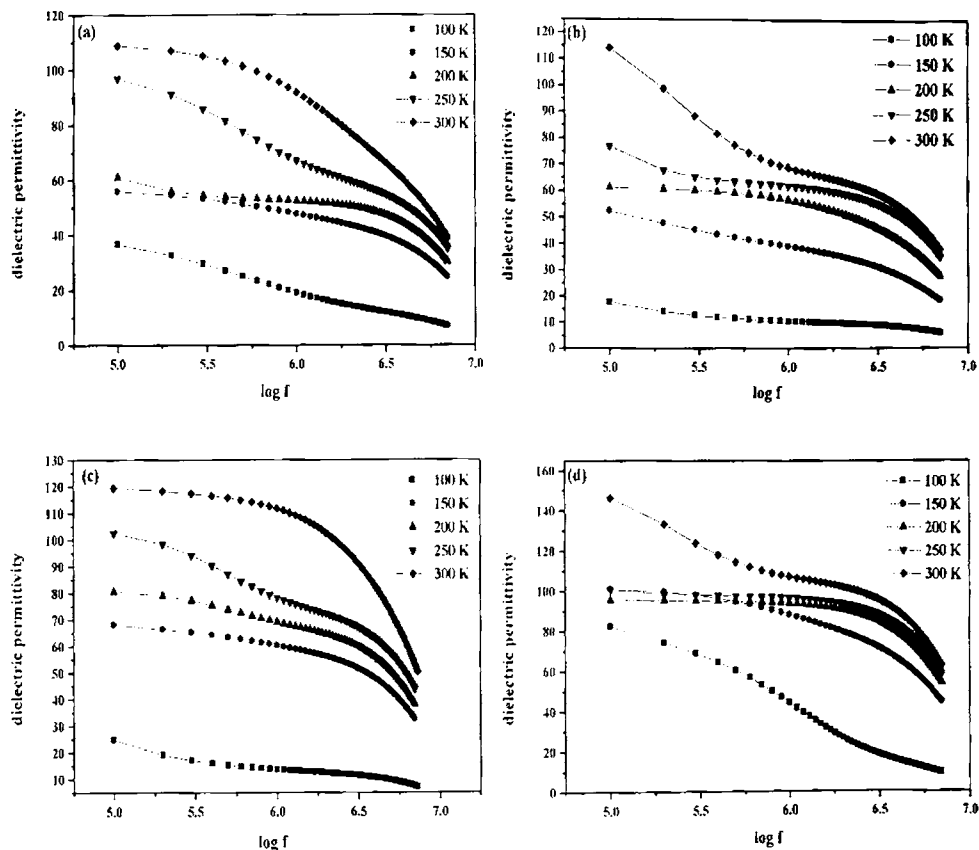


Figure 6.1 Frequency variation of dielectric permittivity for LNMO sample $\text{La}_{1-x}\text{Na}_x\text{MnO}_3$ ($x=0.05, 0.1, 0.15$ and 0.20) at selected temperatures.

It can be observed that as frequency increases, the permittivity value decreases, from an initial plateau value. This phenomenon can be understood on the basis of Koop's theory which considers the dielectric structure as an inhomogeneous medium of two layers of the Maxwell-Wagner type [3, 4]. In this

model, the dielectric structure is assumed to be consisting of well conducting grains which are separated by poorly conducting grain boundaries. At high frequencies the jumping frequency of electric charge carriers can not follow the alternation of applied field and polarisation gradually decreases with increase of frequency.

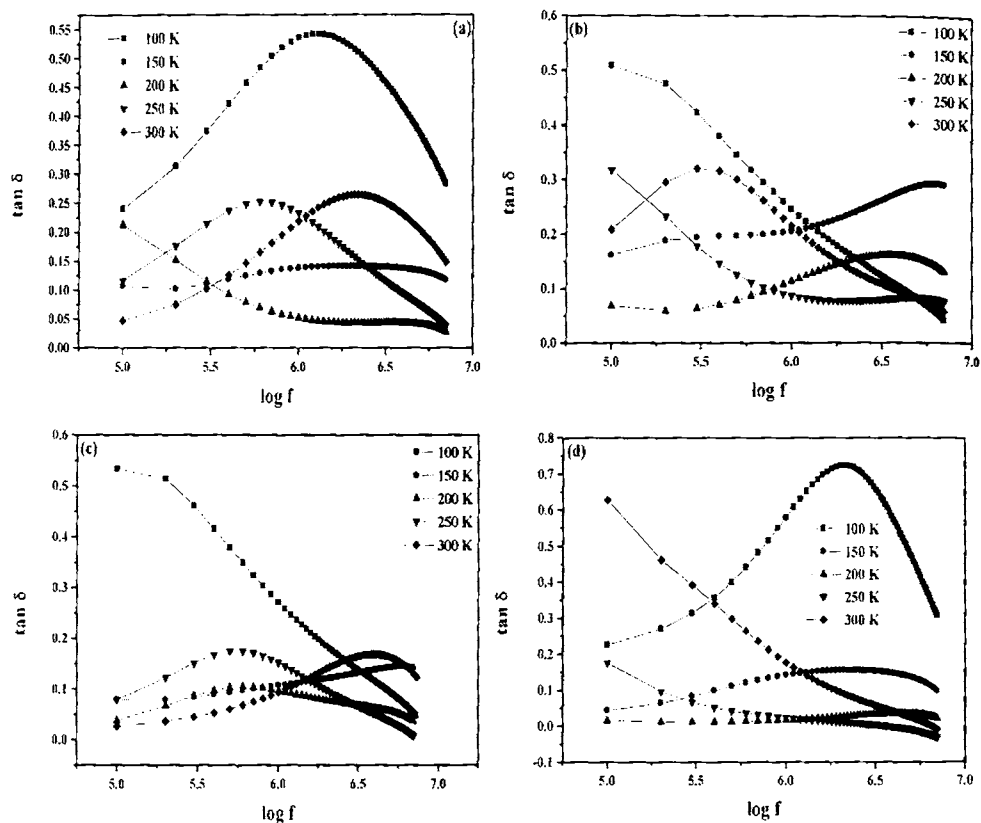


Figure 6.2 Frequency variation of dielectric loss tangent LNMO sample $\text{La}_{1-x}\text{Na}_x\text{MnO}_3$ (a) $x=0.05$, (b) $x=0.1$, (c) $x=0.15$ and (d) $x=0.2$ at selected temperatures.

Considering the compositional dependence on permittivity from figure 6.1, it is clear that at high temperature, there is an increase of dielectric constant with Na concentration for the LNMO samples. This may be due to the increase of hopping polarisation with Na doping.

The frequency variation of dielectric loss tangent for the LNMO samples at different temperatures is shown in figure 6.2. From the figure it is clear that near 100 K and in the temperature range 200K - 300K, the dielectric loss tangent initially increases with frequency, attains a maximum and then decreases (i.e., a relaxation behaviour). The decrease of dielectric loss tangent at high frequencies can be explained by considering the RC equivalent circuit of a lossy dielectric material. In the parallel combination of resistor and capacitor, the decrease of capacitive reactance at high frequency causes a decrease of charge flow across the resistor, which in turn reduces the energy dissipation across the resistor. The loss peak is sharp near 100K and broad in the temperature range 200K - 300K.

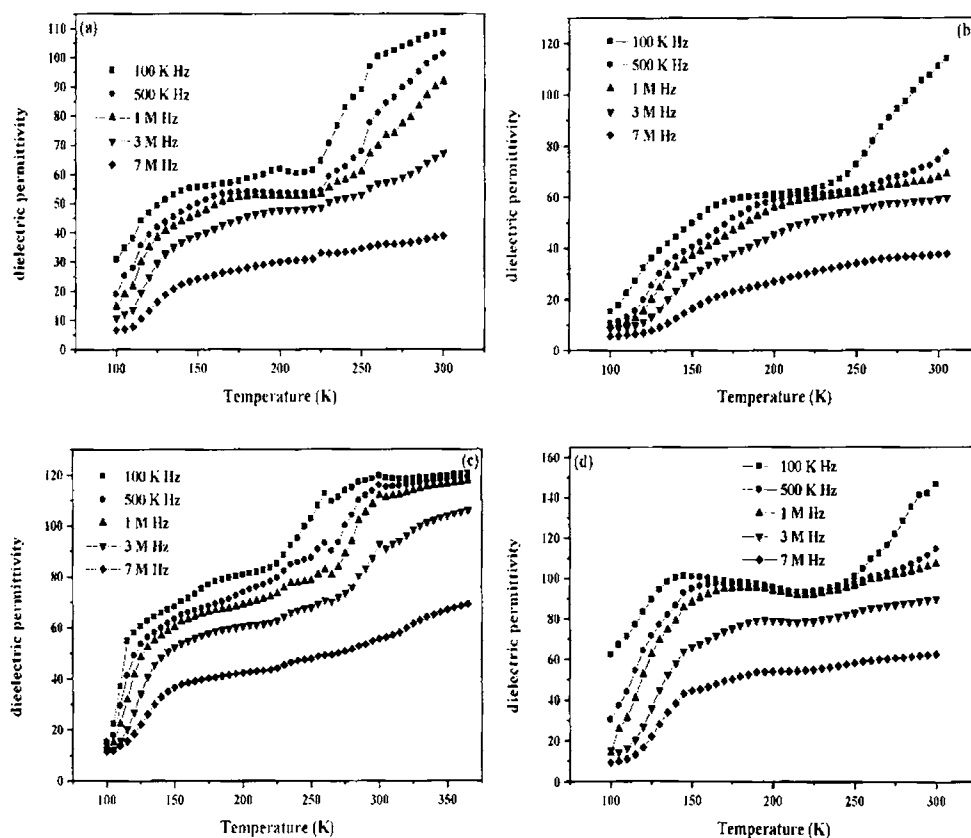


Figure 6.3 The variation of dielectric permittivity with temperature for the samples

$\text{La}_{1-x}\text{Na}_x\text{MnO}_3$ [(a) $x = 0.05$, (b) $x = 0.1$, (c) $x = 0.15$ and (d) $x = 0.2$]

The variation of dielectric permittivity with temperature at selected frequencies for the samples $\text{La}_{1-x}\text{Na}_x\text{MnO}_3$ ($x=0.05, 0.1, 0.15, 0.2$ and 0.25) is presented in figure 6.3. For the LNMO sample corresponding to the composition $x=0.15$, the dielectric study is extended to 365K in order to obtain a wide temperature window. All the LNMO samples show almost similar behaviour. There are two plateaus; one at lower temperature (near 100 K) and another at higher temperature (above 150K) with a step like increase connecting them. The decrease of dielectric permittivity with decrease of temperature can be understood from the fact that as temperature decreases the relaxing entities can no longer follow the applied ac field. The plateau formation is pronounced at low

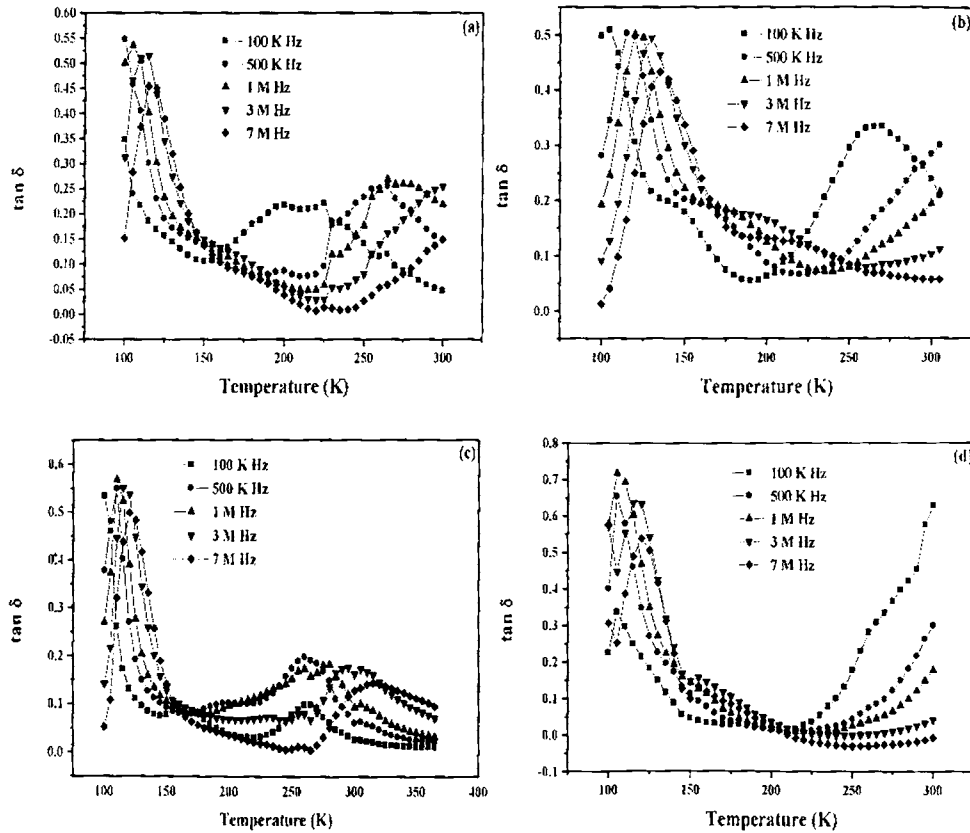


Figure 6.4 The variation of dielectric loss with temperature for the samples $\text{La}_{1-x}\text{Na}_x\text{MnO}_3$ [(a) $x = 0.05$, (b) $x = 0.1$, (c) $x = 0.15$ and (d) $x = 0.2$]

frequencies. Plateau after a step like increase in the temperature variation of permittivity is a signature of relaxation process [5]. Corresponding to the two plateau regions in figure 6.3, we can notice two thermally activated processes which is depicted in the graph showing variation of dielectric loss tangent with temperature (figure 6.4).

The low temperature relaxation is Maxwell – Wagner type, due to the interfacial polarisation at grain boundaries [6]. This phenomenon is common in heterogeneous system where there is a difference between the grain and grain boundary conductivities. As a result surface charges pile at the interface, giving a Debye like relaxation on application of electric field. The high temperature relaxation is due to charge carrier hopping between Mn^{3+} and Mn^{4+} sites [7, 8]. The variation of dielectric loss tangent with frequency for all the LNMO samples, near the temperature corresponding to relaxation process, is shown in the figure 6.5. From the figure it is clear that as temperature increases the dielectric loss peak is shifted to higher frequencies, which is the correct signature of thermally activated relaxation.

6.3 Cole – Cole plot studies of LNMO

Dielectric spectroscopy (Cole – Cole plot analysis) is an indirect method used for the evaluation of dispersion parameters [9]. In Cole – Cole plot analysis imaginary value of dielectric permittivity is plotted against real permittivity and using non linear least square fitting circular arcs can be completed above real permittivity axis. Dispersion parameters can be evaluated from the fitting parameters. Detailed description of the method was presented in chapter 2. As an initial step we had performed the dielectric spectroscopic studies of cobalt phthalocyanine tetramer and the dispersion parameters were obtained. The temperature variation of those dispersion parameters was reported [10]. In order to study the temperature variation of different dielectric parameters like optical dielectric constant, static

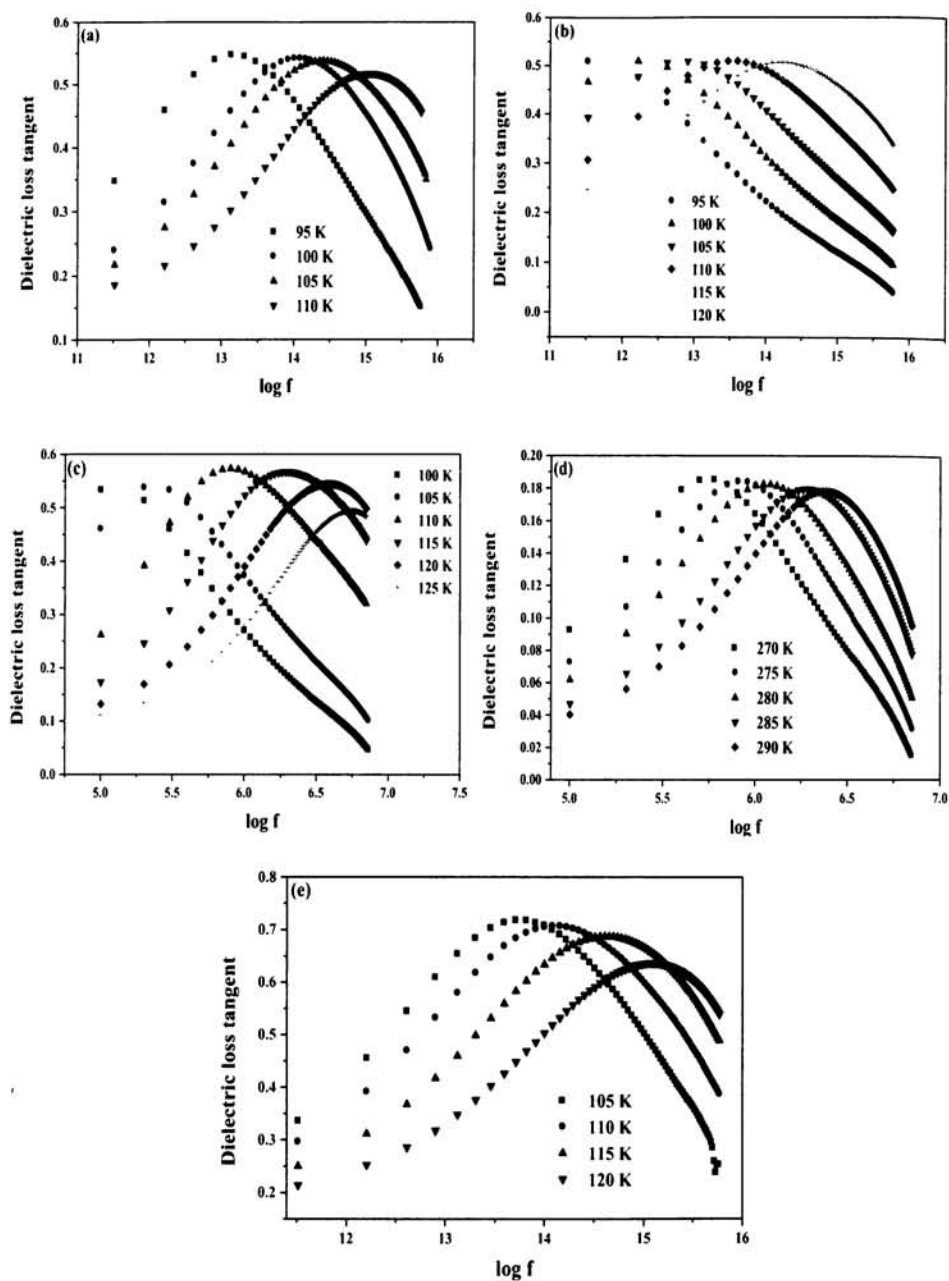


Figure 6.5 The variation of dielectric loss tangent with $\log f$ for the samples $\text{La}_{1-x}\text{Na}_x\text{MnO}_3$ [(a) $x = 0.05$, (b) $x = 0.1$, (c) $x = 0.15$ (low temperature), (d) $x = 0.15$ (high temperature) and (e) $x = 0.2$]

dielectric constant, relaxation time, spreading factor etc. in LNMO sample, Cole – Cole plots were drawn at different temperatures from 100K to 300K at a step of 20 K and are represented in figures 6.6 (a) to 6.6 (d). The circular arcs are drawn from the measured real and imaginary dielectric permittivity using circle least square fitting [11]. The Cole – Cole plots thus obtained for the sample $\text{La}_{1-x}\text{Na}_x\text{MnO}_3$ ($x=0.05, 0.1, 0.15, \text{ and } 0.20$) are shown in the figures 6.6 (a)-6.6 (d). From the figures it is clear that all graphs have the form of circular arcs with centre lying below the real axis, which is an indication of distribution of relaxation time [10]. Clear high frequency portions (left portions) of circular arc appear for the temperatures at around 100K and in the temperature range 200K - 300K. Previously observed relaxation processes are also lying in the same temperature regimes. From figure 6.4, we can see that the dielectric loss peaks are observed at temperature ranges 100K-150K, corresponding to low temperature relaxation and 200K – 300K, corresponding to high temperature relaxation. Also a linear rising tail is observed in the imaginary permittivity versus real graphs for the above mentioned temperatures. More over, if we extrapolate the circular arcs to the real dielectric axis, with out considering the tail, then we will arrive at the dielectric permittivity values corresponding to the two plateaus in the figure 6.3. The tail in the Cole – Cole plot can be tuned by varying the temperature and hence linked with electron conductivity. In disordered system the electrical response can be described by a power law in the ‘Universal Dielectric Response’ (UDR) [7, 8, 12] of the form,

$$\epsilon^*(\omega) \sim A \frac{(j\omega)^{s-1}}{\epsilon_0} \quad (6.3)$$

where A and s are temperature dependent constants, j is the imaginary unit, ω is angular frequency and ϵ_0 is permittivity of free space. The value of s is between 0 and 1. By UDR, equation (6.3) yields a straight line with frequency independent slope of $\tan [(s-1) \pi/2]$. When $s=0$, the slope become infinity and the tail line becomes vertical (in other words tail disappears) and the equation (6.3) shows the

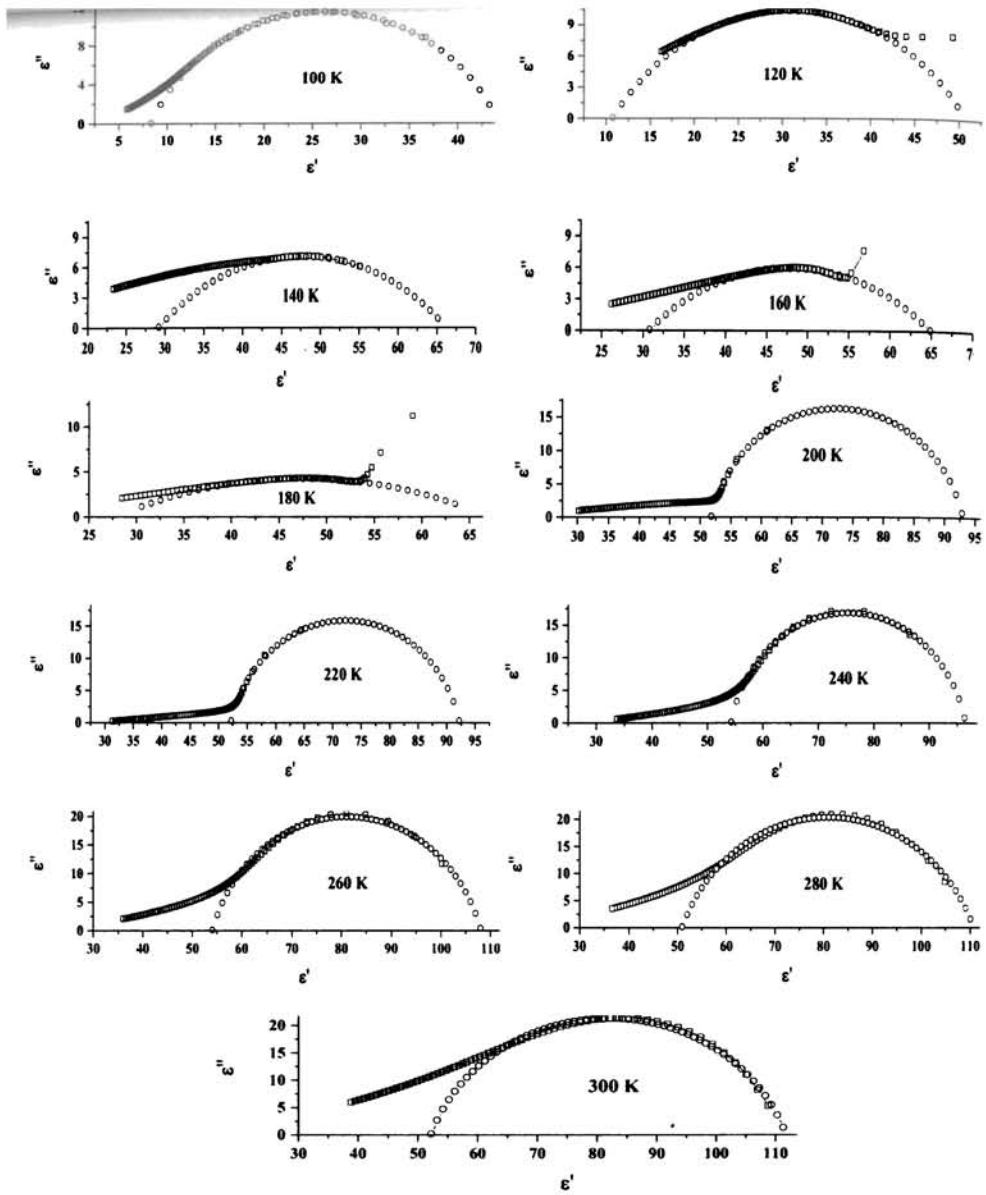


Figure 6.6(a) Cole – Cole plots for the sample $\text{La}_{0.95}\text{Na}_{0.05}\text{MnO}_3$ at different temperatures. Red squares indicate measured data and green indicate fitted data.

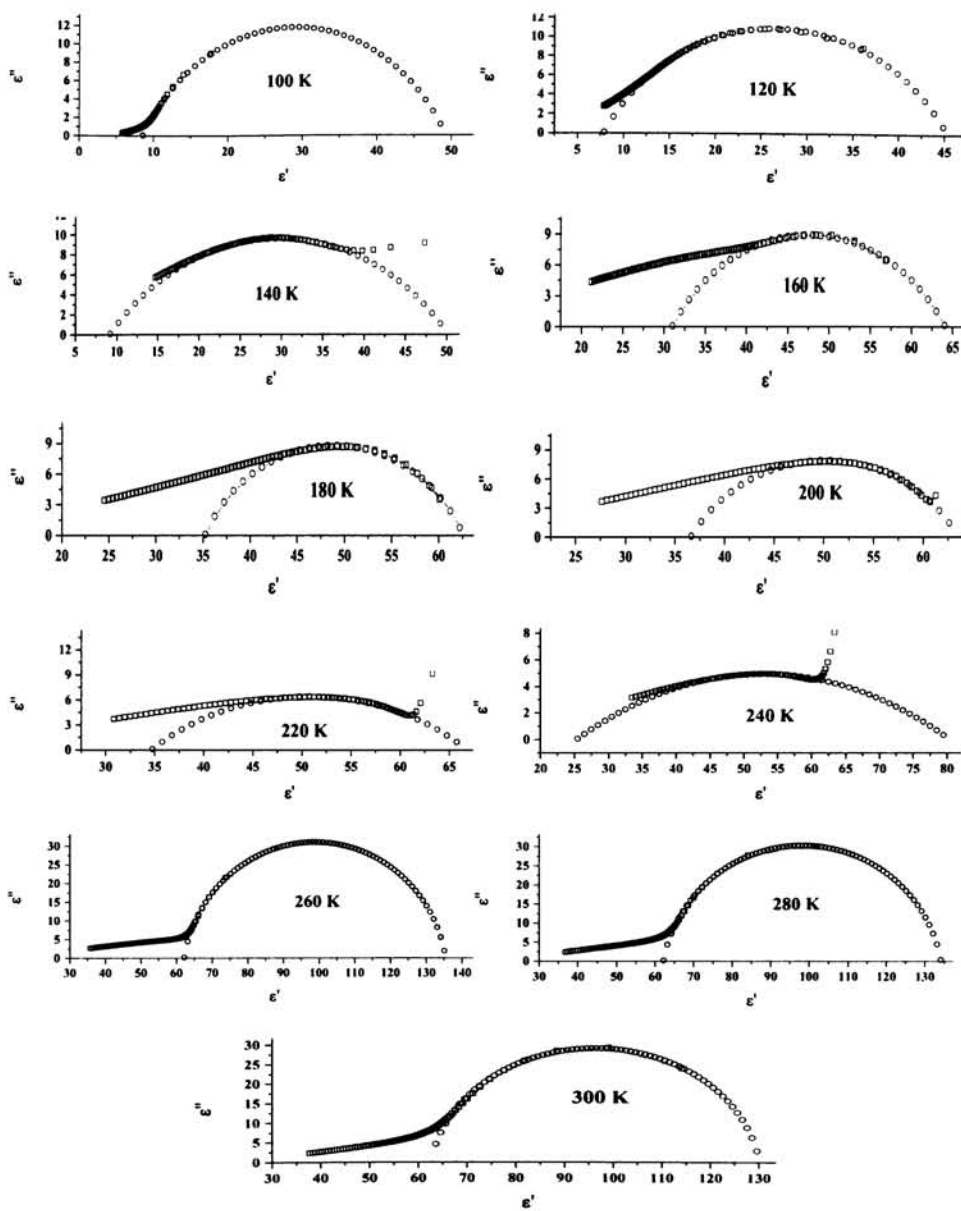


Figure 6.6(b) Cole – Cole plots for the sample $\text{La}_{0.9}\text{Na}_{0.1}\text{MnO}_3$ at different temperatures. Red squares indicate measured data and green indicate fitted data.

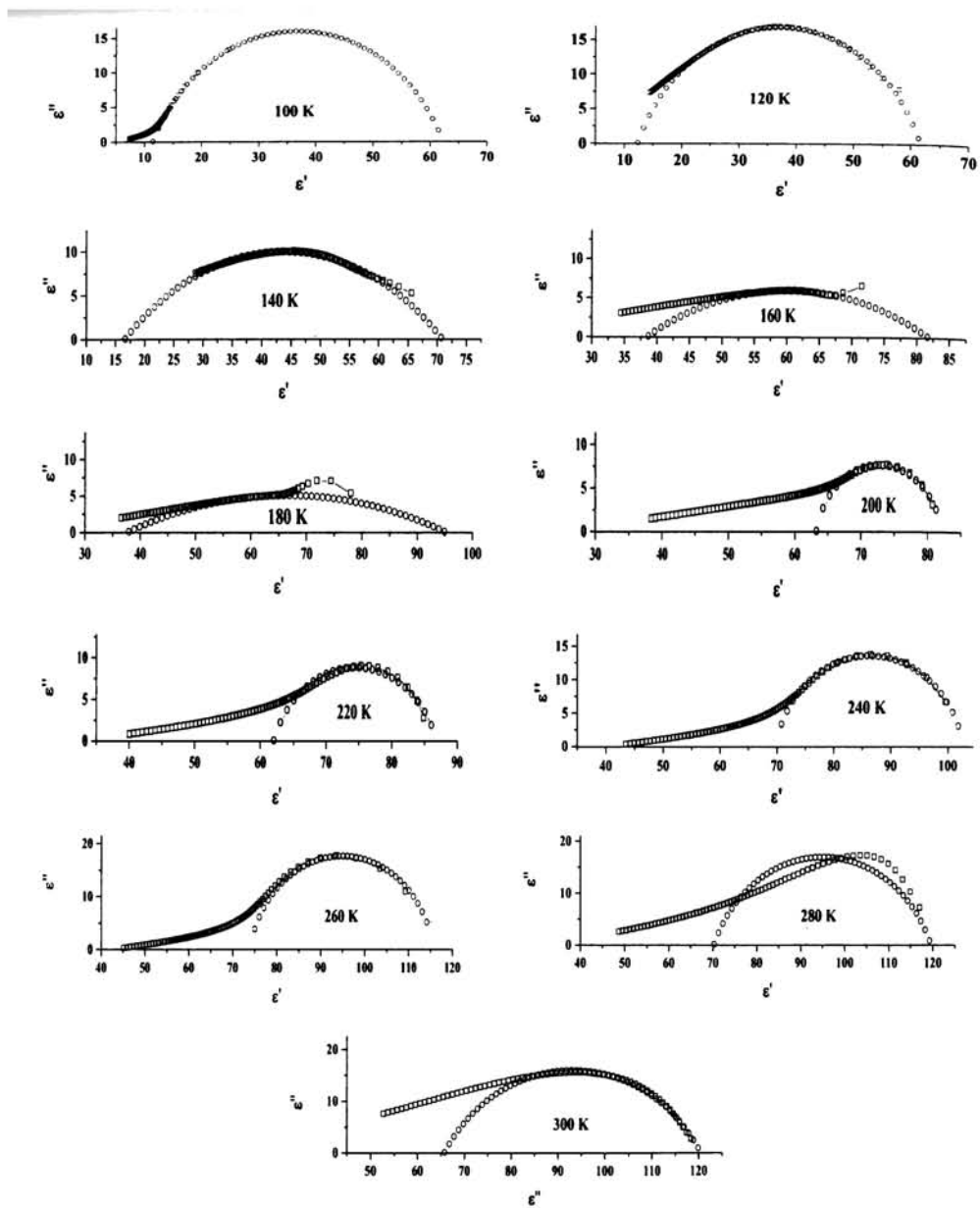


Figure 6.6(c) Cole – Cole plots for the sample $\text{La}_{0.85}\text{Na}_{0.15}\text{MnO}_3$ at different temperatures.

Red squares indicate measured data and green indicate fitted data.

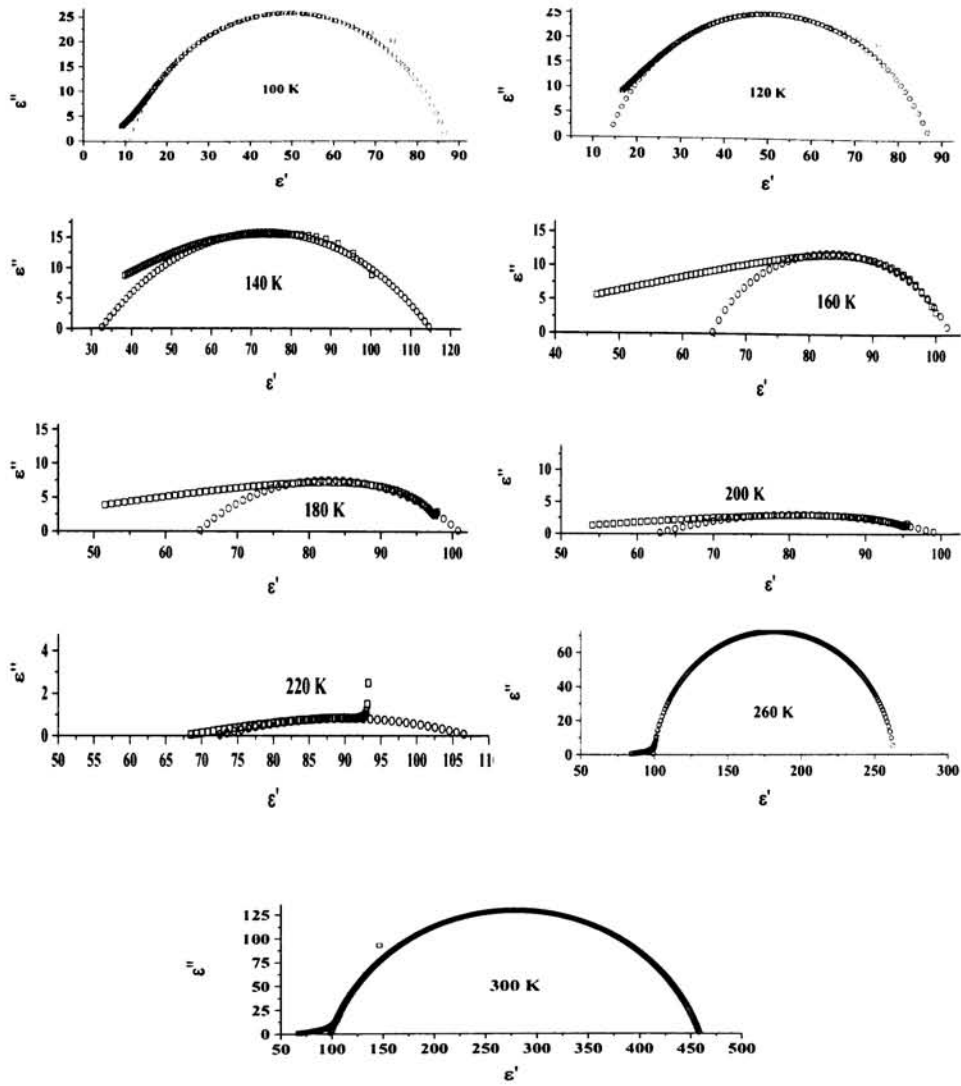


Figure 6.6(d) Cole – Cole plots for the sample $\text{La}_{0.8}\text{Na}_{0.2}\text{MnO}_3$ at different temperatures.

Red squares indicate measured data and green indicate fitted data.

usual reciprocal behaviour. In the relaxation temperature range, Cole – Cole plot shows Debye like behaviour (equation 6.4).

$$\epsilon^* = \epsilon_{\infty} + \frac{\epsilon_s - \epsilon_{\infty}}{1 + (j\omega\tau)^{1-\alpha}} \quad (6.4)$$

All the plots are semicircular arcs with centre lying below the real axis. That is an indication of broadening of relaxation. From Cole – Cole analysis dielectric parameters like static dielectric constant (ϵ_s), optical dielectric constant (ϵ_∞), spreading factor (α), average relaxation time (τ_0) and molecular relaxation time (τ) of the LNMO sample were calculated [10] and are presented in table 1. From the table, it is clear that the temperature variations of dielectric parameters have similar behaviour in the case of all LNMO samples and hence the sample $\text{La}_{0.95}\text{Na}_{0.05}\text{MnO}_3$ is selected as a representative of the series for further discussion. The variation of optical dielectric constant with temperature for the sample $\text{La}_{0.95}\text{Na}_{0.05}\text{MnO}_3$ is shown in figure 6.7(a). The two plateau regions in the figure corresponds to the two thermally activated relaxation mechanism. This is in good agreement with the results obtained from the variation of dielectric permittivity with temperature studies (figure 6.3). The same conclusion is drawn from figure 6.7(b) too, where the variation of static dielectric constant with temperature is depicted.

From the variation of spreading factor (α) with temperature [figure 6.7(c)], it is understood that as temperature increases from 100 K the spreading factor also increases up to 190K. Thereafter a sharp decrease occurs at 200 K and then it again increases. An increase in α is associated with the two relaxation mechanisms. The spreading factor is a measure of distribution of relaxation time. The increase of α with temperature can be easily understood from the bistable model proposed by Frolich [13], according to which there are two equilibrium positions for the dipole. These positions are determined by the minima of the potential well and are separated by the potential hill. If the charged particle possesses enough energy to cross the potential hill, then there is dielectric relaxation which is associated with a single relaxation time [13]. However a molecule in a solid might possess more than two equilibrium positions corresponding to minima of potential energy which are separated by more than

Temperature (K)	x	ϵ_{∞}	ϵ_s	α	$\tau_0(*10^{-7}S)$	$\tau(*10^{-7}S)$
100	0.05	8.32	44.27	0.28	6.22	4.59
	0.1	8.53	49.22	0.32	8.50	6.16
	0.15	11	61.5	0.35	9.34	7.53
	0.2	10.56	87.28	0.25	9.04	7.45
120	0.05	10.82	50.77	0.4	3.30	2.69
	0.1	7.87	45.33	0.33	6.82	4.96
	0.15	12.2	61	0.39	8.12	6.89
	0.2	13.57	87.3	0.27	7.46	6.42
140	0.05	29.2	64.2	0.54	2.97	2.17
	0.1	9.21	50.08	0.37	4.17	3.45
	0.15	16.5	71	0.43	7.12	6.37
	0.2	32.6	114.8	0.35	6.84	4.99
160	0.05	30.55	64.36	0.575	1.09	0.89
	0.1	31.02	64.06	0.44	2.98	2.16
	0.15	38.0	82	0.56	4.56	3.49
	0.2	64.73	102.2	0.50	4.67	4.11
180	0.05	30.85	64.89	0.69	0.65	0.54
	0.1	35.22	62.55	0.52	1.35	1.16
	0.15	38.0	95	0.74	3.65	2.87
	0.2	64.79	100.8	0.54	3.86	3.11
200	0.05	51.84	92.3	0.15	11.60	9.90
	0.1	36.62	63.53	0.76	4.97	4.18
	0.15	64	83	0.17	7.34	6.39
	0.2	63	99.66	0.58	7.18	6.41
220	0.05	52.26	93.1	0.15	8.22	7.01
	0.1	34.75	66.74	0.21	4.67	3.61
	0.15	63	87	0.24	7.54	6.47
	0.2	72.56	107.08	0.19	3.6	3.44
240	0.05	54.11	96.48	0.16	4.55	3.89
	0.1	35.47	80.32	0.27	2.94	2.43
	0.15	70	103	0.29	3.29	2.74
	0.2	71.41	81.92	0.23	2.81	2.43
260	0.05	54.31	108.2	0.19	3.18	2.65
	0.1	62.1	135.45	0.29	1.76	1.44
	0.15	74	115	0.31	2.27	1.89
	0.2	99.22	263.0	0.25	1.46	1.05
280	0.05	51.06	110.67	0.21	1.81	1.49
	0.1	62.19	134.24	0.32	1.14	0.92
	0.15	70	120	0.35	1.56	1.15
	0.2	100.22	294.58	0.32	1.16	0.99
300	0.05	52.34	111.77	0.21	1.13	0.94
	0.1	62.61	130.13	0.33	1.06	0.87
	0.15	65	120	0.37	1.67	1.23
	0.2	99.12	458.2	0.35	1.02	0.84

Table 1 Different dielectric parameters obtained from the Cole- Cole analysis of LNMO samples

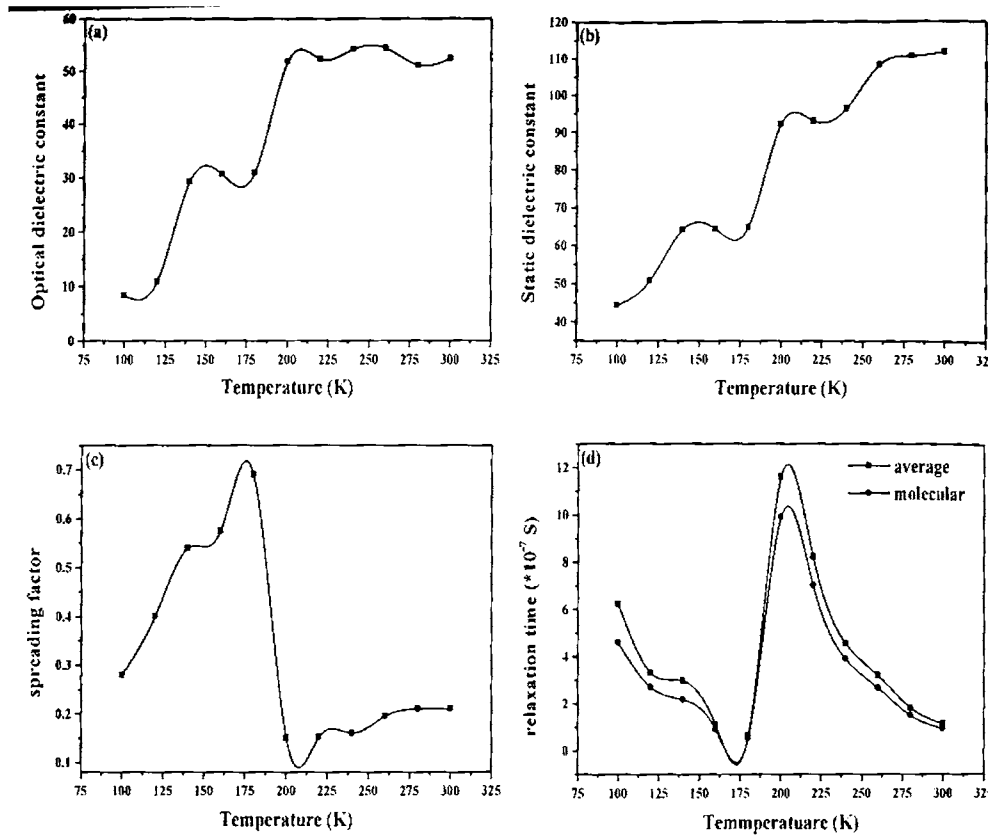


Figure 6.7 The temperature variation of dielectric parameters for the sample $\text{La}_{0.95}\text{Na}_{0.05}\text{MnO}_3$ [(a) optical dielectric constant, (b) static dielectric constant (c) spreading factor, and (d) relaxation time]

one potential hill. A charged particle under activation, while crossing these hills gives rise to multiple relaxation times. In all LNMO samples spreading factor has non zero values and hence we can conclude that there are multiple equilibrium states for the two relaxation process in all LNMO samples. As temperature increases the charged particles gain more and more energy and as a result they cross more potential hills, resulting in the distribution of relaxation times [10]. Hence the spreading factor increases with increase of temperature. The sharp decrease in α between the two relaxation processes might be due to the few

number of equilibrium positions corresponding to relaxation at higher temperature than that at lower temperature.

The temperature variation of average and molecular relaxation time is shown in figure 6.7(d). Since average relaxation time and molecular relaxation time are related by the equation (2.6), they exhibit similar behaviour. As temperature increases, both the relaxation time decrease from initial high values at temperatures 100K and 200K. The former decrease corresponds to low temperature thermally activated relaxation process and latter one corresponds to high temperature thermally activated relaxation process. The decrease of relaxation time with increase of temperature is in accordance with the Debye theory of dipolar orientation [14, 15]. The rise in temperature causes reduction in mean time of stay of ionic dipoles which in turn causes the relaxation time to decrease [16,17]. The large difference between relaxation time for the two thermally activated process may be due to the less number of equilibrium positions for the higher temperature relaxation process.

Considering the compositional dependence, the optical dielectric constant and static dielectric constant increase with increase of Na doping, for almost all temperatures. This can be understood from the fact that hopping polarisation increases with increase of Na concentration. The other three dielectric parameters show an increase up to $x=0.15$ and then decreases in the case of $x=0.2$. Some variations are observed at temperatures between the two relaxation processes, because of the cross over from one Cole-Cole semicircular arc to the other.

Above and below relaxation temperature the dielectric behaviour follows the UDR model. According to equation (6.3), the real and imaginary part of dielectric permittivity can be written as

$$\varepsilon' = \varepsilon_{\infty} + C(T)\omega^{s-1} \quad (6.5)$$

and
$$\varepsilon'' = B(T)\omega^{s-1} \quad (6.6)$$

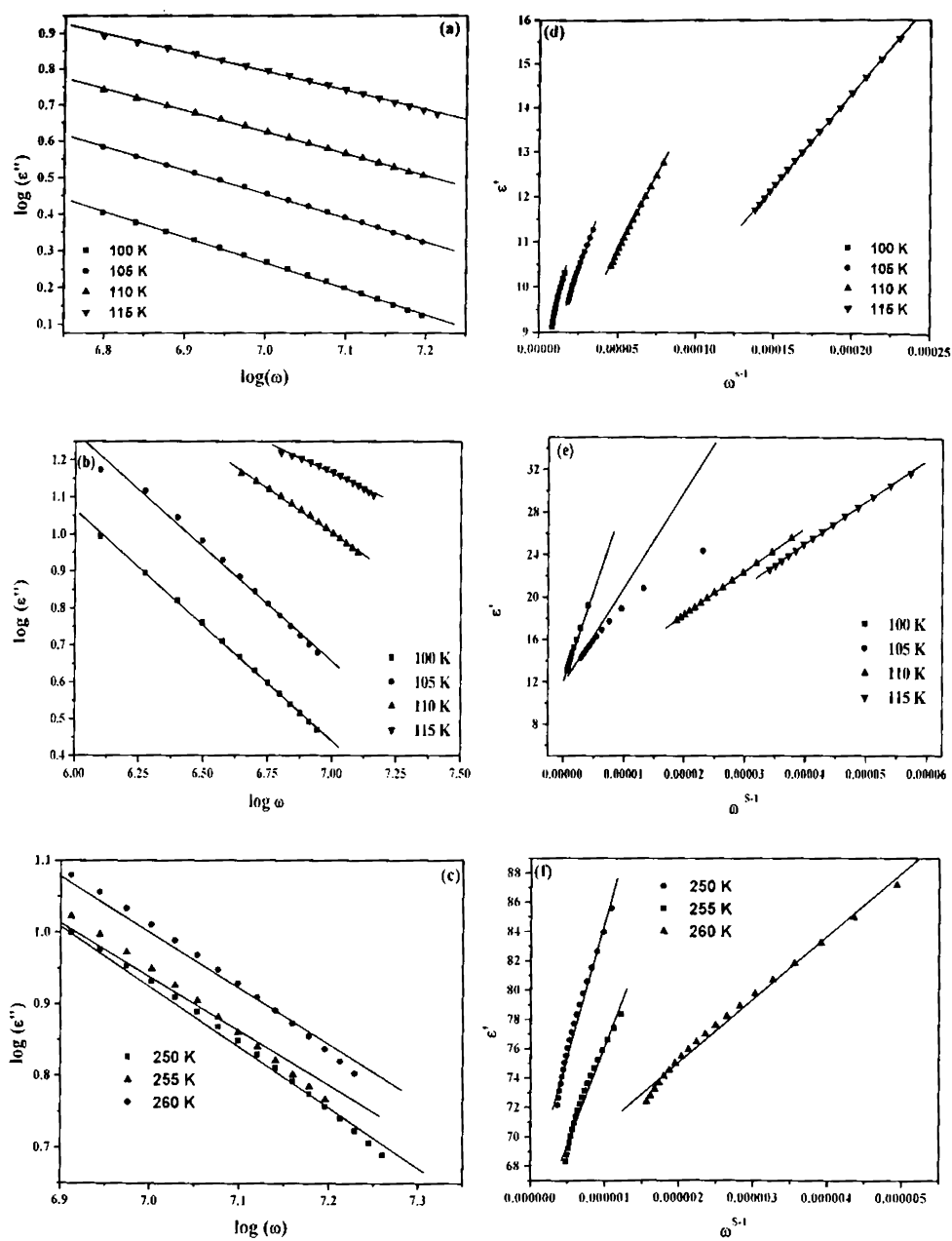


Figure 6.8 Variation of $\log \epsilon''$ with $\log \omega$ for the sample $\text{La}_{1-x}\text{Na}_x\text{MnO}_3$ (a) $x=0.1$ [low T], (b) $x=0.15$ [low T] and (c) $x=0.15$ [high T]; (d) to (f) Variation of ϵ' with ω^{-1} for the sample $\text{La}_{1-x}\text{Na}_x\text{MnO}_3$ (0.1 [low T] and 0.15 [low T & high T])

where $B(T)$ and $C(T)$ are temperature dependent constants [7]. At a constant temperature the graph between $\log \epsilon''$ and $\log \omega$ is a straight line and from the slope the parameter 's' can be calculated. Using that 's' value, another straight line graph can be obtained between ϵ' and ω^{s-1} . The y intercept of that graph will give the optical dielectric constant. The log-log graph between imaginary permittivity and angular frequency for the sample $\text{La}_{1-x}\text{Na}_x\text{MnO}_3$ (0.1 and 0.15) is depicted in the figure 6.8 (a) – (c). All the graphs show straight line behaviour favouring UDR model and from the slopes, 's' values were evaluated. The graph between imaginary permittivity and ω^{s-1} for the same set of samples are shown in figure 6.8 (d) – (f). By extrapolating the straight line graphs to the Y-axis the optical dielectric constants were obtained. The ϵ_∞ values thus obtained are nearly 7 for the sample $\text{La}_{0.9}\text{Na}_{0.1}\text{MnO}_3$ at around 100 K and 11 and 67 for the sample $\text{La}_{0.85}\text{Na}_{0.15}\text{MnO}_3$ at around 100 K and 240 K respectively and these values are in agreement with those obtained from the Cole – Cole plots (the values from Cole – Cole plots are 7, 11.5 and 70 respectively). Thus we can conclude that the material under consideration follows the UDR model.

6.4 Impedance spectroscopic studies of LNMO

The impedance spectroscopic measurements of the LNMO sample were carried out by using the hp 4192A impedance analyzer, by measuring the real value of impedance (Z') and corresponding phase angle ($\tan \theta$) in a frequency range 100 Hz to 6MHz. The imaginary value of the impedance is measured using the equation (6.7).

$$Z'' = Z' * \tan\theta \quad (6.7)$$

The impedance spectrum was obtained by plotting real impedance (Z') against imaginary impedance (Z''). The semicircular arcs obtained were fitted using least square fitting. The impedance spectrum for the sample $\text{La}_{0.9}\text{Na}_{0.1}\text{MnO}_3$ is depicted in the figure 6.9. The impedance spectrum shows single semicircular arcs whose radii decrease with increase in temperature. The single semicircle at all

temperatures indicates the dominance of grain effect rather than the grain boundary and electrode effect [18]. From the intercepts at the right side of the

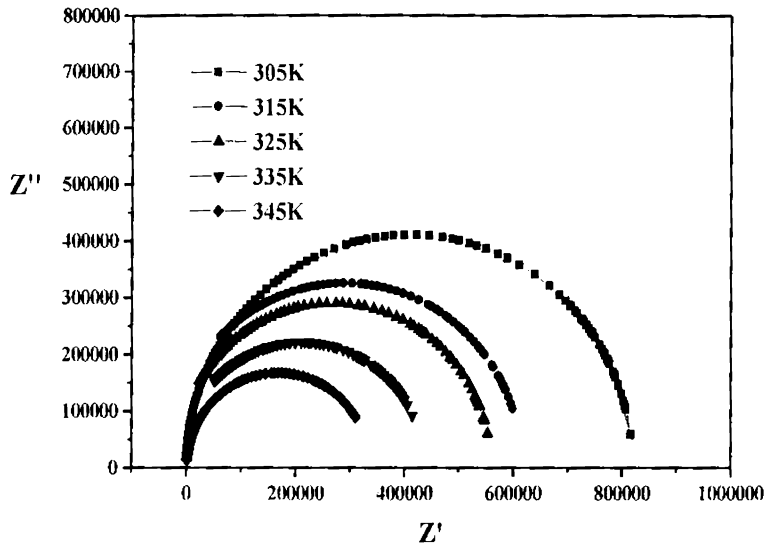


Figure 6.9 Complex Impedance spectrum of the sample $\text{La}_{0.9}\text{Na}_{0.1}\text{MnO}_3$ at different with temperature

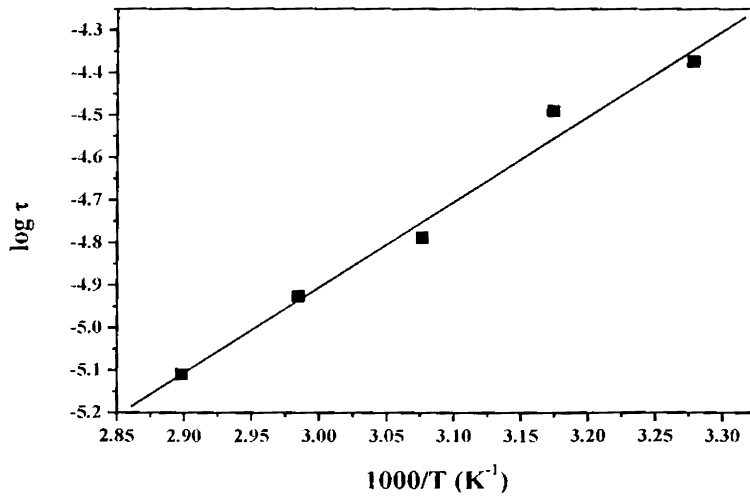


Figure 6.10 Variation of relaxation time temperatures.

semicircular arc with the real axis, we can calculate the values of bulk resistance of the material (grain resistance). From the frequency at which Z'' becomes maximum we can calculate the bulk capacitance using the equation (6.8).

$$2\pi f_{max} = \frac{1}{R_b C_b} \quad (6.8)$$

The relaxation time can be calculated from impedance diagram (or from variation of Z'' with frequency) using the relation (6.9).

$$2\pi f_{max} = \frac{1}{\tau} \quad (6.9)$$

The calculated values of R_b , C_b and τ were given in table 2. From the table it is clear that as temperature increases the bulk resistance, bulk capacitance and relaxation time decreases. The decrease in R_b is due to the increase in hopping conductivity of the sample with increase in temperature. The decrease of relaxation time with temperature indicates the typical semiconductor behaviour of the material [19]. The activation energy for conduction for the material can be calculated using Arrhenius equation [equation (6.10)].

$$\tau = \tau_0 \exp (E_A / k_B T) \quad (6.10)$$

where τ_0 is the pre exponential factor, k_B is Boltzmann's constant, E_a is the activation energy and T is absolute temperature. The variation of relaxation time with $1000/T$ is shown in the figure 6.10. From the slope of the graph it is found that the activation energy is 0.173 eV.

Temperature (K)	R_b (K Ω)	C_b (pF)	τ ($\times 10^{-5}$ S)
305	824.5	51.7	4.22
315	621.8	51.1	3.22
325	564.5	28.6	1.62
335	426.8	27.6	1.18

Table 2 The calculated values of R_b , C_b and τ

6.5 Dielectric and impedance studies of charge ordered LNMO

The charge ordered LNMO sample ($\text{La}_{0.75}\text{Na}_{0.25}\text{MnO}_3$) is prepared using the citrate gel method. The dielectric permittivity measurements were carried out on these samples, using the hp 4285 A impedance analyzer as explained in the section 6.2 of this chapter. The frequency variation of permittivity along with temperature variation is shown in figure 6.11. The frequency variation is exactly identical to that in the case of other non charge ordered LNMO samples. A broad dielectric maxima around 230 K as in the case of charge ordered GSMO samples can be seen here. The relaxor ferroelectric behaviour is due to the charge ordering in this particular composition [20]. The frequency and temperature variation of loss tangent is presented in the figure 6.12. The frequency variation mimic the behaviour of charge ordered GSMO samples; but the temperature variation does not exhibit loss tangent peak. Due to the shifting of loss tangent peak from dielectric peak as observed in the case of GSMO, the peak could be outside the temperature region. The figure 6.13 represents the frequency and temperature variations of dielectric loss which shows the same behaviour as that of loss tangent.

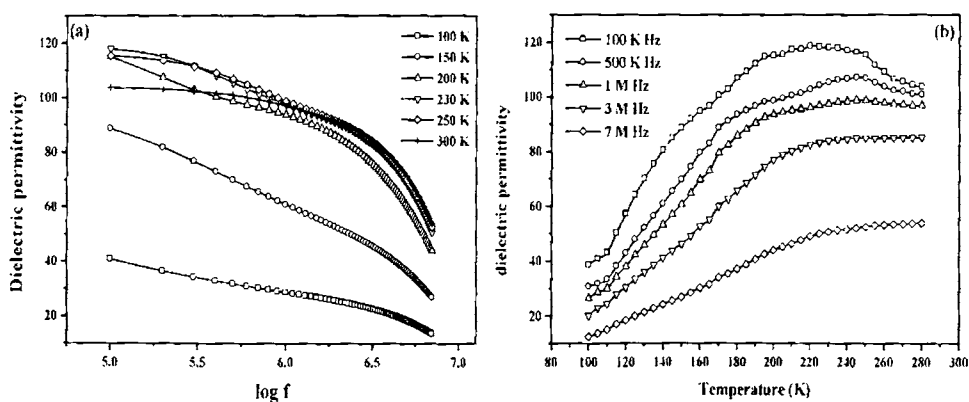


Figure 6.11 (a) Frequency variation and (b) Temperature variation of dielectric permittivity of $\text{La}_{0.75}\text{Na}_{0.25}\text{MnO}_3$

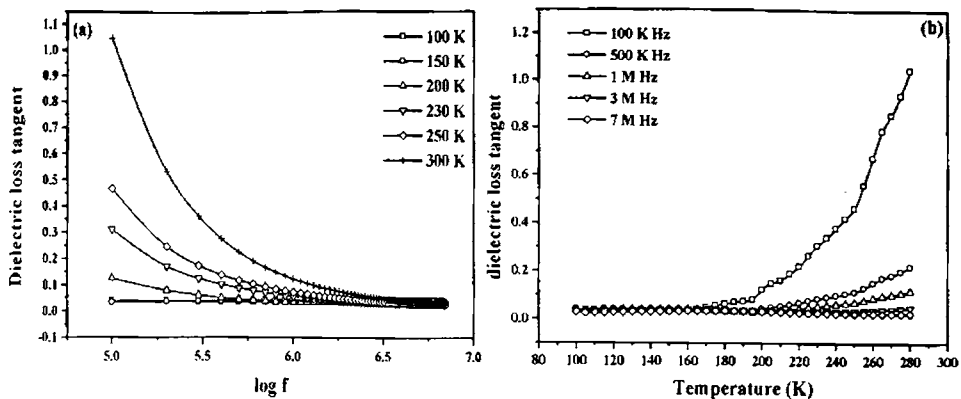


Figure 6.12 (a) Frequency variation and (b) Temperature variation of dielectric loss tangent of $\text{La}_{0.75}\text{Na}_{0.25}\text{MnO}_3$

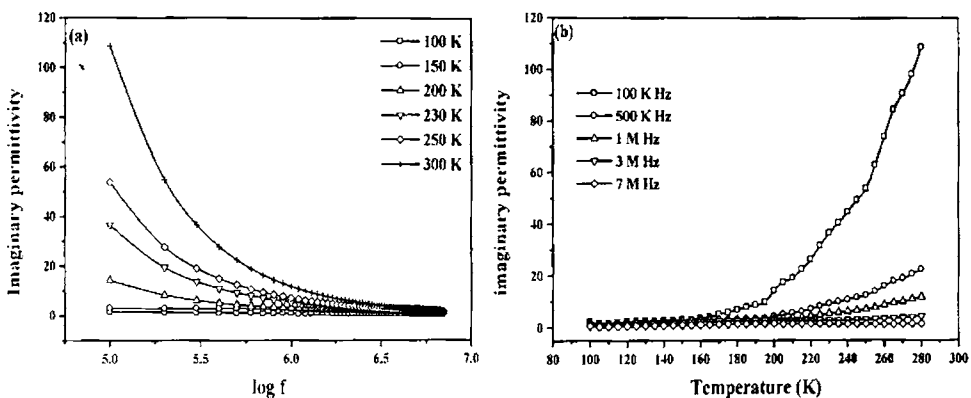


Figure 6.13 (a) Frequency variation and (b) Temperature variation of dielectric loss of $\text{La}_{0.75}\text{Na}_{0.25}\text{MnO}_3$

6.6 Conclusion

The frequency and temperature dependence of the dielectric parameters of the nano sized Na doped Lanthanum manganites, prepared by the citrate gel technique, were studied. The frequency dispersion of dielectric parameters can be explained by using Maxwell-Wagner interfacial polarisation. The temperature dependence of dielectric parameters indicates the presence of two thermally

activated relaxation mechanisms; low temperature relaxation attributed to interfacial polarisation between grain boundaries and high temperature relaxation due to hopping of charge carriers between Mn ions. The shifting of dielectric loss tangent peak to higher frequencies with increase of temperature confirms the two relaxation mechanisms. The dispersion parameters of the LNMO sample were evaluated by using dielectric spectroscopy. All the Cole – Cole plots are semicircular arcs with the centre lying below the real axis, which is an indication of distribution of relaxation times. The temperature variations of optical and static dielectric constants exhibit two plateau regions, corresponding to two thermally activated relaxation mechanisms. The variation of spreading factor with temperature reveals the existence multiple equilibrium states for the sample in the case of both thermally activated relaxation process. The temperature variations of both molecular and average relaxation time are explained by Debye theory of dipolar orientation. The variation of dispersion parameters with doping is attributed to the hopping polarisation. The linear rising tail in the Cole – Cole plot is an indication that LNMO sample obeys ‘Universal Dielectric Response’ (UDR) model. Applying UDR model, in the frequency variation of dielectric permittivity and dielectric loss, the optical dielectric constant values of the sample could be obtained which is in good agreement with those obtained by dielectric spectroscopy. The temperature variation of charge ordered LNMO sample is a signature of multiferroism and it is an indication of role of charge ordering in the ferroelectric property of manganites.

References

- [1] Mohammed E. M, Anantharaman M. R, *J. Instrum. Soc. India* **32**(3) (2002) 165.
- [2] Kwan Chi Kao, *Dielectric Phenomena in Solids*, Elsevier Academic Press, London (2004).
- [3] Koopes C. G, *Phys. Rev* **83**(1) (1951).
- [4] Wagner K. W, *Ann. Phys.* **40** (1993) 817.
- [5] Shanming Ke, Huiqing Fan and Haitao Huang, *J Electroceram* **22** (2009) 252.
- [6] Prabhakar Singh, Devendra Kumar and Om Prakash, *J. Appl. Phys.* **97** (2005) 074103.
- [7] Wang C. C and Zhang L. W, *J. Phys. D: Appl. Phys.* **40** (2007) 6834.
- [8] Thevanayagam S, *J. Appl. Phys.* **82** (1997) 2538.
- [9] Cole K. S and Cole R. H, *J. Chem. Phys.* **9** (1941) 34.
- [10] Sagar S, Saravanan S, Suresh Kumar S, Venkatachalam S and Anantharaman M. R, *J. Phys.D: Appl. Phys.* **39** (2006) 1678.
- [11] Razet A, *Metrologia* **35** (1998) 143.
- [12] Jonscher A. K, *Dielectric Relaxation in Solids*, Chelsea Dielectrics Press, London (1983).
- [13] Daniel V. V, *Dielectric Relaxation*, Academic, London (1967).
- [14] Saravanan S, Joseph Mathai C, Anantharaman M. R, Venkatachalam S and Prabhakaran P. V, *J. Appl. Polym. Sci.* (2004) **91** 2529.
- [15] Nisha J. Tharayil, Sagar S, Raveendran R and Vaidyan A. V, *Physica B: Condensed Matter* **399** (2007) 1-8.
- [16] Hill N. E, Vaughan W. E, Price A. H and Davies M, *Dielectric Properties and Molecular Behaviour*, Van Nostrand-Reinhold, London (1969).
- [17] Das B. P, Choudhary R. N. P and Mahapatra P. K, *Indian Journal of Engineering and Material Science* **15** (2008) 152.
- [18] Currie J. R, Batra A. K, Alim M. A, Aggarwal M. D and Lal R. B, *J Mater Sci. Mater Electron* **18** (2007) 433.

- [19] Ranga Raju M. R and Choudhary R. N. P, *Indian Journal of Engineering and Materials Sciences* **15** (2008) 137.
- [20] Sagar S, Joy P. A and Anantharaman M. R, *Ferroelectrics* **392** (2009) 13.

Chapter 7

On the Colossal Thermoelectric Power of Charge Ordered Manganites

7.1 Introduction

Thermoelectric effect is the generation of an electric field due to a thermal gradient, and the rate of change of thermoelectric voltage with temperature is called the thermoelectric power or Seebeck coefficient. Possible applications of thermoelectric materials are in eco-friendly refrigeration and in electrical power generation [1-4]. The efficiency of a thermoelectric conversion is determined by the figure of merit Z which can be written in the form $Z = Q^2\sigma/K$, where Q is the Seebeck coefficient, σ is the electrical conductivity and K is the thermal conductivity. Accordingly, large Seebeck coefficient, high electrical conductivity and low thermal conductivity are prerequisites for materials with potential for applications. Metals are poor thermoelectric materials because they possess small values of Seebeck coefficient. Insulators display large values of Seebeck coefficient, but are poor electrical conductors and are not in demand. However semiconductors with an electron density of $\sim 10^{19}/\text{cm}^3$ are considered as ideal thermoelectric materials [3].

Abraham Ioffe in 1956 theoretically predicted that doped semiconductors could exhibit a much larger value of Seebeck coefficient. Eventually this led to the discovery of a large thermoelectric power for binary semiconductors of the form Bi_2Te_3 at room temperature [5, 6, 7]. Normal broad band semiconductors, rattling semiconductors with skutterudite crystal structure, correlated metals and semiconductors, Kondo insulators and semiconductor quantum wells were also found to be promising thermoelectric materials [3, 4, 8]. Large value of thermoelectric power of the order of 10 mV/K at ~ 20 K was exhibited by pure germanium single crystals [9, 10].

A survey of literature reveals that SrTiO₃, a metal oxide with cubic perovskite structure, is a good thermoelectric material [2, 11, 12], while rare earth inter-metallic compounds, whose 4f levels are close to the Fermi energy and by virtue of their high density of states near the Fermi energy, scatter most of the conduction electrons, are also considered to be good thermoelectric materials. Therefore, materials, with large number of atoms per unit cell, large average atomic mass and large coordination number per unit atom, are likely to display large thermoelectric power [3]. It is seen from literature that the Seebeck coefficient of manganites is routinely investigated to explain the transport properties of manganites and not much attention is paid to the fact that such materials can be potential thermoelectric materials with colossal Seebeck coefficient. Maignan *et al.* [13] reported that perovskite manganite is a potential material for thermoelectric applications. High bandwidth manganites like La_{1-x}Sr_xMnO₃, though they possess large value of electrical conductivity, display very small values of Seebeck coefficient. However, low and intermediate band width manganites can be materials with potential for displaying a large Seebeck coefficient. Charge ordering has a crucial role in the display of large thermoelectric power and hence measurements of thermoelectric power on charge ordered manganites Gd_{1-x}Sr_xMnO₃ (x=0.3, x=0.4 and x=0.5) and La_{0.75}Na_{0.25}MnO₃ were conducted expecting huge value of Seebeck coefficient. The thermoelectric studies of other non charge ordered Na doped manganites La_{1-x}Na_xMnO₃ (x=0.05, 0.1, 0.15 and 0.2) were also conducted to verify the conduction mechanism in the insulating phase of these manganites. The results of those thermoelectric power studies are presented in this chapter.

7.2 Thermoelectric power studies of GSMO and LNMO samples

The thermoelectric power of GSMO [Gd_{1-x}Sr_xMnO₃ (x=0.3, x=0.4 and x=0.5)] and LNMO samples [La_{1-x}Na_xMnO₃ (x=0.05, 0.1, 0.15, 0.2 and 0.25)] were determined by employing a DC differential technique (which is described in

detail in chapter 2) in the temperature range of 5 K - 300 K using a home made set up at IUC-DAEF, Indore, India.

7.2.1 Colossal thermoelectric power exhibited by charge ordered GSMO and LNMO manganites

The temperature variation of thermoelectric power for the GSMO samples is presented in figure 7.1. The Seebeck coefficient is negative at room temperature and as the temperature decreases, this value decreases and then a cross over from negative to positive value occurs at around 70 K. The thermoelectric power sign crossover from negative to positive (as shown in the inset of fig. 2) can be understood if one considers the conduction mechanism in semiconductors. The Seebeck coefficient of a typical semiconductor can be written in the form

$$Q = -\frac{k_B}{e} \left(\frac{\Delta}{k_B T} + B \right) \quad (7.1)$$

Here Δ is the activation energy which is positive for electrons and negative for holes. B is a constant which is related to the entropy of the carriers [14, 15]. Thus it is evident that at temperatures below 70 K, the predominant carriers are holes. It can also be seen that at very low temperatures there is a sharp increase in the thermoelectric power whose onset is at around 70K and a peak is observed at ~ 40K. At this temperature, $\text{Gd}_{0.5}\text{Sr}_{0.5}\text{MnO}_3$ exhibits a colossal thermoelectric power of 35 mV/K. For the other two compositions the colossal values are 30 mV/K and 20 mV/K respectively for $x=0.4$ and $x=0.3$. After attaining the peak value it decreases with temperature. Coincidentally this is the largest value of thermoelectric power ever reported for these class of materials at this temperature. Colossal thermoelectric power was previously reported for strongly correlated semiconducting FeSb_2 single crystals and reduced TiO_2 single crystals [8, 16].

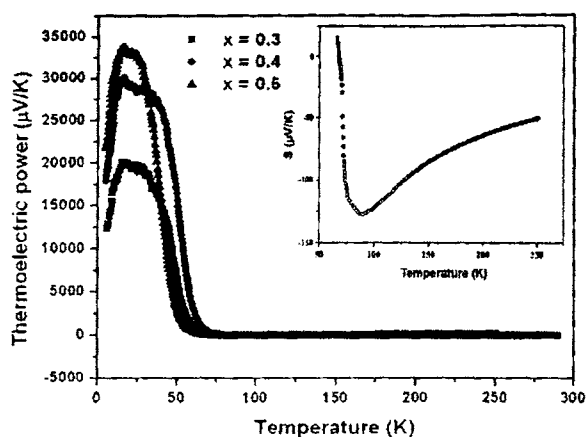


Figure 7.1 Temperature Variation of Seebeck coefficient for the sample $Gd_{1-x}Sr_xMnO_3$ [(a) $x=0.3$, (b) $x=0.4$ and (c) $x=0.5$]. Inset shows the zero crossing over of Seebeck coefficient.

The physical origin of such a phenomenon in manganites could be because of various factors. Of the many attributes leading to the exhibition of colossal thermoelectric power namely, phonon drag, magnon drag, charge ordering, spin glass cluster or spin fluctuation, could be contributing individually or collectively to this phenomenon. The main contributions of thermo electric power can be from phonon drag, diffusion of electrons and magnon drag. When there exists a temperature gradient, heat flows from a high temperature region to a low temperature region. Heat flow can be considered as a flow of phonons. During the transport they get scattered with electrons and transfer its momentum to the electrons. Thus the temperature gradient creates an electron drag and consequently a potential difference is produced. This is the phonon drag contribution to the thermo electric power. For pure substances the phonon drag contribution occurs at temperatures less than the Debye temperature.

Due to difference in charge carrier concentrations in the metals of a thermocouple, there is diffusion of charge carriers from one metal to another metal at the two junctions. But the difference in temperature in a thermo couple at the

junctions results in different diffusion rates of charge carriers and consequently leads to thermo electric power. This is the diffusion contribution of thermopower. Magnons are quanta of spin waves and in a ferromagnetic material at absolute zero there is perfect alignment of spins. But as temperature increases the spins start to misalign. This is where a spin wave is formed. Those spin waves are quantized and each quantum is called a magnon. At absolute zero the material can be considered as vacuum and at higher temperature it can be considered as a system of quasi particles called magnons. When a ferromagnetic material undergoes phase transition there will be magnon flow from higher temperature to lower temperature and some of them will get scattered by the electrons and thus magnon momentum is transferred to the electrons. This magnon drag leads to thermo electric power. It was reported that in the case of single crystal TiO_2 , phonon drag effect of holes contribute to the large positive thermoelectric power [16].

From temperature dependent magnetisation curves (figure 3.8) it is evident that a paramagnetic to spin glass like transition occurs for the sample under discussion at low temperatures. It is noteworthy that colossal thermoelectric power of ~ 35 mV/K was displayed at this temperature for the sample $\text{Gd}_{1-x}\text{Sr}_x\text{MnO}_3$ ($x=0.3, 0.4$ and 0.5). However, studies by other researchers indicate that charge ordering takes place in $\text{Gd}_{0.5}\text{Sr}_{0.5}\text{MnO}_3$ at temperatures $< 90\text{K}$ [17, 18]. Recently, Rhyee *et al.* [19] reported a large figure of merit (~ 1.48) in $\text{In}_4\text{Se}_{3.6}$ crystals where in charge density wave instability was attributed to the large anisotropy observed in electric and thermal transport properties. This result suggests that one cannot rule out the contributions of charge ordering to the colossal thermopower. The suggested mechanism is rather tentative and further studies are in progress so as to understand the underlying physics involved in the display of colossal thermoelectric power in these class of compounds. The low temperature thermo electric power peak can be explained from the electron

phonon interaction theory [9]. Considering the electron-phonon interaction of semiconductors the thermoelectric power may be derived as

$$Q = -\frac{1}{e} \left(\frac{K_2}{K_1 T} - \frac{\zeta}{T} + \frac{K'}{K_1} \right) \quad (7.2)$$

where K_1 , K_2 and K' are functions of distribution function and electron and phonon mean free path and ζ is the chemical potential. The first term is a constant and the temperature dependence of second term is very small. The third term can be evaluated as

$$\frac{K'}{K_1} = \frac{3}{4} \pi^{\frac{1}{2}} \frac{l_{ph}}{l_{ep}} \left(\frac{2ms^2}{k_B T} \right)^{\frac{1}{2}} k_B \quad (7.3)$$

where l_{ph} is the mean free path in phonon-phonon interaction and l_{ep} is that in electron – phonon interaction. Thus the thermoelectric power is directly proportional to the ratio of mean free paths of phonon- phonon interaction and electron – phonon interaction. At around 100K the phonon mean free path l_{ph} is larger than the electron free path l_{ep} and when temperature lowers l_{ph} rises more rapidly than l_{ep} . Thus K'/K_1 increases with decrease of temperature and hence thermoelectric power increases. But at very low temperature boundary scattering will become predominant and the phonon mean free path for this scattering is a constant of the order of crystallite size. On the other hand the electron mean free path increases with decrease of temperature. Thus at very low temperature, thermo electric power decreases with decrease of temperature.

In the case of charge ordered intermediate bandwidth manganite $\text{La}_{0.75}\text{Na}_{0.25}\text{MnO}_3$, the temperature variation of thermoelectric power is shown in

the figure 7.2. The Seebeck coefficient has positive value at room temperature. As temperature decreases the positive value increases, attains a maximum value and then decreases. After that it becomes negative. At low temperature there is a dramatic increase of negative value of thermo electric power and at 60K it becomes a colossal value of about 80mV/K, the highest Seebeck Coefficient ever reported. The crossing over from positive to negative is clear from the inset of figure 7.2 and can be explained using the equation 7.1. From the temperature variation of magnetisation in the case of $\text{La}_{0.75}\text{Na}_{0.25}\text{MnO}_3$ [figure 4.9(b) in section 4.3.2], it is clear that there is a magnetic transition from paramagnetic state to spin glass like state, as in the case of charge ordered GSMO sample, at around 60K. The temperature coincidence of colossal value of Seebeck coefficient and magnetic transition points to the role of spin fluctuation caused by magnetic transition.

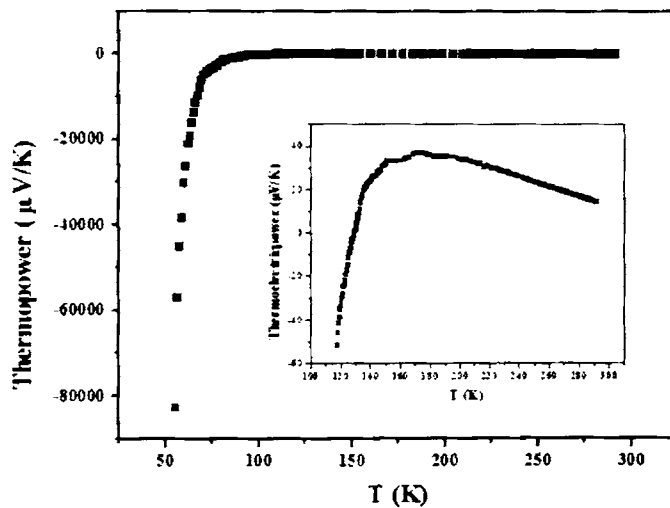


Figure 7.2 Temperature Variation of Seebeck coefficient for the sample $\text{La}_{0.75}\text{Na}_{0.25}\text{MnO}_3$.

Inset shows the zero crossing over of Seebeck coefficient.

7.2.2 Thermoelectric power in non charge ordered LNMO

The variation of thermoelectric power (Seebeck coefficient) of manganites $\text{La}_{1-x}\text{Na}_x\text{MnO}_3$ ($x = 0.05, 0.1, 0.15$ and 0.2) with temperature in the temperature range $5\text{K} - 300\text{K}$ is shown in figure 7.3. All the samples except $x = 0.2$, the thermo electric power value changes from negative to positive. In the case of sample with composition $x = 0.2$, the value remains positive through out the temperature range of investigation. The change in sign in the Seebeck coefficient indicates the coexistence of two types of carriers. The negative S at high temperature is due to electrons which are excited from the valence band (VB) into conduction band (CB). Because of the higher mobility of electrons with in the CB, S is negative. At low temperatures, the electrons in the VB are excited into the impurity band which generates hole like carriers, which are responsible for a positive thermoelectric power [20].

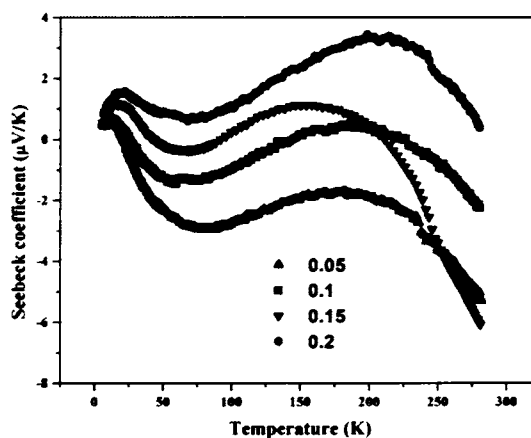


Figure 7.3 Variation of thermoelectric power with temperature for the samples

$\text{La}_{1-x}\text{Na}_x\text{MnO}_3$ [$x=0.05, x=0.1, x=0.15$ and (d) $x=0.2$]

From figure 7.3, it is clear that the value of thermoelectric power changes from negative value and finally becomes positive with increase in Na concentration. It is due to the fact that for every Na doping, double amount of holes are created in the e_g band and thus causes narrowing of e_g band and

distortion of Fermi surface. In addition to a peak in the higher temperature region all the samples exhibit another peak in the lower temperature region. The high temperature peak is a general one for all manganites, which is due to metal insulator transition [21]. The low temperature peak may be due to either phonon drag contribution or magnon drag contribution.

7.2.2.1 Low temperature thermoelectric behaviour

The general relation for thermoelectric power of transitional metal oxides is of the form [22]

$$S = S_0 + S_{3/2}T^{3/2} + S_4T^4 \quad (7.4)$$

where S_0 is a constant which accounts the low temperature variation of thermo electric power, the second term ($S_{3/2} T^{3/2}$) is due to the magnon scattering process and the third term (S_4T^4) is attributed to the spin wave fluctuations in the ferromagnetic phase. In the case of manganites $\text{La}_{1-x}\text{Na}_x\text{MnO}_3$ ($x = 0.05, 0.1, 0.15$ and 0.2), the low temperature data could not be fitted well with the above equation. Considering the diffusion and phonon drag contribution we can use a more general equation for thermopower of the form [23],

$$S = S_0 + S_1 T + S_{3/2}T^{3/2} + S_3 T^3 + S_4T^4 \quad (7.5)$$

where S_1T term is due to diffusion and S_3T^3 term is due to phonon drag. But we could not fit the low temperature data perfectly with the above equation, especially the low temperature peak and above 170K (figure 7.4). From the section 4.3.4, the low temperature resistivity data fitting need a $T^{1/2}$ term. Hence we assume the contribution of thermo power from a $T^{1/2}$ term and then the corresponding equation is given as equation (7.6). Surprisingly the thermoelectric power data perfectly fit with this equation. The fitting is shown in the figure 7.5. The $T^{1/2}$ term contribution to thermoelectric power may be due to weak localisation.

$$S = S_0 + S_{1/2}T^{1/2} + S_1 T + S_{3/2}T^{3/2} + S_3 T^3 + S_4T^4 \quad (7.6)$$

The corresponding fitting parameters are given in the table.1. A general decrease in the fitting parameters indicates the decrease of different contributions to low temperature thermoelectric power of LNMO manganites.

x	S ₀ (μV/K)	S _{1/2} (μV/K ^{3/2})	S ₁ (μV/K ²)	S _{3/2} (μV/K ^{5/2})	S ₃ (μV/K ⁴)	S ₄ (μV/K ⁵)
0.05	-6.12243	5.25193	-1.25213	0.08702	-0.00001	2.7633E-8
0.1	-5.25262	4.37895	-1.0155	0.07095	-0.00001	2.1755E-8
0.15	-5.32701	4.63524	-1.04533	0.07307	-0.00001	2.078E-8
0.2	-5.01945	3.85564	-0.73768	0.0452	-4.4613E-6	5.6772E-9

Table 1. The best fit parameters from TEP data of La_xNa_xMnO₃ (x = 0.05, 0.1, 0.15 and 0.2)

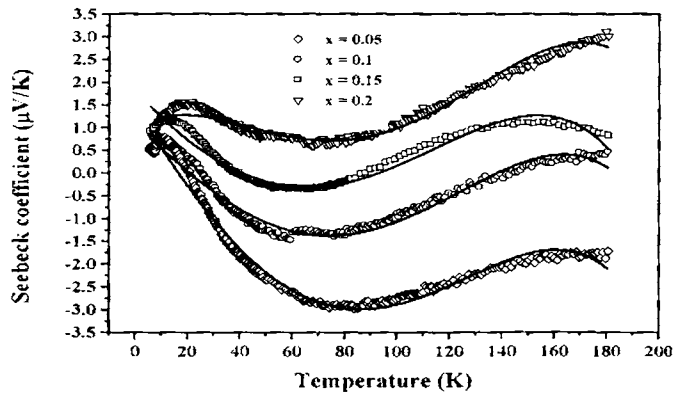


Figure 7.4 Temperature variation of thermoelectric power for the sample La_{1-x}Na_xMnO₃ (x = 0.05, 0.1, 0.15 and 0.2) below 180K. The solid line represents the fitting with equation (7.5).

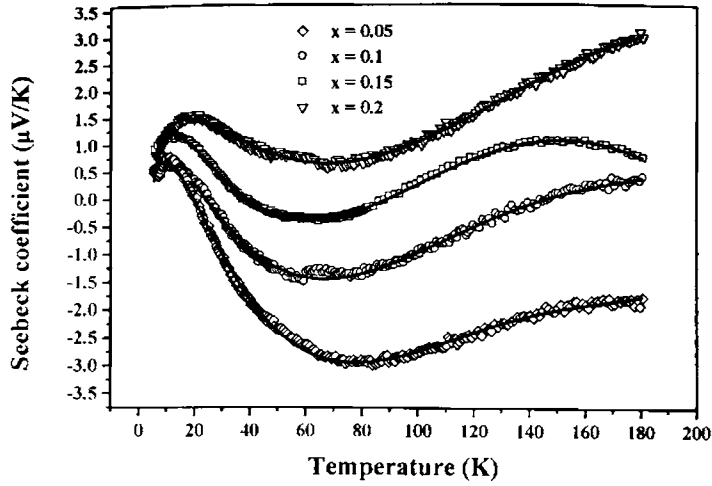


Figure 7.5 Temperature variation of thermoelectric power for the sample $\text{La}_{1-x}\text{Na}_x\text{MnO}_3$ ($x = 0.05, 0.1, 0.15$ and 0.2) below 180K. The solid line represents the fitting with equation (7.6).

7.2.2.2 High temperature behaviour

In the high temperature regime, thermo electric power can be expressed by the Mott's well known equation based on Polaron hopping.

$$S = k_B/e \left[\frac{E_S}{k_B T} + \alpha' \right] \quad (7.7)$$

where ' E_S ' is the activation energy obtained from the TEP data, ' k_B ' is Boltzmann's constant, ' e ' is electronic charge, ' T ' is absolute temperature and ' α' ' is a constant of proportionality between the heat transfer and the kinetic energy of an electron. $\alpha' < 1$ suggests hopping due to small polarons and $\alpha' > 2$ suggests the existence of large polarons [24]. The equation (7.7) is a straight line equation with slope E_S/e and y intercept $k_B \cdot \alpha'/e$. Figure 7.6 give the graph between Seebeck coefficient ' S ' versus $1/T$ curve for all the samples. Solid line gives the best fit of the experimental data with equation (7.7). From the slope of S versus $1/T$ curves, activation energy E_S for all the samples were obtained. The constant α' was obtained from the intercept of the plotted curves. All the parameters obtained from fitting the experimental data with equation (7.7) are given in table 2. From the

estimated values of α' from equation (7.7), we found that $\alpha' < 1$ for all compositions. This supports the fact that small polaron hopping is the mechanism for conduction in this system. Mott's equation for the resistivity is given by

$$\frac{\rho}{T} = \rho_{\alpha} \exp\left(\frac{E_p}{k_B T}\right) \quad (7.8)$$

where ρ is resistivity, T absolute temperature ρ_{α} is constant, E_p is activation energy and k_B is Boltzmann's constant. Taking logarithm the above equation becomes

$$\log\left(\frac{\rho}{T}\right) = \log(\rho_{\alpha}) + E_p/k_B T \quad (7.9)$$

It is a straight line equation whose slope is E_p/k_B and y intercept is $\log(\rho_{\alpha})$. The activation energy (E_p) was obtained from the graphs plotting between $\log(\rho/T)$ and $1/T$ as shown in figures 4.12. They are also given in table 2. The calculated values show that both the activation energies (E_p and E_s) gradually increase with increasing sodium content. The huge difference in the values of the two activation energies (E_p and E_s), as originally pointed out by Mott and Davis, is due to the thermally activated behaviour of the hopping transport at high temperature [25]. According to Polaron model, activation energy obtained from resistivity value (E_p) is the energy required for creation of carriers and activating them hopping. Activation energy from thermopower (E_s) is that needed for activating the hopping process. The difference between the activation energies, measured from resistivity and TEP studies is called polaron hopping energy $W_{II} = E_p - E_s$. The calculated values of the polaron hopping energy are also included in table 2. Due to the colossal value of thermoelectric power fitting with thermoelectric equation and activation energy calculation are impossible for the charge ordered manganites.

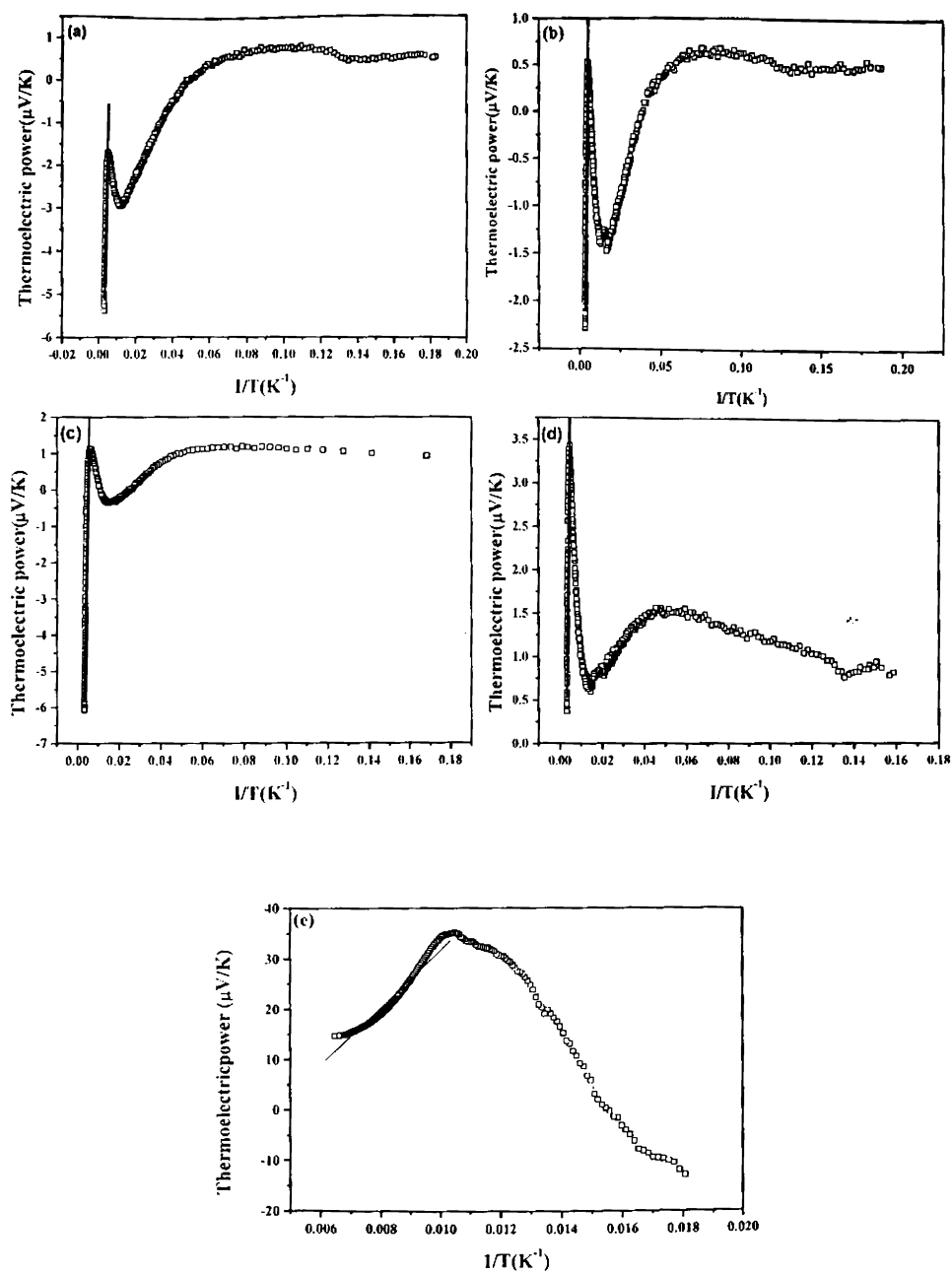


Figure 7.6 Variation of thermoelectric power with reciprocal of temperature for the samples $\text{La}_{1-x}\text{Na}_x\text{MnO}_3$ [(a) $x=0.05$, (b) $x=0.1$, (c) $x=0.15$ (d) $x=0.2$ and $x=0.25$]

An increase of all the parameters E_p , E_s , and W_H with increasing composition x can be understood from the following explanation. Increasing Na concentration sufficiently increases the number of charge carriers (holes) in the e_g band take part in conduction and thereby narrowing the e_g band. Thus as Na concentration increases more energy is needed to release a charge carrier. This effectively increases the activation and hopping energy. According to Mott and Davis [26], the hopping energy W_H is related to the polaron radius (r_p) as

$$W_H = e^2/4\epsilon\left(\frac{1}{r_p} - \frac{1}{R}\right) \quad (7.10)$$

where ϵ is the dielectric constant and R is the average inter site distance related to r_p [$r_p = (\pi/6)^{1/3}R/2$]. From the table it is clear that polaron hopping energy increases with increase in Na concentration, and from equation 7.10 we can see that polaronic radius is inversely proportional to Polaron hopping energy. Hence it can be concluded that polaronic radius decreases with increase of Na concentration.

x	Mn ⁴⁺ /Mn ³⁺	E _p (m eV)	E _s (m eV)	W _H (m eV)	α'
0.05	0.11	29.9	1.78	28.12	-0.095
0.1	0.25	37.17	2.11	35.06	-0.124
0.15	0.43	*	2.49	*	-0.135
0.2	0.67	40.24	3.20	37.04	-0.142
0.25	1	50.7	5.66	45.04	-0.29

Table 2 Thermoelectric power fitting parameters in the high temperature region for the samples $\text{La}_{1-x}\text{Na}_x\text{MnO}_3$ [(a) $x=0.05$, (b) $x=0.1$, (c) $x=0.15$ (d) $x=0.2$ and $x=0.25$]

* Resistivity data in the paramagnetic phase is unavailable

7.3 Conclusion

The thermoelectric powers of the charge ordered GSMO and LNMO samples and non charge ordered LNMO were measured. The charge ordered manganites exhibited colossal values of thermoelectric power at low temperatures. The colossal positive Seebeck coefficient is around 35mV/K near 40K in the case of GSMO sample. This is the one of the highest values reported at this temperature. But for charge ordered LNMO sample the colossal Seebeck coefficient is negative and its value at 60K is around 80mV/K, the highest ever reported value. We could not propose the exact mechanism for such a colossal value of Seebeck coefficient. The thermoelectric peak temperature coincides with the temperature corresponding to the transition from paramagnetic state to magnetically ordered state. Hence spin fluctuation associated with magnetic transition could be one of the reasons. Since colossal value of thermoelectric power is exhibited by charge ordered manganites, we could not ruled out charge ordering as the cause of colossal thermoelectric power. The fitting of low temperature thermoelectric power data of the non charge ordered LNMO manganite need an additional $T^{1/2}$ term (weak localisation contribution) as in the case of its resistivity data fitting. High temperature thermoelectric power studies of non charge ordered LNMO manganite indicated that small polaron hopping as the conduction mechanism rather than large polaron.

References

- [1] Vining C. B, *Nature* **423** (2003) 391.
- [2] Ohta H, *Materials Today* **10** (2007) 44.
- [3] Mahan G, Sales B and Sharp J, *Phys. Today* 50 (1997 March) 42.
- [4] Boukai A. I, Bunimovich Y, Tahir – Kheli J, Yu J-K, Goddard W. A and Heath J. R, *Nature* **451** (2008) 168.

- [5] Rosi F. D, Abeles B and Jensen R. V, *J. Phys. Chem. Solids* **10** (1959) 191.
- [6] Steele M. C and Rosi F. D, *J. Appl. Phys.* **29** (1958) 1517.
- [7] Duarte N. B, Mahan G. D and Tadigadapa S, *Nano Lett.* **9** (2009) 617.
- [8] Bentien A, Johnsen S, Madsen G. K. H, Iversen B. B and Steglich F, *EPL* **80** (2007) 17008.
- [9] Frederikse H. P. R, *Phys. Rev.* **92** (1953) 248.
- [10] Inyushkin A. V, Taldenkov A. N, Ozhogin V. I, Itoh K. M and Haller E. E, *Phys. Rev.B* **68** (2003) 153203.
- [11] Ohta H, Kim S-W, Mune Y, Mizoguchi T, Nomura K, Nakanishi Y, Hirano M, Hosono H and Koumoto K, *Nature Mater.* **6** (2007) 129.
- [12] Ohta S, Nomura T and Ohta H, *Appl. Phys. Lett.* **87** (2005) 092108.
- [13] Maignan A, Hebert S, Li P, Pelloquin D, Martin C, Michel C, Hervieu M and Raveau B, *Crystal Engineering* **5** (2002) 365.
- [14] Coey J. M. D, Viret M and Von Molnar S, *Advances in Physics* **48** (1999) 248.
- [15] Kong W. J, Liu L, Zhu H. W, Wei B. Q and Wu D. H, *J. Phys. Condens. Matter* **17** (2005) 1923.
- [16] Tang J, Wang W, Zhao G-L and Li Q, *J. Phys. Condens. Matter* **21** (2009) 205703.
- [17] Garcia- Landa B, De Teresa J. M, Ibarra M. R, Ritter C, Drost R and Lees M. R, *J. Appl. Phys.* **83** (1998) 7664
- [18] Wagh A. A, Anilkumar P.S, Bhat H. L and Suja Elizabeth, *J. Phys.: Condens. Matter* **22** (2010) 026005.
- [19] Rhyce J. S, Lee K. H, Lee S. M, Cho E, Kim S. I, Lee E, Kwon Y. S, Shim J.

- H and Kotliar G, *Nature* **459** (2009) 965.
- [20] Venkataiah G, Lakshmi Y. K and Reddy P. V, *PMC Physics B* **1** (2008) 7.
- [21] Ang R, Sun Y. P, Yang J, Zhu X. B and Song W. H, *J. Appl. Phys.* **100** (2006) 073706.
- [22] Mandal P, *Phys. Rev. B* **61** (2000) 14675
- [23] Urushibara A, Moritomo Y, Arima T, Asamitsu A, Kido G, and Tokura Y, *Phys. Rev. B* **51** (1995) 14103.
- [24] Aritra Banerjee, Pal S, Bhattacharya S, Chaudhuri B. K, and Yang H. D, *Phys. Rev. B* **64** (2001) 104428.
- [25] Sayani Bhattacharya, Aritra Banerjee, Pal S, Mukherjee R. K, and Chaudhuri B. K, *J. Appl. Phys.* **93** (2003) 356.
- [26] Mott N. F and Davis E. A, *Electronics Process in Non Crystalline Materials*, Clarendon, Oxford (1971).

Chapter 8

Conclusion

Development of novel and new materials for various applications has been the hall mark of material science. Any study in material science necessitates synthesis of phase pure compounds in the required stoichiometry. Characterisation is another integral part of any study in material science and this often leads to taking refuge in modern analytical instruments and some times, in developing in-house technique for characterization of samples. This investigation on Gd based manganites and Na doped manganites is also such an attempt where in samples are synthesized in the purest form without compromising on purity and are characterized at appropriate stages of preparation using various analytical techniques.

Manganites are very interesting class of materials and they crystallize in the perovskite structure and hence attracted the attention of the scientific community since they are capable of exhibiting various properties simultaneously like ferromagnetism, ferroelectricity, magnetoresistance etc. Most of the properties are determined by a variety of factors namely double exchange, Jahn Teller distortion, orbital ordering, charge ordering etc. Among them charge ordering plays a crucial role in the transport and ferroelectric properties of manganites. Low and intermediate bandwidth manganites exhibit charge ordering and hence Gd based low bandwidth and Na doped intermediate bandwidth manganites were selected for the present study. Na doped sample possess further advantages like charge ordering at low doping levels. Special attention was paid to carry out dielectric and thermoelectric power measurements because of the hints from existing literature regarding role of charge order in multiferroicity and large thermoelectric power. In order to understand the nano size effect in

magnetoresistance properties, nano sized Na doped manganites were prepared using citrate gel method.

Gd containing manganites belonging to the series $Gd_{1-x}Sr_xMnO_3$ was prepared by wet solid state reaction method. All the compositions corresponding to ($x=0.3, 0.4$ and 0.5) was synthesised which was found single phasic in nature and without any detectable impurities. A citrate gel method was employed for the preparation of nano sized $La_{1-x}Na_xMnO_3$ ($x=0.05, 0.1, 0.15, 0.2$ and 0.25). This method yielded phase pure compounds with sizes ranging from 20 nm to 40nm. Both these synthesis techniques can be adopted for the preparation of other manganites samples containing various rare earth ions of micron size and nano size.

A complete automated system using a graphical programming package called LabVIEW was developed for the evaluation of dielectric permittivity, impedance and ac conductivity. This set up was modified and completely automated using LabVIEW and C-programming for the evaluation of dispersion parameters using dielectric spectroscopy. The same set up was modified to carry out impedance spectroscopy where in grain impedance and grain capacitance could be estimated. The development of a complete automated system for dielectric spectroscopy and impedance spectroscopy using an LCR meter and LabVIEW can be considered as a major contribution of this investigation from an instrumental technique perspective.

Low temperature magnetoresistance studies of low and intermediate bandwidth manganites assume significance from a theoretical perspective. The D. C conductivity studies of the sample sheds light into the conduction mechanisms and help to establish the role of double exchange interaction in the hopping process. Moreover a comparison, vis a vis the conduction process, between low bandwidth and intermediate bandwidth manganite is possible. It may be established that a metal to insulator transition takes place in both low and

intermediate bandwidth manganites. But in low bandwidth manganites, the transition is not so explicit as in the case of high bandwidth manganites. High magnetic field of about 8T was needed for the explicit metal insulator transition in the charge ordered manganites. This high magnetic field is used for the melting of charge ordered state. Thus the role of charge ordering in the double exchange mechanism was established.

From D. C Conductivity studies it was possible to establish the exact conduction mechanism for GSMO samples both in the paramagnetic and ferromagnetic regions. While in the the paramagnetic region, in the low temperature regime, variable range hopping (VRH) aided the conduction process and in the high temperature regime small polaron hopping (SPH) is the most probable conduction mechanism. However in the ferromagnetic region double exchange is found to be the predominant conduction process. It was found that these samples exhibit a metal to insulator transition at around 40K, where it was also possible to observe a spin glass like transition at around the same temperature. In the case of GSMO series, composition corresponding to $x=0.7$ exhibited 80% magnetoresistance at 120K. This is a significant result, considering the fact that these materials can be tailored for enhancing the transition temperature as well as the magnetoresistance percentage. In the case of LNMO sample it was found that as the amount of sodium was varied, the metal insulator transition gradually shifted from low temperature to room temperature. In the case of LNMO the composition corresponding to $x=0.25$ exhibited a large MR $\sim 93\%$ at around 70K.

A study of dielectric and ac conductivity over a wide range of frequencies revealed interesting observations. The dielectric studies of GSMO samples established the multiferroic nature of the sample under study. The presence of a broad dielectric peak in the temperature versus dielectric constant graph is indication of relaxor ferroelectric behaviour. The ferroelectricity is due to the charge ordering characteristic of the manganites which was explained by inversion

symmetry of an intermediate state between site centered charge ordering and bond centered charge ordering. The ferroelectric behavior was confirmed in the capacitance-voltage (C-V) measurements carried out on these samples. The butterfly nature of C-V curve was an indication of the ferroelectric nature. The frequency dispersion of dielectric parameters was explained by using Maxwell – Wagner capacitor model. The frequency dependent term of ac conductivity was analyzed using power law and the temperature variation of ac power law exponent established the different ac conduction mechanisms in the GSMO manganites.

The temperature dependence of dielectric parameters of non charge ordered LNMO samples indicated the presence of two thermally activated relaxation mechanisms. The low temperature relaxation was attributed to interfacial polarization between grain boundaries and high temperature relaxation is due to hopping of charges between manganese ions. The dispersion parameters like optical dielectric constant, static dielectric constant, spreading factor and relaxation time were evaluated using dielectric spectroscopy. All the Cole – Cole plots were semicircular arcs with centers lying below the real axis, which is an indication of distribution of relaxation time. The linear rising tail in the Cole – Cole plot indicated that the LNMO samples obey Universal Dielectric Response (UDR) model. Applying UDR model in the frequency variations of dielectric permittivity and dielectric loss, the values of optical dielectric constant were elucidated and were in good agreement with those obtained by dielectric spectroscopy. The temperature variation of dielectric parameters of the charge ordered LNMO samples strongly confirmed the role of charge ordering in the ferroelectric property of manganites.

The thermoelectric measurements carried out on both GSMO and LNMO samples was the most exciting part of this investigation. The charge ordered GSMO manganites exhibited a positive colossal value of thermoelectric power of about 35mV/K at around 40K. Colossal thermoelectric power was previously reported for strongly correlated semiconductor FeSb₂ single crystals and reduced

TiO₂ single crystals at around 10K. The observance of colossal thermoelectric power at comparatively higher temperature is important from both a theoretical and experimental point of view. The charge ordered LNMO sample exhibited a negative colossal value of thermoelectric power of about 80mV/K at 60K. To best of our knowledge this is the highest ever reported value of thermoelectric power for these class of materials. We could not propose an exact mechanism for the observed colossal thermoelectric power phenomenon. Since the thermoelectric power peak coincides with the magnetic transition temperature, the spin fluctuation associated with the magnetic transition may be one of the reasons. Since colossal value of Seebeck coefficient is exhibited by charge ordered manganite compounds, the role of charge ordering in the exhibition of colossal thermoelectric power could not be ruled out.

The thermoelectric power studies are usually used in manganites to find out the conduction mechanism. The high temperature thermoelectric power studies of non charge ordered LNMO sample reveal the existence of small polarons in the conduction process. Data generated from low temperature thermoelectric power measurements were fitted using an existing model. The presence of a $T^{1/2}$ term in the equation for Seebeck coefficient, as in the case of low temperature resistivity fitting, could be attributed to weak localization of electrons in the low temperature regime.

The high point of the thesis is the discovery of multiferroism in GSMO samples. This is being reported for the first time. Another important finding of the thesis is the exhibition of colossal thermoelectric power in the case of charge ordered LNMO and GSMO samples. It must be noted here that to best of our knowledge highest reported thermoelectric power is 80mV/K exhibited by the LNMO sample ($x=0.25$).

This investigation is also without any lacunae. A crystal clear explanation for the colossal thermoelectric power could not be provided. This requires further

investigations using various analytical tools. The evaluation of multiferroic nature of GSMO samples was limited to the measurement of permittivity versus temperature and capacitance versus applied voltage. More measurements using ferroelectric loop tracer is required and a thorough study on the multiferroic properties of charge ordered compounds is warranted and is a futuristic proposition. Further, studies employing AC magnetic susceptibility is necessary to establish the spin glass nature of these samples. Such a study together with SQUID measurements will unravel the ununderstood physics occurring at these temperatures and on these compositions.

The display of colossal thermoelectric power by both low and intermediate bandwidth compounds is rather intriguing and investigations are to be extended to other similar compounds. From an application point of view, especially for power generation, using colossal thermoelectric materials, the figure of merit has to be enhanced and for this both electrical conductivity and thermal conductivity have to be appropriately tuned. By a judicious choice of the composition this can be achieved. Perhaps, hybrid nano structures of manganites could well be potential thermoelectric materials for room temperature applications. This can be prospective research topic from an application point of view as well as from a fundamental perspective.

Multiferroism exhibited by charge ordered manganites is another promising finding and much more need to be established with respect to non centre of symmetry considerations, Jahn Teller distortion and charge ordering etc. Sometime back, manganites were considered potential material for autocatalyst and then came superconductivity based on manganite and new manganites have again occupied the centre of attraction on potential multiferroic materials and also for thermoelectric power generation. Perhaps in the coming years one can witness breakthrough in technology using manganites especially for greener environment and earn carbon credits.

